

Feb 16, 2015

Final Report

on

**Determination of the Spatial Distribution of Ozone Precursor and Greenhouse
Gas Concentrations and Emissions in the LA Basin**

Contract No. 09-318

to

**Dr. William Vance
Air Pollution Specialist**

**California Air Resources Board
Research Division
P.O. Box 2815
Sacramento, CA 95812**

**Prepared for the California Air Resources Board and the California
Environmental Protection Agency
by**

**Dr. Jochen Stutz, Dr. Qinbin Li, Dr. Stan Sander
Joint Institute for Regional Earth System Science and Engineering
University of California Los Angeles
Box 957228
Los Angeles, CA 90095**

Disclaimer

The statements and conclusions in this Report are those of the contractor and not necessarily those of the California Air Resources Board. The mention of commercial products, their source, or their use in connection with material reported herein is not to be construed as actual or implied endorsement of such products.

Acknowledgement

This Report was submitted in fulfillment of Contract No. 09-318: Determination of the Spatial Distribution of Ozone Precursor and Greenhouse Gas Concentrations and Emissions in the LA Basin, by the University of California Los Angeles under the sponsorship of the California Air Resources Board. Work was completed as of 12/31/14.

Contents

1. Executive Summary	2
2. Introduction.....	4
3. UV-Vis MAX-DOAS	5
3.1. Experimental setup.....	6
3.2. Instrument description.....	6
3.3. Spectral retrievals.....	7
3.4. Cloud Filtering	10
3.5. Development of radiative transfer modeling tools.....	13
3.5.1. Radiative Transfer Model: VLIDORT.....	13
3.6. Aerosol extinction profiles retrievals	14
3.7. Trace gas profile retrievals.....	16
3.8. Information Content Analysis of Theoretical Retrievals	17
3.8.1. Aerosol.....	19
3.8.2. NO ₂	20
3.8.3. HCHO	21
3.9. Atmospheric Retrievals.....	23
3.9.1. Aerosol.....	23
3.9.2. NO ₂	23
3.10. Comparison with surface measurements	28
3.10.1. Aerosol	28
3.10.2. NO ₂	29
3.11. HCHO to NO ₂ ratios as marker for ozone production efficiency.....	30
4. Near-IR Fourier Transfer Measurements of Greenhouse Gases.....	35
4.1. Measurement Technique	36
4.2. Data Processing and Error Analysis.....	37
4.2.1. Interferogram to Spectrum.....	37
4.2.2. Spectrum to Slant Column Densities (SCD) of Trace Gases.....	37
4.2.3. Column Average Volume Mixing Ratio of GHG in Dry Air (XGHG).....	45
4.2.4. Sample Retrievals from CLARS-FTS	45
4.2.5. Measurement Uncertainty of XGHG	46
4.2.6. Estimation of XGHG Measurement Precision.....	53
4.2.7. Estimation of XGHG Measurement Accuracy	57
4.3. Diurnal Variations of XGHG	57

4.4.	Top-down Estimates of CH ₄ Emissions	59
4.4.1.	CH ₄ :CO ₂ Ratio Originating From Los Angeles.....	59
4.4.2.	Implication for bottom-up CH ₄ emission inventory	60
4.4.3.	Seasonal Variability	61
4.5.	Top-down Estimates of CO ₂ Emissions	63
4.5.1.	CO:CO ₂ ratio in the basin	63
4.5.2.	Top-down CO ₂ emission estimates from 2011 to 2014	65
4.6.	Comparison between CLARS Observations and WRF-VPRM Model	65
4.7.	Future developments	69
5.	Modeling.....	71
5.1.	Model Setup	71
5.2.	Emission Inventories	72
5.2.1.	Carbon Monoxide	72
5.2.2.	Nitrogen Oxides	73
5.2.3.	Hydrocarbons	73
5.3.	Comparison with observations	74
5.3.1.	Meteorology	74
5.3.2.	CO	76
5.3.3.	NO _x	78
6.	Conclusions.....	84
7.	References.....	86
8.	Glossary	96

List of Figures

Figure 3.1: Viewing strategy of the MAX-DOAS instrument from Mt. Wilson.....	6
Figure 3.2: Example of the analysis of a MAX-DOAS spectrum	8
Figure 3.3: Example of O ₄ , NO ₂ , and HCHO DSCDs for one day, May 31 st , 2010, during CalNex.....	9
Figure 3.4. Example of cloud classification of MAX-DOAS O ₄ DSCDs and intensity observations.....	11
Figure 3.5. Diagram of the cloud sorting routine.....	12
Figure 3.6. NO ₂ DSCDs for July of 2011, before and after the cloud-removal algorithm was applied.	12
Figure 3.7: Schematics of the aerosol retrievals from the MAX-DOAS O ₄ DSCDs.	16
Figure 3.8: Example of theoretical retrieval of a typical Los Angeles aerosol profile and a measurement error of 1%.	18
Figure 3.9: Theoretical retrieval of NO ₂ vertical column densities from Mt. Wilson.....	19
Figure 3.10: Example of aerosol extinction retrieval on July 2 nd , 2011.	24
Figure 3.11: Example of an aerosol retrieval on May 31 st , 2011.	25
Figure 3.12: NO ₂ profile retrieval for Mt. Wilson observation on July 2 nd 2011.....	25
Figure 3.13: NO ₂ profile retrieval for Mt. Wilson observation on May 31 st 2011.....	26
Figure 3.14: NO ₂ profile retrieval for Mt. Wilson observation on June 14 th	26
Figure 3.15: Statistics of information content analysis for NO ₂ retrievals in June and July 2011.	27
Figure 3.16: Daily averages of the retrieved NO ₂ vertical profiles for the summer of 2011.....	27
Figure 3.17: Comparison of AOT retrievals from the AERONET sun-photometer at Caltech and the AOT retrieved from the MAX-DOAS O ₄ observations on June 1 st	28
Figure 3.18: Comparison of AOT retrievals from the AERONET sun-photometer at Caltech and the AOT retrieved from the MAX-DOAS O ₄ observations on June 3 rd	29
Figure 3.19: Comparison of the daily averaged NO ₂ concentrations between NO ₂ concentrations retrieved in the boundary layer, and the NO ₂ concentrations measured by the nearby Pomona ground station.	30
Figure 3.20: Plot of HCHO/NO ₂ vs. LN/Q for the surface observations during CalNex.....	31
Figure 3.21: Daily averaged HCHO/NO ₂ ratio measured from Mt. Wilson.	32
Figure 3.22: Monthly averaged DSCDs of HCHO and NO ₂ and HCHO/NO ₂ ratio in the Los Angeles Basin.....	33
Figure 3.23: Hourly average NO ₂ and HCHO DSCDs during 2011.	34
Figure 3.24: Weekday/weekend monthly averaged NO ₂ DSCD ratio for the years 2011-2013..	34
Figure 4.1: Schematic diagram of spectrometer viewing geometry for the Los Angeles Basin. .	41
Figure 4.2 Sample spectral fittings of CO ₂ bands near 1.6 μm region using the CLARS-FTS....	42
Figure 4.3 Root Mean Square of spectral fitting residuals and spectral SNR as a function of time for the measurements of CO ₂ and O ₂ column densities.	43
Figure 4.4: The spectral fitting residuals and their correlation, Pearson correlation coefficients, and histograms for CO ₂ slant column density measurements..	44
Figure 4.5: XCO ₂ measured by CLARS-FTS on January 3 rd , 2013 and differences of retrieved XCO ₂ between the two spectral regions in the Spectralon® viewing geometry.....	47
Figure 4.6: Sample spectral fittings of CH ₄ bands..	48

Figure 4.7: Root Mean Square of spectral fitting residuals and spectral SNR as a function of time for the measurements of CH ₄ and O ₂ column densities in Spectralon® viewing geometry.....	49
Figure 4.8: The spectral fitting residuals and their correlation, Pearson correlation coefficients, and histograms for CH ₄ slant column density measurements.....	50
Figure 4.9: XCH ₄ measured by CLARS-FTS on January 3 rd , 2013 and differences of retrieved XCH ₄ between two spectral regions.....	51
Figure 4.10: XCH ₄ measured by CLARS-FTS and differences of retrieved XCH ₄ between the two spectral regions.....	52
Figure 4.11: XCO measured by CLARS-FTS and differences of retrieved XCO between the two spectral regions.....	55
Figure 4.12: Column averaging kernels of GHG measurements using CLARS-FTS with a Maximum Optical Path Difference (MOPD) of 5 cm.	56
Figure 4.13: Diurnal variations of SVO and LABS, west Pasadena and Santa Anita Park, XCO ₂ , XCH ₄ and XCO on seven consecutive days in May 2012.	58
Figure 4.14: Correlations between XCH ₄ excess (ppb) and XCO ₂ excess (ppm) for West Pasadena (left) and Santa Anita Park (right) between September 1, 2011 and October 30, 2013.	60
Figure 4.15: Map of correlation slopes of XCH ₄ excess to XCO ₂ excess (ppb/ppm) in the Los Angeles basin between of September 1, 2011 and October 30, 2013.	60
Figure 4.16: Seasonal maps of correlation slopes of XCH ₄ excess to XCO ₂ excess (ppb/ppm) in the Los Angeles between September 1, 2011 and October 30, 2013.....	62
Figure 4.17: Monthly variations of Los Angeles basin averaged XCH ₄ :XCO ₂ excess ratio, Vuclan CO ₂ emission, scaled CARB bottom-up CO ₂ emission and derived CH ₄ emission (green).	63
Figure 4.18: Map of correlation slopes of XCO excess to XCO ₂ excess (ppb/ppm) in the Los Angeles basin calculated using CLARS-FTS measurement between September 1, 2011 and October 30, 2014.	64
Figure 4.19: Seasonal-spatial variability in XCO excess to XCO ₂ excess (ppb/ppm) ratio in the Los Angeles basin calculated using CLARS-FTS measurement between the period of September 1, 2011 and October 30, 2014.....	64
Figure 4.20: Yearly trend of observed Los Angeles basin average CO to CO ₂ ratio, CARB CO emissions for the South Coast Air Basin and CO ₂ emissions for the basin.	66
Figure 4.21: Structure of the coupled WRF-VPRM model.....	66
Figure 4.22: CO ₂ SCD measured by CLARS FTS over LA basin and WRF-VPRM simulations.....	69
Figure 4.23: CO ₂ slant column densities over Los Angeles basin on June 20 th , 2010.	70
Figure 5.1: Anthropogenic CO emissions in the two inner domains and hourly variations in the innermost domain.	72
Figure 5.2: Daily averaged anthropogenic NO _x emissions in the two innermost domains and hourly variations in the innermost 4-km domain.	73
Figure 5.3: Simulated and observed hourly averages planetary boundary layer height (PBLH) at the CalNex Caltech supersite for May 27-June 15, 2010.....	74
Figure 5.4: Simulated and observed concentrations of CO vertical profiles for the ensemble of CalNex flights.....	76

Figure 5.5: Simulated and observed surface concentrations of CO at the CalNex Caltech supersite for May 15-June 14, 2010.	77
Figure 5.6: Simulated and observed hourly averages of O ₃ , NO _y , NO, NO ₂ , O _x , HCHO and HNO ₃ concentrations at the CalNex Caltech supersite..	79
Figure 5.7: WRF-Chem simulated surface NO _x and O ₃ concentrations in the SCAB area averaged for May 15-June 6, 2010.....	81
Figure 5.8: Simulated and observed vertical profiles of O ₃ and NO _y for the ensemble of CalNex flights during weekdays (May 4, 14 and 19) and weekends (May 16 and June 20).	83
Figure 5.9: Simulated and observed concentrations of O ₃ , NO _y , HNO ₃ and PAN for the ensemble of CalNex flights during weekdays and weekends..	83

List of Tables

Table 3.1: Wavelength Ranges and Spectral References used for the spectral retrievals of O ₄ , HCHO, and NO ₂ ..	9
Table 3.2: Input and output parameters for VLIDORT	14
Table 3.3: Theoretical DOFs for an aerosol extinction retrieval with a 1% measurement error and a 20% a-priori error.....	20
Table 3.4: Dependence of the theoretical DOFs of aerosol extinction retrievals on measurement and a priori error..	20
Table 3.5: Theoretical DOFs from NO ₂ concentration retrievals by measurement and a priori profile error for a boundary layer aerosol extinction of 0.1 km ⁻¹ and a boundary layer height of 1 km	21
Table 3.6: Theoretical DOFs from NO ₂ concentration retrieval by shape of a priori estimate of vertical concentration profile with a boundary layer aerosol extinction of 0.1 km ⁻¹ ..	21
Table 3.7: Theoretical DOFs from HCHO concentration retrievals by measurement and a priori profile error for a boundary layer aerosol extinction of 0.1 km ⁻¹ and a boundary layer height of 1 km. HCHO measurement errors of 5 % are not uncommon	22
Table 3.8: Theoretical DOFs from HCHO concentration retrieval by shape of a priori estimate of vertical concentration profile with a boundary layer aerosol extinction of 0.1 km ⁻¹ ..	22
Table 4.1: CLARS FTS Measurement Sequence	39
Table 4.2: Spectral range, species that have spectral signatures within the spectral range, and sources of spectroscopic parameters used in spectral fittings.....	54
Table 4.3: Estimated Measurement Precisions ¹	56
Table 4.4: Estimated Measurement Accuracy ¹	57
Table 5.1: WRF-Chem model configurations.....	71
Table 5.2: WRF-Chem simulated (MOD) and observed (OBS) temperature, wind speed, PBLH and water vapor at surface sites and across basin, bias (MOD-OBS), root mean square error (RMSE), standard deviations (S.D.) and correlations (r ²) between model results and observations.....	75
Table 5.3: CO concentrations at surface sites and across the basin..	77
Table 5.4: WRF-Chem simulated (BASE) and observed (OBS) surface chemical species concentrations (O ₃ , NO _y , NO, NO ₂ , HCHO, HNO ₃) at the Caltech super site for May 27-June 15, 2010.....	79
Table 5.5: Same as Table 4.4, but for surface O ₃ , NO _x =NO+NO ₂ at ARB sites for May 15- June 8, 2010.....	80
Table 5.6: WRF-Chem simulated (LOW) and WP-3D observed (OBS) daytime O ₃ , NO _y , HNO ₃ and PAN in boundary layer (<1.5 km) across the basin and weekends.....	82

Abstract

The monitoring of pollutants and greenhouse gases is crucial to support efforts by the State of California to improve air quality and combat climate change. Two remote sensing methods, a multi-axis Differential Optical Absorption Spectroscopy (MAX-DOAS) instrument and a Fourier Transform Spectrometer (CLARS-FTS) to monitor pollutants and greenhouse gases, were developed and deployed at JPL's California Laboratory for Atmospheric Remote Sensing (CLARS) on Mt. Wilson (1673 meters asl) to scan the Los Angeles Basin. A version of the regional air quality model WRF-Chem for the LA basin was developed and validated for the 2010 CalNex experiment.

Vertical profiles of NO_2 concentrations and aerosol extinction were retrieved from the MAX-DOAS observations. MAX-DOAS HCHO/NO_2 ratios show a decreased VOC sensitivity during the weekends compared to weekdays due to lower NO_2 levels on the weekends, in agreement with WRF-Chem results. Elevated $\text{CH}_4:\text{CO}_2$ ratios were observed in west Pasadena and in the eastern LA basin by the CLARS-FTS. The annual basin total top-down CH_4 emissions was derived to be 0.39 ± 0.06 Tg CH_4 per year, significantly larger than the bottom-up emissions. The preliminary annual top-down CO_2 emissions of 211 ± 12 Tg CO_2/year in 2011, 230 ± 12 Tg CO_2/year in 2012, 212 ± 11 Tg CO_2/year in 2013, and 204 ± 10 Tg CO_2/year in 2014, were about 10-15% greater than the CARB bottom-up CO_2 emissions in 2012.

1. Executive Summary

The Los Angeles basin remains one of the most polluted areas in the U.S. Air quality in the LA basin has been studied for several decades and observational networks as well as regulation policies have been put in place to alleviate its impact on human health. It has also been recognized that megacities, such as Los Angeles, contribute substantially to the emission of greenhouse gases and thus regional and global climate change. However, the policies to mitigate global and regional climate change have just begun to emerge, with the State of California's Assembly bill AB32 at the forefront of these efforts in the U.S. Human activities and the associated emissions of ozone and aerosol precursors as well as greenhouse gases are the main cause of these environmental challenges. The monitoring of the atmospheric concentrations of the various trace gas as well their emission rates is thus a crucial undertaking, in particular over long time periods. In the case of pollutants, a network of surface stations has been established that provides point measurements distributed across the LA Basin. Despite the success in improving air quality these networks are still sparse and do not provide information of the vertical distribution of trace gases, which would allow a much better description of the total trace gas amounts and emissions. For greenhouse gases, the problem is direr as a monitoring network does not exist and only a few studies have focused on urban areas.

The goal of our proposal was to develop two remote sensing methods that address these challenges and perform long-term measurements in the Los Angeles Basin. Both methods rely on the remote sensing of trace gases, one in the UV – visible wavelength range measuring NO_2 , HCHO, and aerosols, the other in the near IR measuring CO_2 , CH_4 , and CO. Both systems were located at JPL's California Laboratory for Atmospheric Remote Sensing (CLARS) on Mt. Wilson, California. The UV-vis multi-axis Differential Optical Absorption Spectroscopy instrument, has been operational since Spring 2010, measuring path-integrated concentrations, i.e. slant column densities, of pollutants such as NO_2 , HCHO, as well as aerosol extinction in the wavelength range from 300-530nm. The instrument samples 8 consecutive elevation angles, from +6 to -10 degrees in 5 azimuth directions from CLARS. We developed several tools to analyze and interpret this long-term data set of over one million measurements. A cloud sorting algorithm was developed to identify measurements that are impacted by clouds above or below Mt. Wilson. To convert the trace gas slant column densities into concentrations and aerosol extinction vertical profiles, we implemented a fast radiative transfer model (RTM) that allows for the simulation of the effective light path through the atmosphere. The RTM was combined with a two-stage non-linear / linear optimal estimation inversion to derive aerosol extinction profiles followed by the determination of trace gas profiles. To ensure that this novel approach is indeed able to retrieve the vertical aerosol and trace gas profiles with sufficient accuracy, an information content analysis for our Mt. Wilson observational strategy was performed. In general we found that the remote sensing from a mountaintop approach can derive 3-4 pieces of information on aerosol extinction, which means that averaged extinction in 3-4 height intervals in the lower 2 km can be derived if no other information, such as boundary layer height, is included in the retrieval. For NO_2 five pieces of information can be retrieved, which translates into a profile with at least a 400-500 m vertical resolution. In both cases the retrieval will be able to at least determine the boundary layer average and in the case of NO_2 typically provide two data points in the boundary layer. Example retrievals show a clear identification of the boundary layer and the higher aerosol and NO_2 levels in the boundary layer compared to aloft. Based on this encouraging analysis we proceeded to derive vertical profiles of NO_2 and aerosol extinction for

LA for a 4 year period. This data is available for model testing and to follow trends in trace gas and aerosol levels. Our original proposal also included analysis of SO₂ and glyoxal. However, we found that SO₂ was below our detection limit, confirming the findings of the CalNex field experiment during which we observed that SO₂ mixing ratios rarely exceeded 0.5 ppb. The analysis of glyoxal, which is considerably more challenging than those of NO₂ and HCHO, is ongoing. However mixing ratios are also expected to be rather low.

An exciting new application of our observations is the use of the HCHO/NO₂ ratio to study the long-term trend of the VOC/NO_x sensitivity of ozone formation in the LA Basin. Based on observations from the CalNex ground site, we have determined the HCHO/NO₂ cross-over point between VOC and NO_x limited ozone formation. The daily averaged HCHO/NO₂ ratios from Mt. Wilson show a clear pattern with higher ratios, indicative of decreased VOC sensitivity, during the weekends, and lower ratios during the weekdays. The monthly averaged NO₂ and HCHO DSCDs from Mt. Wilson from 2011-2013 show that this weekend effect is caused by lower NO₂ levels on the weekends. The data also shows a decrease in monthly averaged NO₂ slant column densities during weekdays, while weekend NO₂ does not seem to decrease as much. This trend, however, is not reflected in the long-term trend of HCHO/NO₂ ratios.

A new Fourier Transform Spectrometer called CLARS-FTS has been taking measurements since May 2010) on Mt. Wilson. From its mountaintop location at an altitude of 1673 meters, the instrument points at a programmed sequence of 28 ground target locations in the LA basin, recording spectra of reflected near-IR solar radiation. Column-averaged dry-air mole fractions of greenhouse gases (XGHG) including XCO₂, XCH₄, and XCO are retrieved several times per day for each target, with best precisions of 0.16%, 0.26% and 4.10% for XCO₂, XCH₄, and XCO respectively. Spectra from a local Spectralon® scattering plate are also recorded to determine background (free tropospheric) column abundances above the site, with precisions of 0.09%, 0.14% and 1.94% for XCO₂, XCH₄, and XCO respectively. Comparisons between measurements from LA basin targets and the Spectralon® plate provide estimates of the boundary layer partial column abundances of the measured species. Using two years of observations acquired between September 2011 and October 2013, we derived maps of CH₄:CO₂ in the basin. Significant spatial and seasonal variability were observed due to varying emission patterns and atmospheric transport. A two-year integrated map of CH₄:CO₂ showed an elevated CH₄:CO₂ ratio in west Pasadena and in the eastern LA basin. Using the basin average CH₄:CO₂ ratio and the bottom-up CO₂ emissions for the basin, we derived the annual basin total top-down CH₄ emissions to be 0.39±0.06 Tg CH₄ per year, which is significantly larger than the bottom-up emissions. Using more than three years of observations acquired between September 2011 and October 2014, we derived maps of CO:CO₂ in the basin. A three-year integrated map of CO:CO₂ showed an elevated ratio in western Los Angeles basin. Larger CO:CO₂ ratios were observed in summer compared to winter. Further investigation using an atmospheric transport model is essential to disentangle emission from transport processes. Using the annual trend of CO:CO₂ ratio observed by the FTS and the bottom-up CO emissions, we derived the annual top-down CO₂ emissions of 211±12 Tg CO₂/ year in 2011, 230±12 Tg CO₂/ year in 2012, 212±11 Tg CO₂/ year in 2013, and 204±10 Tg CO₂/ year in 2014. The top-down CO₂ emissions were about 10-15% greater than the CARB bottom-up CO₂ emissions in 2012. Spatial and temporal patterns of XCO₂ in the Los Angeles basin observed by the CLARS-FTS are simulated by WRF-VPRM model. The model results have a low bias of 10% compared to that of CLARS FTS observations. Model inversion will be performed to derive CO₂, CH₄ and CO emissions in the LA basin.

Our original proposal aimed to use inverse 3D urban air-shed models to interpret our data. However, the inversion algorithms did not become available in time to apply them to our data. In our initial work we developed a version of the regional air quality model WRF-Chem to simulate and analyze meteorological conditions, as well as CO, NO_x and ozone concentrations in the LA basin. That technique was applied and validated for the 2010 CalNex experiment (May-June 2010). The meteorological part of the model performed well with respect to simulating the land sea breeze, inland pollutant transport and boundary layer heights. CO concentrations at Caltech, and the inland source region during the day and night were overestimated by 42%, ~20% and 30-50% respectively. The model overestimation of CO in the basin indicated that the CO emissions in the model (28% reduction from NEI'05) were still too high. A 45% reduced NO_x emissions rate relative to NEI'05 improved model performance relative to a 24% NEI reduction case for daytime NO_x and O₃ in the source region. The lower NO_x emissions increased O₃ by 6.8 ppb and 2.9 ppb on weekdays and weekends respectively in the model, indicating that O₃ formation in the basin is NO_x-saturated. The relatively smaller O₃ increase on weekends may indicate that modeled weekend O₃ production is shifted to be less NO_x-saturated compared to weekdays. The modeled weekend-to-weekday difference was much smaller than the observations with a small 2.9 ppb O₃ increase and a 16% NO_x reduction. Together with overestimated NO_y on weekends and underestimated NO_y on weekdays in the basin, we conclude that a 22-26% weekend-to-weekday difference in NO_x emissions in the model is not large enough and weekend NO_x emissions were still overestimated in the model.

2. Introduction

The quantification of emissions and trends in trace gas levels are crucial for our understanding of atmospheric air pollution, i.e. ozone and aerosol chemistry, as well as to better quantify the impact of greenhouse gases on our climate. Regional air quality has been studied for decades, and observational networks as well as regulation policies have been put in place to alleviate its impact on human health. However, the policies to mitigate global and regional climate change have just begun to emerge. Following its history as one of the most environmentally progressive states in the U.S., the State of California recently passed a mandate (Assembly Bill (AB) 32) that requires a reduction of the emissions of the major greenhouse gases to 1990 levels by 2020. That bill and our continued focus on air quality introduces new challenges for scientists and policy makers.

Degradation of air quality and climate change is driven by anthropogenic emissions of ozone and aerosol precursors (NO_x, CO, VOCs, and SO₂) and their chemical transformations, as well as emissions of various greenhouse gases (CO₂, CH₄, N₂O, and CFCs). It is thus crucial to accurately quantify trace gas levels, their spatial distribution, and their emissions to best support the development of air pollution and climate change mitigation strategies. The observation of those parameters presents a number of challenges. For greenhouse gases the problem is direr than for air pollutants since monitoring networks do not exist and only a few studies have focused on urban areas. In addition, measurements are often only performed at a few locations, introducing uncertainties into the overall emissions budget, as well as making it impossible to identify the major sources of those emissions. The development of improved tools for monitoring and studying trace gas concentrations and emissions as well as aerosol properties on larger spatial and temporal scales continues to be an important undertaking.

The current approach to monitoring air pollutants relies on a limited number of surface monitoring sites, while networks for greenhouse gases are only just emerging. The motivation for this project was to demonstrate and apply novel remote sensing methods from a mountaintop to provide new and unique insights into the concentrations and emissions of ozone precursors and greenhouse gases in the Los Angeles Basin. The observations were originally planned for a 2 year period but, through contract extensions, ended up a period of more than 3 years. We originally had planned to use inverse 3D urban air-shed models to interpret our data, but the inversion algorithms did not become available in time to apply them to our data. However, we will report on some initial work in this direction.

The two remote sensing instruments, one in the UV–visible wavelength range, the other in the near IR, were located at JPL’s California Laboratory for Atmospheric Remote Sensing (CLARS) on Mt. Wilson, California (1673 meters above sea level). Both instruments have been operating from May 2010 until today, although we will only discuss IR data from the mid-2011, after the FTS instrument was fully aligned and producing high-quality data.

The UV-vis system is based on Multi-Axis Differential Optical Absorption Spectroscopy (MAX-DOAS), which measures narrow-band absorptions of pollutants such as NO₂, HCHO, as well as aerosol extinction in the wavelength range from 300-530nm. The instrument sampled 8 consecutive elevation angles, from +6 to -10 degrees, in 5 azimuth directions from CLARS. Section 3 of this report will give details on the instrument, the spectral data analysis and the vertical profile retrieval. The results of the MAX-DOAS observations will be discussed with respect to the long-term trend in NO₂ as well as the trend in NO_x/VOC sensitivity of ozone formation using the HCHO/NO₂ ratio from our observations.

The near-IR instrument is based on a novel remote sensing approach for monitoring the spatial and temporal distributions of greenhouse gases in the Los Angeles basin using high-resolution spectroscopy. A new Fourier Transform Spectrometer called CLARS-FTS was deployed at CLARS on Mt. Wilson, California, and performed long-term measurements of greenhouse gases during sunny days. The instrument points at a number of ground target locations in the Los Angeles basin, recording spectra of reflected near-IR solar radiation. Column-averaged dry-air mole fractions of greenhouse gases (XGHG) including XCO₂, XCH₄, and XCO are retrieved several times per day for each target. The details of the instrument, data retrieval and methodology to determine GHG emissions will be described in Section 4 of this report. This section also presents the results of the observations, e.g. emission factors of methane and their spatial distribution.

We developed a version of the regional air quality model WRF-Chem to simulate and analyze meteorological conditions and CO, NO_x and ozone concentrations in the Los Angeles basin. This was originally applied to the CalNex campaign (May-June 2010) to validate the model. While the adjoint/inverse of the model did not become available, we will, nevertheless, briefly review this aspect of our project in Section 5.

3. UV-Vis MAX-DOAS

We operated UCLA’s multi-axis Differential Optical Absorption Spectroscopy instrument (MAX-DOAS) (Platt and Stutz, 2008) on Mt. Wilson. The MAX-DOAS system measures path-averaged concentrations of NO₂, HCHO, and O₄ (as a proxy for aerosol extinction) using the absorptions in the UV and visible wavelength range. The path-averaged concentrations are

typically referred to as slant column densities, SCD, or if taken relative to a zenith viewing reference for removal of the stratospheric trace gas absorptions, differential slant column densities, DSCD. Our original idea of assimilating these DSCDs into a 3D chemistry and transport model could not be realized. Consequently we pursued the alternative approach of employing numerical inversion techniques to derive vertical trace gas profiles. Radiative transfer calculations in combination with optimal estimation techniques were developed for this project. These methods were then applied to the Mt. Wilson observations.

The following sections discuss the MAX-DOAS observational setup and spectral retrieval methodology developed within this project. We will also discuss various theoretical considerations on the performance of the retrievals to provide a better understanding on the capability of our method to derive vertical trace gas profiles. The retrieved aerosol extinction and trace gas concentration profiles will be presented and discussed. One aspect of our work, which was not included in the original proposal, but has proven to be interesting and potentially very useful for the ARB, is the use of the HCHO/NO₂ DSCD ratio to investigate the VOC/NO_x sensitivity of ozone formation in the Los Angeles Basin. We will discuss the results from this exercise at the end of this section.

3.1. Experimental setup

The UCLA MAX-DOAS was installed on Mt. Wilson, California in April of 2010. It is housed at the California Laboratory for Atmospheric Remote Sensing (CLARS), a facility run by the NASA Jet Propulsion Laboratory. CLARS is at an altitude of 1673 meters above sea level (34° 13' 28'' N, 118° 3' 25'' W), in the San Gabriel Mountains. CLARS is above the boundary layer most of the time, and as it overlooks the Los Angeles basin, it presents an excellent vantage point of the lowest several kilometers of the atmosphere (Figure 3.1).



Figure 3.1: Viewing strategy of the MAX-DOAS instrument from Mt. Wilson

3.2. Instrument description

The MAX-DOAS consist of a telescope unit, which includes a hemispheric scanner consisting of two elliptical flat mirrors at 45° and stepper motors. This setup allows for observations in nearly all direction in its upper hemisphere. The telescope/scanner unit has a field of view of

~0.4°C. Light collected by the scanner is focused onto a 1 mm diameter, 5m long, quartz fiber, which is connected to a Czerny-Turning type grating spectrometer (Acton Spectra Pro 300i, 600g/mm grating, 200 μm width entrance slit) coupled to a Hamamatsu 1024 pixel photodiode array (Hoffman Messtechnik with Hamamatsu S3094 PDA). The system has a spectral resolution of 0.92 nm and is thermally stabilized at 35°C, while the photodiode array is cooled to -20°C. The system alternates between observation in spectral window centered in the UV at 385 nm (320-450 nm), and a window centered in the visible at 530 nm (465-595 nm). A more in-depth description of the UCLA MAX-DOAS can be found in Pikel'naya *et al.* (2007).

The MAX-DOAS' hemispheric scanner was operated to look in a combination of five azimuth angles (147.36°, 160°, 172.45°, 182.0°, and 240°) and eight elevation angles (+6°, +3°, 0°, -2°, -4°, -6°, -8°, and -10°), thus scanning from east to west into the boundary layer (negative elevation angles) and horizontally/upwards into the free troposphere (positive elevation angles) (Figure 3.1).

The instrument cycles through all angle combination in sequence during the day. A zenith scan is taken after each azimuth scan to provide a measurement of the stratospheric component of NO₂ as well as to allow for a better removal of solar Fraunhofer lines in the spectral retrievals. Spatial scans are performed consecutively in the UV and the visible wavelength range. Observation from each viewing angle takes approximately one minute, and the full azimuth/elevation cycle for both the UV and visible light regions, including zenith scans, takes 60-80 minutes. At night, Hg emission lines, dark-current, and electronic offset spectra are recorded.

3.3. Spectral retrievals

The MAX-DOAS measurements are based on the observations of weak trace gas absorptions in solar radiation collected at the various viewing directions. This retrieval requires sophisticated numerical methods that involve a solar reference that describes the spectral characteristics of the light source, i.e. the sun, the pure trace gas absorptions, and the description of scattering effects in the atmosphere. All of these parameters vary with wavelength. Consequently a wide range of wavelength intervals can be used to retrieve trace gas information. NO₂ was retrieved in four wavelength intervals, from 323.4-350 nm, 419.5-447 nm, 464-506.9 nm, and 519.8-587.7 nm. HCHO was fit simultaneously alongside NO₂ in the 323.4-350 nm region. O₄ was observed in three intervals, from 350-390 nm, 464-506.9 nm, and 519.8-587.7 nm.

The retrieval was performed using a combination of a linear and nonlinear least-squares fit (Stutz *et al.*, 1996, Platt and Stutz, 2008). The fit includes a Fraunhofer reference spectrum measured in the zenith, a simulated Ring (Raman scattering) spectrum (Vountas *et al.*, 1998), and reference absorption spectra for the major trace gas species in these regions. Each of the trace gas reference spectra was convoluted using the instrument function from a Hg line to simulate the degradation of the spectral resolution by the spectrometer. The I₀ effect from the solar spectrum was considered in this convolution process (Aliwell *et al.*, 2002). O₃ and NO₂ references were taken from Voigt *et al.* (2001) and Vandaele *et al.* (1998), respectively. For HCHO, we used the cross section of Cantrell *et al.* (1990) and the O₄ reference spectrum was provided by Hermans *et al.* (1999). The measurement spectra were allowed to spectrally stretch and squeeze in wavelength to correct for small spectral drift of the spectrometer. A fifth order polynomial was included in the fit to describe Rayleigh and Mie scattering. The retrieval was performed with the DOASIS software package (Univ. Heidelberg).

The uncertainty of these retrievals is assessed in various ways. The set-up of the retrieval algorithm is checked by visually comparing trace gas references with the retrieved spectra. Figure 3.2 shows an example of this approach for O₄, NO₂, and HCHO. The literature absorption spectrum (red line) agrees well with the retrieved spectrum (blue line). Thus all gases can be clearly identified. Figure 3.2 also shows that the agreement is not perfect. In our case, most of the disagreement stems from unavoidable photon noise in the spectra. This disagreement is then the basis of the error calculation performed by the least squares fitting process (see Platt and Stutz, (2008) for details). The final data is thus reported with a statistical uncertainty determined for each data point that is calculated based on the noise in the respective spectrum. This error varies with atmospheric conditions as well as the solar zenith angle as the noise depends on the amount of light collected. Table 3.1 gives an overview of the various spectral intervals and the fitted trace gases. Also listed is the detection limit of the DSCD which was determined to be twice the average error of the spectral retrievals over a several month period. Since our method does not calibrate the instrument, the accuracy of the measurements is dominated by the reported uncertainties of the literature absorption cross sections included in the spectral retrievals. These uncertainties are in the range of 5-10% depending on the trace gas. There is also a small instrumental uncertainty of 2% which is minor compared to the cross-section uncertainties.

Finally, it should be noted that the analysis of NO₂ in four different wavelength intervals has not been previously reported and that our results are unique in this respect.

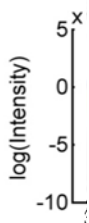


Figure 3.2: Example of the analysis of a MAX-DOAS spectrum

Table 3.1: Wavelength Ranges and Spectral References used for the spectral retrievals of O₄, HCHO, and NO₂. Note that a zenith solar reference, ring spectra and a polynomial of degree 5 are also included in the fit.

Species	Scan	Wavelength Interval (nm)	Fitted Spectral References	Detection Limit
O ₄	UV	350-390	NO ₂ , O ₄ , HCHO, HONO	$7 \cdot 10^{41}$ molec ² /cm ⁵
O ₄	Vis	464-506.9	NO ₂ , glyoxal, O ₄ , H ₂ O	$8 \cdot 10^{41}$ molec ² /cm ⁵
O ₄	Vis	519.8 - 587.7	NO ₂ , O ₄ , O ₃ , H ₂ O	$5 \cdot 10^{41}$ molec ² /cm ⁵
HCHO	UV	323.4-350	HCHO, O ₄ , O ₃ , HONO	$5 \cdot 10^{15}$ molec/cm ²
NO ₂	UV	323.4-350	HCHO, O ₄ , O ₃ , HONO	$3 \cdot 10^{15}$ molec/cm ²
NO ₂	UV	419.5-427.9 & 432.4-447	NO ₂ , glyoxal, O ₄ , H ₂ O	$1 \cdot 10^{15}$ molec/cm ²
NO ₂	Vis	464-506.9	NO ₂ , glyoxal, O ₄ , H ₂ O	$1 \cdot 10^{15}$ molec/cm ²
NO ₂	Vis	519.8 - 587.7	NO ₂ , O ₄ , O ₃ , H ₂ O	$2 \cdot 10^{15}$ molec/cm ²

Figure 3.3 shows an example of the retrieved DSCDs for one day during May 31st 2010. It should be noted that the DSCD error bars are too small to be visible in this graph. The data shows the clear separation with elevation angle and azimuth for all trace gases.

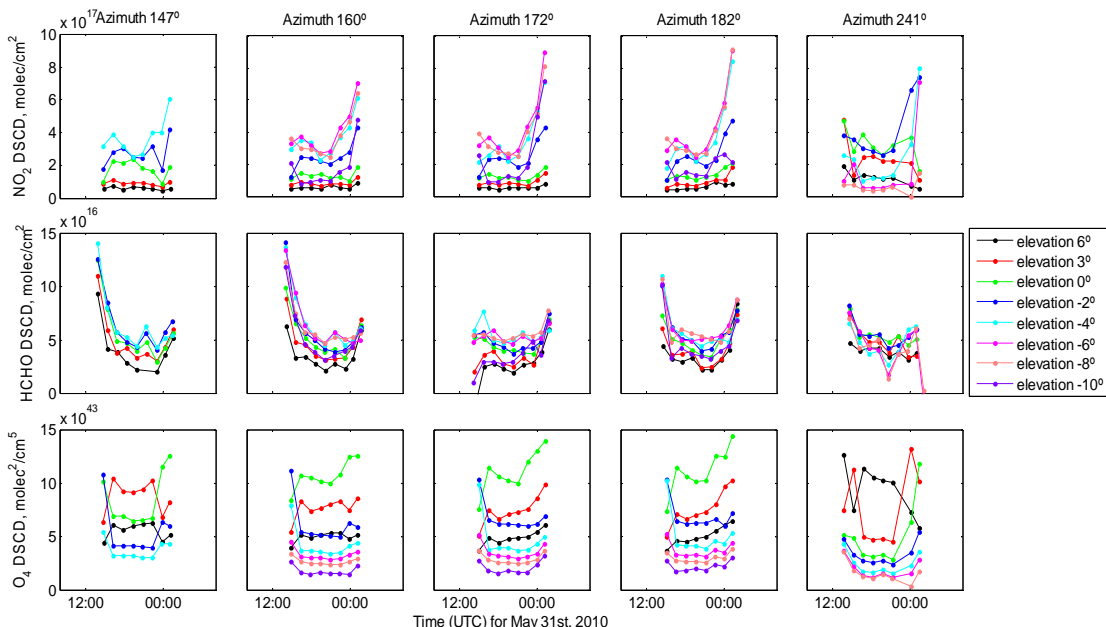


Figure 3.3: Example of O₄, NO₂, and HCHO DSCDs for one day, May 31st, 2010, during CalNex.

We also attempted a retrieval of SO₂ and glyoxal, as stated in our original proposal. However SO₂ DSCDs were typically below our detection limit, which makes a retrieval of vertical profiles impossible. The low SO₂ DSCDs confirm our observations made with our active (using a lamp) Longpath-DOAS system, which found that SO₂ mixing ratios rarely exceeded 0.5 ppb. It should be noted that the LP-DOAS is more sensitive than the MAX-DOAS, as the atmospheric absorption pathlength of scattered solar

radiation in the UV region in which SO_2 absorbs is much shorter and because of spectra interferences with the stratospheric ozone absorption.

We developed the spectral retrieval method for glyoxal, but found that its results were not reliable. This is likely caused by inaccuracies in the description of NO_2 and water absorptions, which are strong in the region in which glyoxal absorbs. We are still working on optimizing this retrieval, but gave it lower priority compared to the analysis of NO_2 and HCHO. We expect glyoxal mixing ratios to be rather low, which make vertical profile retrievals considerably more difficult due to the larger measurement errors. Because the vertical profile retrieval for SO_2 and glyoxal would likely not be successful we decided not to pursue this further in the project.

3.4. Cloud Filtering

As with most scattered-sunlight remote sensing applications, clouds represent a challenge as they are highly variable and strongly impact the observations and the radiative transfer in the atmosphere. Considering the large data-set we have collected over the past years, we have developed an automated cloud filtering algorithm to identify and sort out measurements impacted by clouds. This algorithm was applied to the data to ensure that measurements considered in the trace gas concentration retrievals are not contaminated by the presence of clouds. In this section we will briefly describe the principles of this algorithm.

The presence of clouds is reflected both in the O_4 DSCDs and in the light intensity (photon count) detected by the MAX-DOAS. A unique problem for our Mt. Wilson application, for example compared to ground or satellite remote sensing observations, is the presence of clouds above and below Mt. Wilson. In short, the algorithm is based on the fact that clouds below Mt. Wilson are more reflective than the surface thus increasing the observed intensity, while at the same time blocking the view into the basin, decreasing the effective absorption light path and thus the O_4 DSCDs. Clouds above Mt. Wilson attenuate solar radiation thus decreasing the intensity, while most often leaving the O_4 column unchanged or increasing it slightly. It should be noted that, because our spectra analysis is relative to a temporally close zenith reference spectrum, the effect of high clouds is often reduced.

To provide a calibration for clear skies we installed a camera at Mt. Wilson in May 2011 to collect images of the MAX-DOAS field of view. The images, obtained over several months, were classified into three categories: “clear days” with very few to no clouds, “low cloud days” with partial or full cloudiness at or below 1.7 km, and “high clouds” with partial or full cloud coverage above Mt. Wilson. We then determined a clear day reference behavior for O_4 DSCDs and intensity as a function of solar zenith angle for each viewing direction by fitting a second-order polynomials to the clear sky data. A comparison of O_4 DSCDs and intensity under cloudy conditions show distinct deviations from this polynomial (Figure 3.4). The clear-sky reference polynomials are generally consistent for each elevation angle for all seasons and can thus be applied on our entire data set.

The statistical distribution of the clear sky days relative to the reference polynomial was Gaussian and was dominated by random errors. Cloudy days had a long “tail” in the statistical distribution relative to the reference polynomial. Consequently, the standard deviations from the polynomial fit of clear-sky intensity and O_4 DSCDs was used as suitable cut-off values for cloudy observations. Figure 3.5 shows a sketch of the cloud sorting algorithm as it was implemented for our data set. Figure 3.6 show the results for the cloud sorting in July 2011.

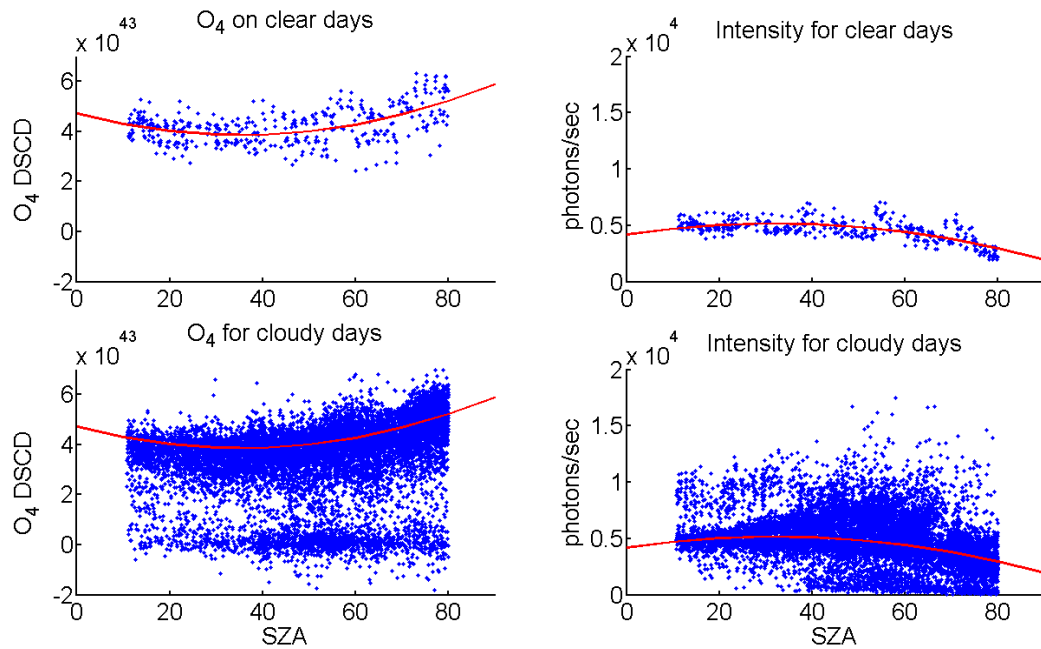


Figure 3.4. Example of cloud classification of MAX-DOAS O₄ DSCDs (left two plots) and intensity observations (right two plots) and fitted polynomial for one viewing elevation angle. The 2nd order fit to clear sky days is the same in each plot, so that the deviation of high clouds and especially low clouds is clear.

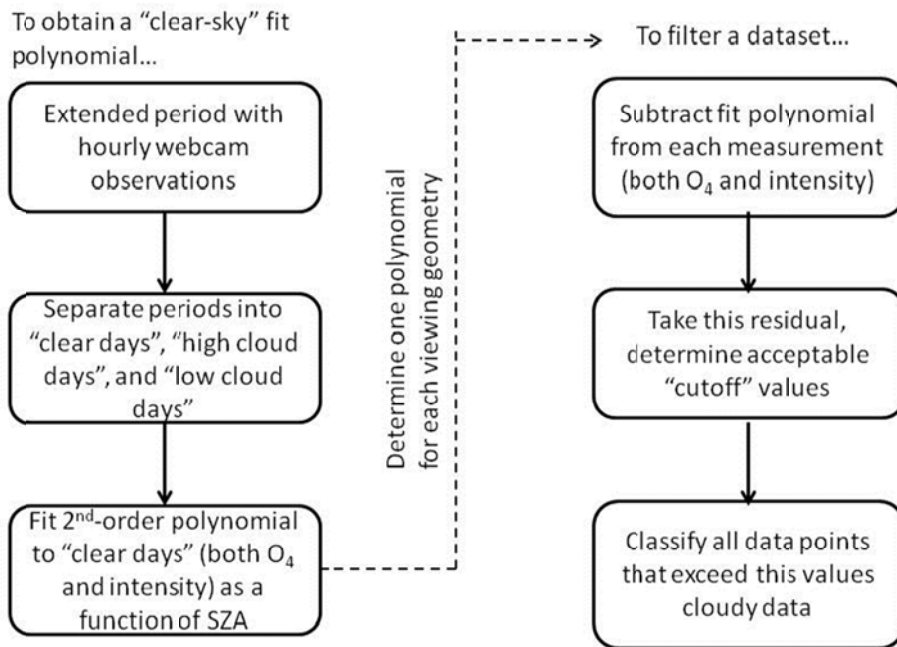


Figure 3.5. Diagram of the cloud sorting routine, from which we are able to systematically identify which of our measurements were taken during cloudy periods.

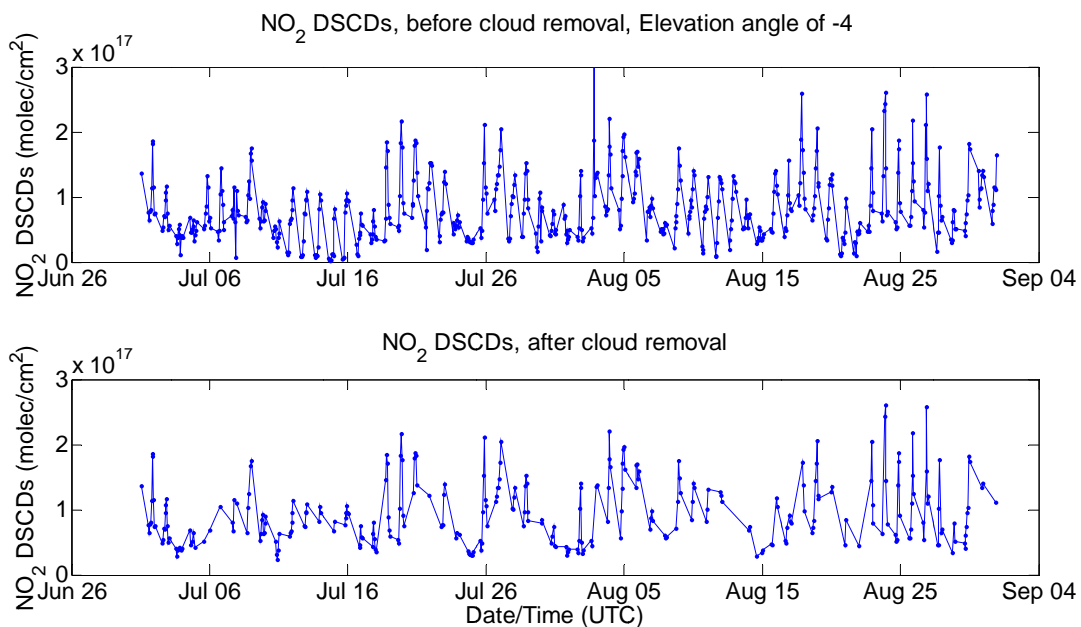


Figure 3.6. NO₂ DSCDs for July of 2011, before and after the cloud-removal algorithm was applied. The summer of 2011 had an extended "June gloom" period, with unusually high amounts of clouds, so it was a good test for the algorithm.

3.5. Development of radiative transfer modeling tools

Originally to interpret our MAX-DOAS observations, we intended to perform a direct comparison of the trace gas DSCDs with forward radiative transfer model calculations using the output of the WRF-CHEM model. We thus initially developed offline RT calculations, using a Monte Carlo model (McArtim, Univ. Heidelberg, Deutschmann et al., 2011), which was linked to WRF-CHEM. However, due to the delay in the development of the WRF-CHEM adjoint we decided to pursue a different approach to interpret the MAX-DOAS observations, namely using inverse modeling combined with the observations to derive vertical profiles of aerosol extinction and trace gases. We will thus not further discuss the WRF-CHEM based RT modeling efforts.

The challenge with interpreting MAX-DOAS observations is the initially unknown absorption light-path in the atmosphere. While in some cases geometric light paths can be assumed, this is often not the case, especially in a polluted atmosphere such as that in Los Angeles. In addition to the well-known Rayleigh scattering effects, the presence of aerosol can impact the length of path reflected or scattered sunlight travels. It is thus necessary to perform additional calculations to convert the observed trace gas DSCDs into concentrations. Luckily information on the path the light takes through the atmosphere, often referred to as radiative transport, can be gained from the observation of the oxygen dimer, O_4 , which has a temporally constant concentration profile (proportional to the square of the oxygen concentration). Thus measured O_4 DSCDs contain information about the various radiative transfer effects (Platt and Stutz, 2008).

As mentioned above, the conversion of the MAX-DOAS DSCDs into trace gas concentration profiles requires radiative transfer calculations and inversions using optimal estimation techniques (Hönninger et al, 2004). Trace gas absorptions in the UV (above 320nm) and visible wavelength ranges are weak and in a first approximation radiative transfer is independent from the absorption of these trace gases. Consequently the retrieval can be subdivided into two steps (Platt and Stutz, 2008). First the radiative transfer, and in particular the influence of aerosol scattering, is determined using O_4 DSCDs. Besides a description of the radiative transfer, this set also yields vertical profiles of aerosol extinction. This first step is computationally and mathematically more demanding as the underlying problem is non-linear. It thus requires iterative numerical methods that make multiple calls to the radiative transfer code, making this computationally expensive. Once the radiative transfer has been determined one can derive the trace gas vertical concentration profile in a second step. This step can use a linear retrieval and is thus less complicated.

As part of this project, we developed the tools to perform these inversion methods to fully take advantage of the MAX-DOAS observations. The radiative transfer model as well as the inversion approach will be described in the following section. We also spent a considerable amount of effort to performing theoretical calculations to provide a better understanding on how much information on the vertical distribution of aerosol and trace gases can be derived. The results of these activities will be discussed in Section 3.8

3.5.1. Radiative Transfer Model: VLIDORT

Due to the intensive calculations that are required to retrieve continuous aerosol extinction and trace gas profiles for the long-term MAX-DOAS measurements, a fast radiative transfer model (RTM) was needed. We thus implemented and modified a version of VLIDORT, which is derived from the well-known first version of the Linearized Discrete Ordinate Radiative Transfer

(LIDORT) scalar code (Spurr et al., 2001; Spurr 2006). VLIDORT, which was developed for the computation of the Stokes vector components in a multi scattering multilayer medium, is a fully linearized RTM. It is capable of calculating the full radiance field simultaneously, including all of the analytic weighting functions with respect to atmospheric and surface properties (Spurr, 2006). The linearization makes VLIDORT very computationally efficient, while maintaining its accuracy. VLIDORT was validated by being compared to other RTMs prior to its implementation in this project. VLIDORT uses a user-defined environment, where geophysical atmospheric inputs such as vertical profiles (thermal, trace gases and aerosol), optical parameters (single scattering albedo, asymmetry function, optical thickness, phase function moments) and spectral properties (cross sections, wavelengths), are supplied by the user (Table 3.2). It then generates a set of intensities and weighting functions that allow for iterations in a multi-parameter atmospheric retrieval with a single call of the model per step (Table 3.2). VLIDORT use a “pseudo-spherical” approximation of the radiative transfer equation to simulate the earth’s curvature, which is essential for our observations close to the limb, i.e. elevation angles close to zero. Further information on VLIDORT can be found in Spurr [2006].

Table 3.2: Input and output parameters for VLIDORT

VLIDORT model inputs	VLIDORT model outputs
<ul style="list-style-type: none"> • Pressure and Temperature profile • O₃ and NO₂ profile • Solar geometry (Solar zenith and relative azimuth angle) • Altitude of detector • Viewing elevation angle • Aerosol optical depth profile • Surface albedo • Aerosol Single-Scattering Albedo (SSA) • Aerosol asymmetry factor • Absorption cross-sections (for O₃, NO₂, and O₄) 	<ul style="list-style-type: none"> • Simulated Radiances, with and without absorbers and aerosols • Intensity derivative with respect to aerosol optical depth $\left(\frac{\partial I}{\partial \tau}\right)$ • Intensity derivatives with respect to trace gas absorptions (for O₃, NO₂, and O₄) <p data-bbox="857 1146 1276 1178"><i>Calculated outside of VLIDORT:</i></p> <ul style="list-style-type: none"> • Simulated slant-column densities from POV of detector • Jacobian matrices of O₄ SCDs with respect to aerosol optical depth $\left(\frac{\partial [SCD(O_4)]}{\partial \tau}\right)$ and relative radiances

3.6. Aerosol extinction profiles retrievals

Typically the retrieval of aerosol extinction profiles from ground-based or satellite observations uses measured radiances. We initially performed tests with that approach and found that the radiance based retrieval worked for theoretical cases. However, the application for real radiance observations from Mt. Wilson was not as reliable, and was also more sensitive to the effects of clouds in boundary layer measurements. We thus chose to use O₄ DSCD as the measurement vector, \vec{y} , in our aerosol retrieval (Wagner et al., 2004, Friess et al., 2006). Besides a better reliability, this approach has other advantages. Due to the O₄ vertical profile, which shows highest levels near the surface, the retrieval is more sensitive to the boundary layer, especially at low elevation angles. The retrieval is also less influenced by the effects of clouds that escaped the filtering process.

The theory of optimal estimation inversion techniques, which we adopted as the mathematical method to derive aerosol profiles, is based on the approximation of the physics of the measurement process by a forward model F . This model relates the measurement vector \vec{y} , i.e. O₄ DSCDs at various elevation angles, to the state vector \vec{x} , i.e. the vertical profile of the aerosol extinction coefficients:

$$\vec{y} = F(\vec{x}, b) + \varepsilon \quad (3.1)$$

Here b is the vector of parameters not optimized in the retrieval, such as albedo, aerosol optical properties, etc. ε is the error term encompassing both instrumental and model errors (Rodgers, 2000).

Optimal estimation is based on the retrieval of \vec{x} through minimization of the cost function $\chi^2(\vec{x})$, which compares modeled measurement from the real measurement considering errors and previous (*a priori*) knowledge of \vec{x} :

$$\chi^2(\vec{x}) = [\vec{F}(\vec{x}) - \vec{y}]^T \mathbf{S}_\varepsilon^{-1} [\vec{F}(\vec{x}) - \vec{y}] + [\vec{x} - \vec{x}_a]^T \mathbf{S}_a^{-1} [\vec{x} - \vec{x}_a] \quad (3.2)$$

\vec{x}_a is the *a priori* assumption of the state vector (Rodgers, 2000). S_ε and S_a are the measurement and *a priori* covariance matrices, respectively, which represent the uncertainty of \vec{y} and how well \vec{x}_a is known.

Since the effects of aerosols on atmospheric radiative transfer are inherently nonlinear, we have implemented a non-linear, numerical, iterative approach to solve the optimal estimation problem that is based on VLIDORT and the Levenberg-Marquardt optimization algorithm. The Levenberg-Marquardt method is a well-established fast optimization method with a fairly reliable convergence (Levenberg 1944, Marquardt, 1963). VLIDORT is called in each Levenberg-Marquardt optimization step, calculating a new state vector \vec{x}_i , and the Jacobian, i.e. the multiparameter gradient, \mathbf{K} , which in this case is the partial derivative of each measured O₄ DSCD with respect to aerosol optical depth per altitude:

$$\vec{\nabla} \vec{F}(\vec{x}) = \mathbf{K} = \frac{\partial \vec{y}}{\partial \vec{x}} \quad (3.3)$$

Each new state vector in the iteration is then calculated based on the following equation:

$$\vec{x}_{i+1} = \vec{x}_i + [(1 + \gamma)S_a^{-1} + K^T S^{-1} K]^{-1} \left[K^T S^{-1} (\vec{y} - \vec{F}(\vec{x})) - S_a^{-1} (\vec{x}_i - \vec{x}_a) \right] \quad (3.4)$$

Here γ is the parameter controlling the convergence of the Levenberg-Marquardt method. If at each step i there is a reduction in the cost function (i.e. the difference between the modeled DSCD and the measured DSCD is reduced), the retrieved state is accepted as the current step, and the iteration is repeated. If the cost function of the retrieved state is greater, the retrieval is rejected, and γ is increased, widening the search area over which a solution can be found. Convergence is reached when one of several possible conditions is reached. First, if the state vector \vec{x}_i shows a change of less than 10% in between an iterative step, it is considered to have converged into a final solution, as little improvement has been found to continue the iteration. In addition, if after a number of iterations there is no improvement, or if γ reaches too high of a level, the retrieval is halted and is assumed to have not reached a convergence.

We performed extensive tests of the performance of this retrieval method, using a number of theoretical profiles for our Mt. Wilson case. These tests were also used to determine the information content of the vertical aerosol profile retrievals one can expect for the various environmental conditions in Los Angeles.

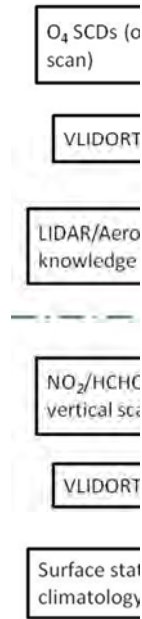


Figure 3.7: Schematics of the aerosol retrievals from the MAX-DOAS O₄ DSCDs.

3.7. Trace gas profile retrievals

Once the radiative transfer has been constrained and the aerosol extinction profile retrieved, the radiative transfer model can be run one more time, configured to simulate a trace gas DSCD and Jacobian matrix in order to determine the trace gas concentration profiles. Since this is a linear problem, the results can be directly calculated using the following equation (Rodgers, 2000):

$$\hat{x} = [\mathbf{K}^T \mathbf{S}_\epsilon^{-1} \mathbf{K} + \mathbf{S}_a^{-1}]^{-1} [\mathbf{K}^T \mathbf{S}_\epsilon^{-1} \vec{y} + \mathbf{S}_a^{-1} \vec{x}_a] \quad (3.5)$$

For the trace gas retrieval, the Jacobian K is the partial derivative of the observed trace gas DSCD at each elevation angle in a scanning sequence, with respect to the vertical concentration profile.

For the trace gas profiles, as well as for the aerosol extinction profiles, errors of the retrievals are also determined based on optimal estimation theory. It should be noted that these errors combine both the uncertainty of the measurements as well the uncertainty in the *a priori* profiles.

3.8. Information Content Analysis of Theoretical Retrievals

To better understand how much information can be retrieved from our observations we performed an information content analysis based on optimal estimation theory (Rodgers 2000). This allows the quantification of the number of pieces of information in a vertical profile that can be retrieved. In addition this analysis describes the sensitivity of our observations to different the altitudes in the atmosphere.

We calculate the gain matrix, G , which describes the sensitivity of the retrieval \hat{x} to the observations \vec{y} :

$$G = \frac{\partial \hat{x}}{\partial \vec{y}} = \hat{S}K^T S_e^{-1} \quad \text{where} \quad \hat{S} = (K^T S_e^{-1}K + S_a^{-1})^{-1} \quad (3.6)$$

Based on G we determine the averaging kernel A . The averaging kernel quantifies the impact of each state vector element on the retrieval, i.e. in our case the sensitivity of the retrieval to each height:

$$A = \frac{\partial \hat{x}}{\partial \vec{x}} = \frac{\partial \hat{x}}{\partial \vec{y}} \frac{\partial \vec{y}}{\partial \vec{x}} = GK \quad (3.7)$$

The averaging kernels provide information about the vertical sensitivity of a given height interval to every altitude layer in the true atmosphere (see color-coded in the figures in this section.) The averaging kernel elements ideally range from 0 to 1. Elements close to 1 indicate that the state vector at a given height interval is highly sensitive to the atmospheric state at this height. Elements close to 0 suggest that no information originates from this height interval. Averaging kernels elements outside of the 0 – 1 range are possible, and indicate that a given height level is either anti-correlated to or over-sensitive to a specific altitude. Typically the averaging kernel for each height interval is sensitive to a wide range of altitudes, with the highest sensitivity corresponding to the peak of the averaging kernel. The quality of the retrieval is thus closely related to the shape of the averaging kernels. For example, at altitudes in which all of the averaging kernels are close to zero, no information can be retrieved from the measurements and the profile is determined by the a-priori profile. This can be the case in atmospheres with high aerosol extinctions close to the surface, such as in our case.

A more simple measure of the information that can be obtained by an optimal estimation retrieval are the degrees of freedom (DoF). The DoF is the trace (or sum of the diagonals) of the averaging kernel matrix. It is often defined as the number of independent pieces of information that can be obtained by the retrieval, and informally acts as a scalar measure of the overall amount of information obtainable. Practically it is desirable to maximize the amount of information, which can be indicated by having higher degrees of freedom. As a simplification one can interpret the DoF as the number of height intervals that can be realistically be retrieved, although the optimal estimation method allow for higher vertical resolutions than is implied by the DoF.

Examples of a theoretical retrieval of aerosol extinction and NO_2 are shown in Figure 3.8 and Figure 3.9, respectively. In both cases we assumed measurement errors of 1%, close to those we derive from our Mt. Wilson observations.

In both figures the left panel shows the true, *a priori*, and retrieved profile. In addition, the uncertainties of the retrievals are shown as error bars. Please note that the error includes both the measurement error as well as the uncertainty of the a-priori profile, which was set to 50% in this case. The right panel shows the averaging kernel of the retrieval, illustrating the sensitivity of the retrieval to various altitudes. The right panel also lists the DoF which is 4.1 for the aerosol extinction profile and 4.5 for the NO_2 profile. This DoF means that the more than 4 pieces of unique information have been retrieved in both cases.

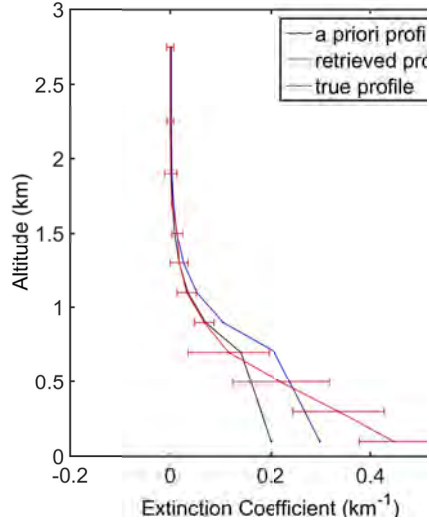


Figure 3.8: Example of theoretical aerosol retrieval of a typical Los Angeles aerosol profile and a measurement error of 1%. The retrieval algorithm has a number of degrees of freedom of 4.3, and is thus able to retrieve the profile with four pieces of independent information.



Figure 3.9: Theoretical retrieval of NO_2 vertical column densities from Mt. Wilson, using the aerosol extinction profiles used in the examples of theoretical aerosol retrievals (Figure 3.8). With an assumed low error of the NO_2 DSCD's of 1% up to 4.9 pieces of independent information can be retrieved.

3.8.1. Aerosol

To investigate how the retrieved information content varies with conditions in the LA Basin we performed a number of theoretical calculations to cover all of the possible cases we would encounter during our 4 year measurement period. It should be noted that this exercise is crucial as the retrieval will always find an aerosol or trace gas profile, but it is not always clear how much information originates from the measurements. The two most important parameters for the aerosol retrievals we considered are boundary layer height and the aerosol extinction content. We had briefly explored other optical aerosol properties, but found that those had less influence and also did not vary as much as extinction in Los Angeles. It should also be noted that boundary layer height and boundary layer aerosol extinction are not fully independent from each other, although we treated them as independent here, as the highest extinction coefficients can be expected primarily when the boundary layer is at its lowest height. This is well known for Los Angeles, where pollution levels are strongly linked to low inversion layer heights. We report the results of these calculations with respect to the DoF that can be retrieved for a vertical aerosol extinction profile in Table 3.3

Table 3.3: Theoretical DOFs for an aerosol extinction retrieval with a 1% measurement error and a 20% a-priori error.

		Aerosol Extinction Coefficient (km^{-1})				
		0.05	0.1	0.25	0.5	1.0
Boundary Layer Height (km)	0.1	3.66	3.63	3.56	3.41	2.93
	0.5	3.65	3.61	3.49	3.15	2.64
	1.0	3.63	3.56	3.35	2.77	2.09
	1.5	3.59	3.48	2.97	2.82	2.16
	2.0	3.57	3.43	2.81	2.42	1.62

As the DoF of the retrievals depend on the measurement and *a priori* error we also performed a sensitivity calculation for these two parameters (Table 3.4). As expected the DoF decreases as the measurement error increases. On the other hand, the DoF increases as the *a priori* error increases as more information will be added through the retrieval.

Table 3.4: Dependence of the theoretical DOFs of aerosol extinction retrievals on measurement and a priori error. These results were derived for a 1 km high boundary layer with an aerosol extinction of 0.1 km^{-1} .

		Measurement error				
		0.2%	0.5%	1%	2%	5%
<i>A priori</i> error	10%	3.94	3.12	2.37	1.50	0.65
	20%	4.49	3.94	3.42	2.65	1.50
	50%	4.89	4.34	3.94	3.42	2.37
	100%	5.23	4.77	4.35	3.94	3.20
	500%	5.73	5.23	4.89	4.49	3.94

3.8.2. NO_2

We performed similar test for the NO_2 retrievals. As NO_2 retrievals are also impacted by the aerosol extinction profile, we also considered this parameter. The first test was performed using a boundary layer height of 1km (Table 3.5). As with the aerosol retrievals the DoF depends strongly on the *a priori* and measurement error. For our current measurements the error is about 1%. Typically we use an *a-priori* error of 50% for our retrievals, allowing us to retrieve a maximum of 5 degrees of freedom in an ideal case for this viewing geometry.

Table 3.5: Theoretical DOFs from NO₂ concentration retrievals by measurement and a priori profile error for a boundary layer aerosol extinction of 0.1 km⁻¹ and a boundary layer height of 1 km

		Measurement Error				
		0.2%	0.5%	1%	2%	5%
<i>A priori</i> error	10%	4.95	4.07	3.31	2.36	1.16
	20%	5.59	4.73	4.07	3.31	2.05
	50%	6.23	5.59	4.95	4.28	3.31
	100%	6.69	6.12	5.59	4.95	4.07
	500%	6.98	6.90	6.69	6.28	5.59

We then used these results to determine the influence of boundary layer height, which is reflected in both the aerosol and NO₂ profile, and in the boundary layer NO₂ mixing ratios (Table 3.6). The impact of BLH and NO₂ is weak, with theoretical DoFs in the range of 4.6 – 5.3.

Table 3.6: Theoretical DOFs from NO₂ concentration retrieval by shape of a priori estimate of vertical concentration profile with a boundary layer aerosol extinction of 0.1 km⁻¹

		NO ₂ boundary layer concentration (ppb)				
		5	10	30	50	100
Boundary Layer Height (km)	0.1	4.62	4.75	4.94	4.98	5.01
	0.5	4.62	4.77	4.95	5.01	5.04
	1.0	4.65	4.81	5.01	5.10	5.12
	1.5	4.67	4.86	5.07	5.17	5.18
	2.0	4.73	4.96	5.20	5.31	5.27

Calculations were also performed to study the impact of the aerosol extinction, and thus atmospheric radiative transfer, on the information content of NO₂. For boundary layer NO₂ mixing ratios below 50 slightly higher DoF was found for larger aerosol extinction. While this increase was small, and will not be further discussed here, it generally leads to lower information content near the surface and higher information content at the top and above the boundary layer.

3.8.3. HCHO

Vertical profile retrievals of HCHO are strongly impacted by the higher measurement error of the HCHO DOAS retrieval. Because HCHO also absorbs at somewhat shorter wavelength we repeated the test performed for NO₂ also for HCHO (Table 3.7 and 3.8). As for NO₂ the results

depend strongly on the *a-priori error*. For our typical HCHO measurements the error of ~5% and an *a-priori* error of 50% we are able to retrieve 2.75 - 3 degrees of freedom in an ideal case. This means that we should be able to at least derive boundary layer averaged HCHO mixing ratios and HCHO mixing ratios above the boundary layer.

Table 3.7: Theoretical DOFs from HCHO concentration retrievals by measurement and *a priori* profile error for a boundary layer aerosol extinction of 0.1 km^{-1} and a boundary layer height of 1 km. HCHO measurement errors of 5 % are not uncommon

		Measurement Error				
		0.5%	1%	2%	5%	10%
<i>A priori</i> error	10%	3.87	3.20	2.32	1.17	0.50
	20%	4.43	3.87	3.20	2.03	1.17
	50%	5.31	4.63	4.04	3.20	2.32
	100%	5.79	5.31	4.63	3.87	3.20
	500%	6.50	6.16	5.89	5.31	4.63

Table 3.8: Theoretical DOFs from HCHO concentration retrieval by shape of a priori estimate of vertical concentration profile with a boundary layer aerosol extinction of 0.1 km^{-1} . The calculations presented here were performed with a 5% measurement error and a *a-priori* error of 50%.

		HCHO boundary layer concentration (ppb)				
		5	10	30	50	100
Boundary Layer Height (km)	0.1	2.75	2.89	3.20	3.43	3.37
	0.5	2.76	2.89	3.20	3.43	3.38
	1.0	2.76	2.90	3.22	3.44	3.39
	1.5	2.77	2.92	3.24	3.46	3.40
	2.0	2.79	2.95	3.28	3.49	3.43

3.9. Atmospheric Retrievals

After performing the theoretical information content calculations, we proceeded to analyze our observations from Mt. Wilson.

3.9.1. Aerosol

The non-linear Levenberg-Marquardt iteration (Section 3.6) was used in our aerosol retrievals. As in the theoretical case, our measurement vector consists of the measured O_4 DSCDs from a single elevation “scan”, all taken within 15 minutes of one another. Since the aerosol extinction in the Los Angeles basin is highly variable, selection of an *a priori* profile is challenging. If the *a priori* profile deviates greatly from the real profile, the retrieval may not converge and thus produce unrealistic profiles. To overcome that challenge, we have adopted a look-up table approach for the *a priori* to aid the retrieval as a first step. A combination of vertical profiles of varying aerosol extinctions and boundary layer heights was created at all possible solar geometries. VLIDORT was then run in a forward mode for every combination of those profiles to create a lookup table of O_4 DSCDs. The best *a priori* aerosol extinction profile was then selected by minimizing the difference between the look-up table and measured O_4 DSCDs. The table was calculated so that the differences between the loop-up table profiles is less than 50%, thus a 50% a-priori error was applied in all retrievals. Once the *a priori* profile is chosen, an aerosol extinction profile is retrieved. It should be noted that this is an iterative calculation and requires multiple calls to VLIDORT. It is thus the most computationally demanding step of the retrieval. However, we have made great progress in speeding up the retrieval in the past year and are now able to process a year’s worth of observations in about 10 days on one computer.

Figure 3.10 shows an example of an aerosol retrieval on July 2nd, 2011. In this case, the initial guess of the *a priori* is quite good. Nevertheless, the retrieval adds about 5 pieces of independent information to the profile. The right panel in Figure 3.10 shows the averaging kernel of the retrieval. In the case of a boundary layer aerosol extinction of 0.2, the sensitivity at the ground is low and the highest sensitivity is at an altitude of 1-2 km. Figure 3.11 shows another example of an aerosol retrieval a few days earlier, on May 31st, 2011. This is during a sunny, polluted day in the Los Angeles basin. Here the information content is limited to 3.6 pieces of information. Although the amount of information that can be retrieved decreases close to the ground, as is indicated by the averaging kernel, we can still obtain information down to roughly 400-500 meters above the surface. The uncertainty of the retrieved aerosol extinction profile is to a large extent determined by the 50% uncertainty attributed to the *a priori* profiles.

3.9.2. NO_2

The second step in our retrievals approach is the calculation of the NO_2 concentration profiles using the previously derived aerosol extinction profile using the method (Section 3.6). Since retrievals are based on a linear optimization algorithm, and the information content is greater for the trace gas retrievals, a look-up table was not used.

Figure 3.12 shows the result of the NO_2 retrieval for July 2nd, 2011, i.e. the same measurement as the extinction profile shown in Figure 3.10. The number of degrees of freedom, i.e. the amount of information added by the retrieval, is 3.9. The profile clearly shows the expected profile, with elevated NO_2 , (~ 24 ppb) within a nearly 700 m deep boundary layer. The averaging kernels show that the retrieval is sensitive from the surface to about 2 km altitude. Figure 3.13 shows

another NO₂ retrieval, this one much earlier in the morning. Here, the retrieval finds a much lower boundary layer height, as would be expected, and an elevated NO₂ concentration within the boundary layer. This retrieval also finds 4.3 pieces of information. Another interesting retrieval example is that from June 14, 2010 (Figure 3.14). During this day the Ceilometer deployed at Caltech showed a boundary layer height of ~500m, close to that derived from the MAX-DOAS. This is notable, as the a-priori assumed a higher boundary layer, which was consequently corrected by the retrieval. The surface NO₂ mixing ratios are equivalent to ~32ppb. The closest AQMD monitoring station at Azusa reported a very similar value of 31ppb at this time. This excellent agreement with surface observations is likely due to the high quality of the retrieval, which is reflected by the DoF of 4.6.

As with the aerosol retrieval, the actual information content may vary depending on a number of factors. Such factors include the atmospheric conditions or the error characterization of the retrievals, but in our current setup, we can consistently find between 3.5-4.2 degrees of freedom, with more or less information possible depending on exceptionally good or bad viewing conditions (Figure 3.15). The retrievals also indicate that the observations are sensitive to the boundary layer NO₂ concentrations, which is important for the comparison with surface observations in Section 3.10.

Figure 3.16 shows the retrieved profiles for several months in 2011. NO₂ concentrations vary greatly on a day to day basis. Changes in the boundary layer height, within the 200 meter vertical resolution of VLIDORT, are also common. We applied the retrieval methods described above to the entire 2011-2013 period. However, as the entire data-set is difficult to display, we will only show only part of the data here. The entire data-set will be available to the AQMD in electronic form at the end of the project.

Figure 3.10: Example of aerosol extinction retrieval on July 2nd, 2011. The number of degrees of freedom in this retrieval was 4.6. The Averaging Kernels are color coded according to the respective altitude intervals (legend is in km).

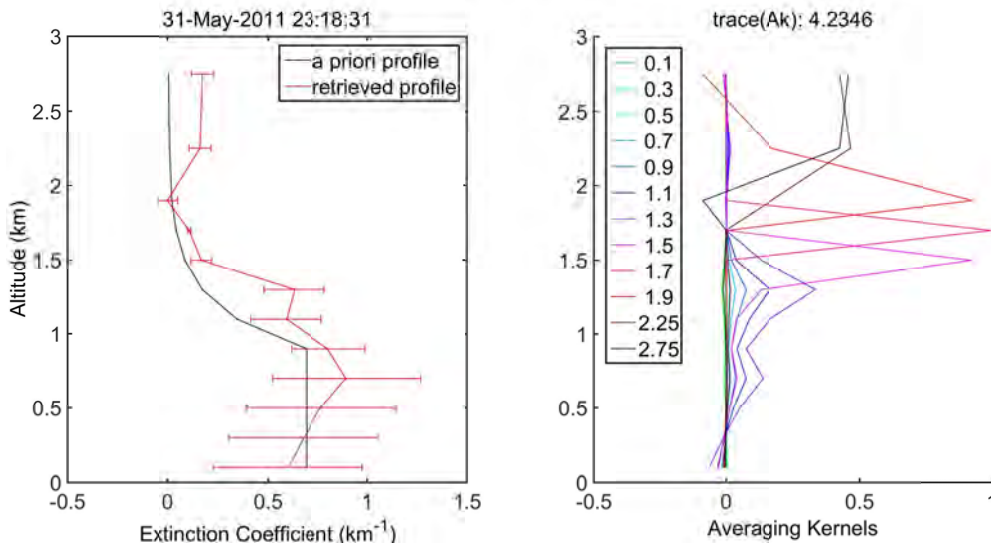


Figure 3.11: Example of an aerosol retrieval on May 31st, 2011. Note that this is in the afternoon, on a day with more sunshine. The number of independent pieces of information is 4.2. The averaging kernels are color coded according to the respective altitude intervals (legend is in km).

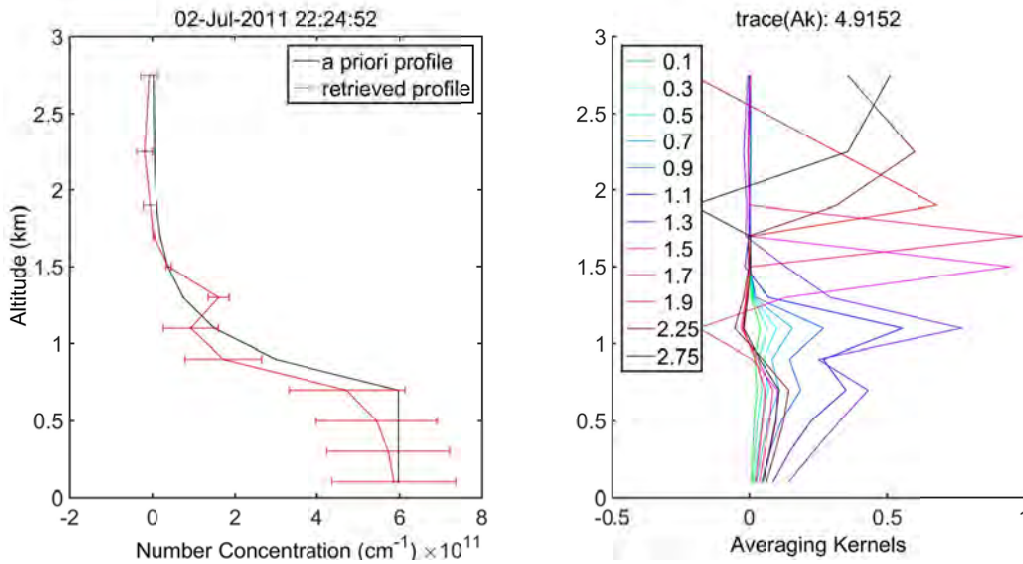


Figure 3.12: NO₂ profile retrieval for Mt. Wilson observation on July 2nd 2011. The surface NO₂ mixing ratios are equivalent to ~24 ppb of NO₂. The closest AQMD monitoring station in Azusa reported somewhat lower values of 15.4 ppb. The averaging kernels are color coded according to the respective altitude intervals (legend is in km).

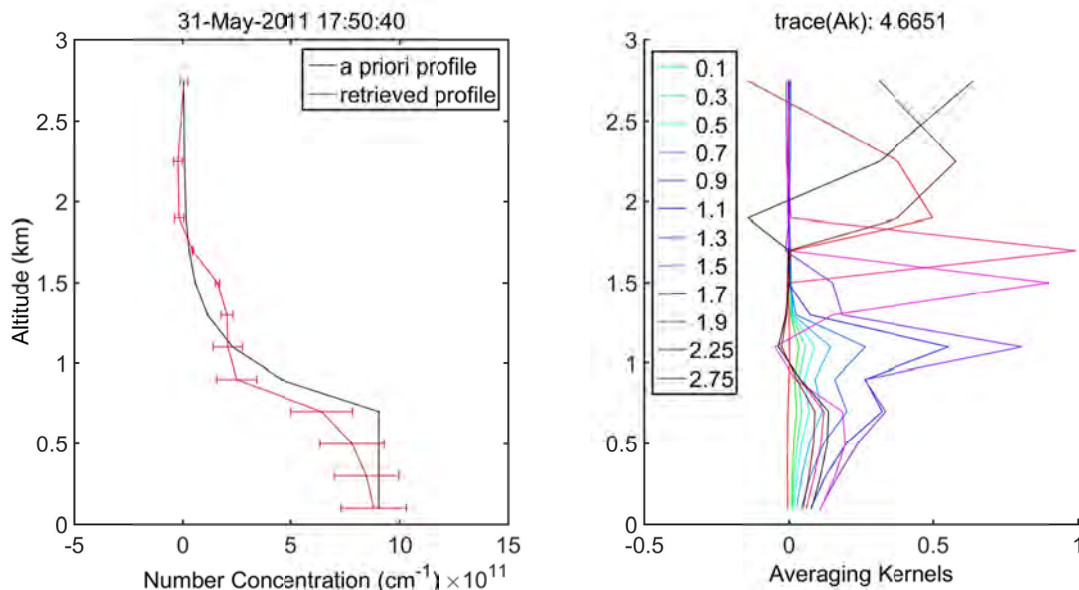


Figure 3.13: NO₂ profile retrieval for Mt. Wilson observation on May 31st 2011, at roughly 10 am PST. The surface NO₂ mixing ratios are equivalent to ~26 ppb of NO₂. This agrees quite well with the closest AQMD monitoring station in Pomona, somewhat downwind of our area of observation, which also measured 26 ppb of NO₂. The averaging kernels are color coded according to the respective altitude intervals (legend is in km).



Figure 3.14: NO₂ profile retrieval for Mt. Wilson observation on June 14th. The surface NO₂ mixing ratios are equivalent to ~32ppb. The closest AQMD monitoring station in Azusa reported a very similar value of 31ppb at this time.

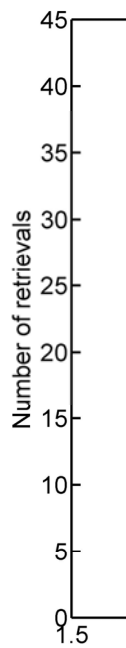


Figure 3.15: Statistics of information content analysis for NO₂ retrievals in June and July 2011. In general 3-4 pieces of information can be retrieved from Mt. Wilson.

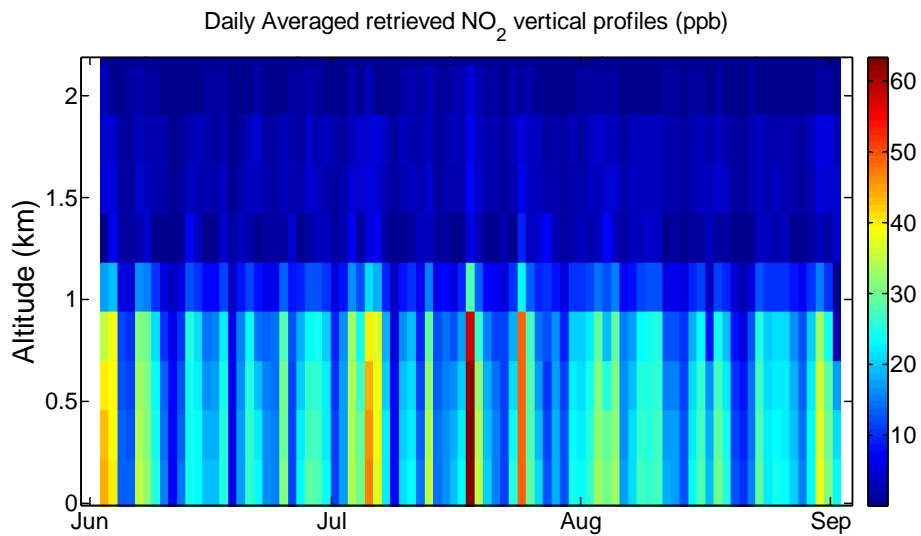


Figure 3.16: Daily averages of the retrieved NO₂ vertical profiles for the summer of 2011.

3.10. Comparison with surface measurements

3.10.1. Aerosol

In the following section, we will compare our retrievals to observations from an AERONET station operated by UCLA on the Caltech campus. The AERONET station was installed in early 2010, before the start of the CalNex experiment. While it has been operated at Caltech since that time, there are numerous gaps in data from when the instrument was at NASA for calibration. Some periods were also impacted by reduced performance of the instrument, in particular the UV. It should be noted that the AERONET Station and the Mt. Wilson MAX-DOAS do not sample the same air mass, but they are within 10 miles of each other. One would thus expect some differences, with the MAX-DOAS likely measuring higher extinctions as it is located further east.

To compare the aerosol extinction retrieval with the aerosol optical thickness, AOT, from the AERONET station, we integrated the extinction profile retrieved from the MAX-DOAS data vertically. Figure 3.17 and Figure 3.18 show two days of this comparison during the CalNex period for which we were certain that the AERONET station was operating accurately and no clouds were present. During June 2nd (Figure 3.17) there is very good agreement between the two methods. The DOAS data is ~15% higher, a difference that is likely due to a difference in the location of the two instruments.

The retrievals for June 3rd, 2010 were not as accurate as the previous example (Figure 3.18). On that day, several data points did not agree well with the AERONET station. We believe that horizontal inhomogeneities and/or clouds that were not correctly identified are the likely cause of that behavior. We are able to identify these problematic retrievals based on the χ^2 of the retrieval, but left them in the plot to illustrate the limitations of our method.

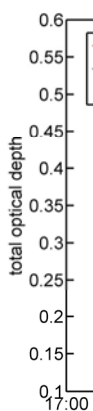


Figure 3.17: Comparison of AOT retrievals from the AERONET sun-photometer at Caltech and the AOT retrieved from the MAX-DOAS O₄ observations on June 1st.

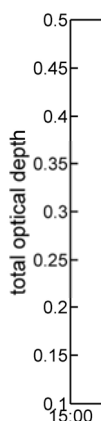


Figure 3.18: Comparison of AOT retrievals from the AERONET sun-photometer at Caltech and the AOT retrieved from the MAX-DOAS O₄ observations on June 3rd.

3.10.2. NO₂

As NO₂ was our main target trace gas, we also performed comparisons with surface station data. It should be noted that these retrievals inherently include the aerosol profile retrievals. Since our focus has been on the long-term trends and to avoid problems with the diurnal and spatial variation of the NO₂ concentrations, we performed this comparison using daily averaged NO₂ concentration retrieved at the 500 meter grid box using our NO₂ retrievals. The 500 meter grid box was found to consistently be well representative of the boundary layer concentrations of NO₂, which our retrievals indicated were relatively well mixed. Part of the rationale for choosing the 500 meter grid box was that our sensitivity studies have suggested that the MAX-DOAS is more sensitive to NO₂ concentrations at this altitude than it is towards NO₂ concentrations at the ground. The comparison in 3.19 was conducted over the central three azimuth angles (160°, 172.45°, and 182°) for greater temporal resolution. We have found that these azimuth angles probe similar air masses, and, in practice, the MAX-DOAS measurements have been found to be almost identical. Figure 3.19 compares retrieved data during the summer of 2011 daily averaged Pomona ground monitoring station, slightly to the east of the area we were measuring (for most of this period, the data for the monitoring station at Azusa was not available). As our retrievals revealed boundary layer NO₂ is typically well mixed, which is in agreement with our understanding of the physics and the meteorology of the boundary layer. Thus, the NO₂ values at the 500 meter grid box are similar to the values observed below and slightly above 500 meters. The reported daily average NO₂ concentration is weighted by the inverse of final cost function of the NO₂ retrieval, thus giving more weight to the better the retrievals throughout one day. As one would expect, lower cost functions (i.e. the better the agreement between the modeled and observed NO₂ DSCDs) are indicative of a better agreement between our retrieved concentration and the observations from the Pomona station. This not only suggests that the cost function can be used as a measure of the quality of our measurements, but also a value for further improvements in the convergence of our retrievals. In general the agreement between the surface station and retrieved concentration is quite good, considering the

difference in location and the path-averaging of the MAX-DOAS data. Further analysis will be required to determine where the differences stem from.

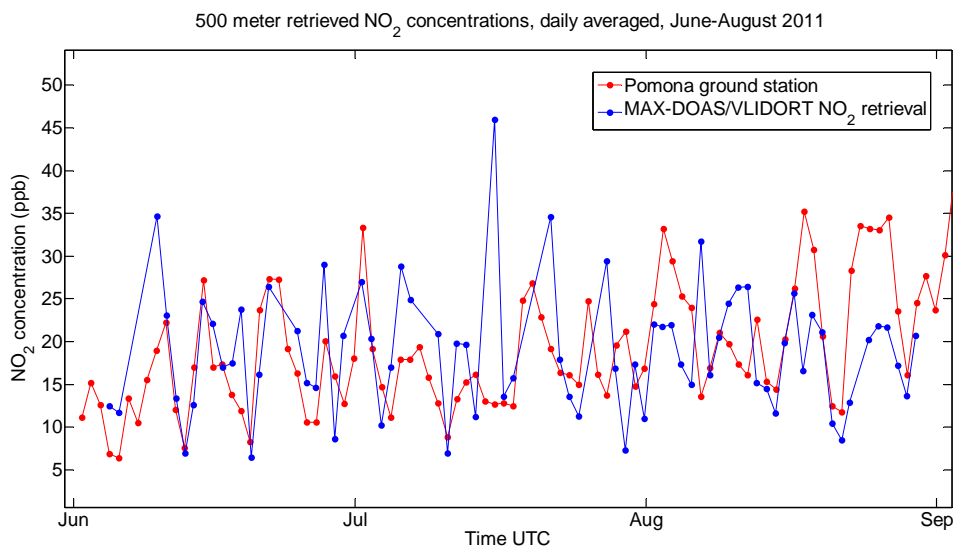


Figure 3.19: Comparison of the daily averaged NO_2 concentrations between our NO_2 concentrations retrieved in the boundary layer, and the NO_2 concentrations measured by the nearby Pomona ground station.

3.11. HCHO to NO_2 ratios as marker for ozone production efficiency

Our sensitivity studies, and the real-world retrievals, have shown that the MAX-DOAS DSCDs for NO_2 and HCHO, i.e. the path integrated trace gas concentrations, are predominately due to the trace gas absorptions in the boundary layer, where their concentrations are much larger than in the free troposphere. We have also found from our analysis and observations during CalNex that both trace gases are fairly well mixed in the boundary layer. Because we are able to measure both compounds in the same wavelength interval (323.4–350nm) we can thus directly interpret the ratio of the HCHO DSCD and the NO_2 DSCD as being representative of the boundary layer-averaged HCHO/ NO_2 concentration ratio. Any radiative transfer effects will be minimized in the HCHO/ NO_2 DSCD ratio. An interesting application resulting from that finding is the use of the HCHO to NO_2 DSCDs ratio to study ozone chemistry in the Los Angeles basin (Duncan et al. 2010; Martin et al, 2004). This approach was originally proposed by Martin et al (2004) and further investigated by Duncan et al (2010), who related the HCHO/ NO_2 ratio to the VOC or NO_x sensitivity of ozone formation. Based on model calculations for the Los Angeles area Duncan et al (2010) used $\text{HCHO}/\text{NO}_2 < 1$ as an indicator of VOC sensitivity, i.e. reductions in VOCs lead to a reduction in ozone, while $\text{HCHO}/\text{NO}_2 > 2$ were indicative of NO_x sensitivity, i.e. NO_x reductions reduce ozone formation. The HCHO/ NO_2 range between 1 and 2 is indicative of an ozone decrease upon reduction of both VOC and NO_x .

Kleinman et al. (1997) introduced a formalism to determine the sensitivity of ozone formation of NO_x vs. VOC based on an analysis of ozone formation chemistry. They relate the cross-over point between the two different sensitivities to the point where the sum total radical production

rate, Q , is twice the rate of radical removal by reactions of the radical + NO_x , L_N , i.e. $L_N/Q=0.5$. L_N/Q thus distinguishes low- NO_x conditions under which radicals are primarily removed by peroxide formation from high- NO_x condition where the radical reactions with NO_x dominate, i.e. L_N/Q smaller than 0.5 is indicative of a NO_x sensitive system, while $L_N/Q > 0.5$ is indicative of a VOC sensitive regime

To provide a better estimate of the limiting value between the two sensitivity regimes we used the CalNex surface measurements to determine the cross-over HCHO/NO_2 value based on surface observations of all relevant parameters. It is beyond the scope of this report to give details on the various observations and the underlying calculations. However, Figure 3.20 shows that L_N/Q , a common marker for VOC vs NO_x sensitivity (Kleinman et al., 1997, 2001, 2005), is closely related to HCHO/NO_2 ratios from the surface observations at Pasadena.

Kleinman et al. (1997) report that L_N/Q smaller than 0.5 is indicative of a NO_x sensitive system, while $L_N/Q > 0.5$ is indicative of a VOC sensitive regime. Based on Figure 3.20, the $L_N/Q=0.5$ cross-over value translates to a HCHO/NO_2 cross-over value for Los Angeles in the May-June time period of 0.55. It should be noted that this value is considerably lower than the one used by Duncan et al. (2010). However, our value was determined from observations and not from model calculations and is thus likely more accurate.

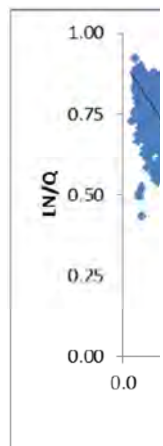


Figure 3.20: Plot of HCHO/NO_2 vs. L_N/Q for the surface observations during CalNex. (P. Stevens, Univ. Indiana, pers. communication, unpublished data)

We first applied the HCHO/NO_2 ratio approach to our observations during the CalNex field experiment (Figure 3.21) for -4° and 0° elevation angle and 182° azimuth observations. For both viewing directions, a clear difference between weekdays and the weekend (gray bars) can be seen. On weekdays, the HCHO/NO_2 ratio typically between 0.1 - 0.2 for the -4° elevations and somewhat higher for the 0° elevation, thus clearly in a VOC limited regime. In contrast weekend values are closer to the threshold value for the -4° elevation and often exceed the threshold value for the 0° elevation. The observations indicate a clear change in ozone sensitivity between weekdays and weekends. This “weekend effect” is well known and leads to higher ozone mixing ratios in the Los Angeles Basin (Marr et al, 2002; Murphy et al., 2007).

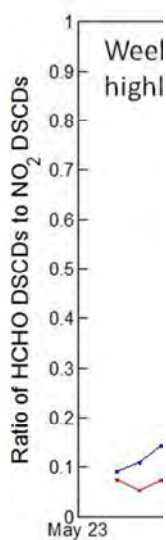


Figure 3.21: Daily averaged HCHO/NO₂ ratio measured from Mt. Wilson during the CalNex experiment

While the CalNex data is quite interesting, the true value of our observations lies in the observations of long-term trends in the HCHO/NO₂ ratio. We therefore calculated the monthly averages of the NO₂ and HCHO DSCDs as well as of the HCHO/NO₂ ratio for our observations for the years 2011-2013 (Figure 3.22). The first interesting observation is the clear difference between weekday and weekend NO₂ and the absence of such a dependence for HCHO. That observation is further illustrated in the hourly averaged values for 2011 shown in Figure 3.23. This is explained by a change in NO_x emissions on the weekends, likely due to the lower truck traffic. The VOC emissions, for which HCHO is a proxy, do not seem to show a weekend-effect. Another interesting aspect of the NO₂ data is the seeming decrease of the weekday DSCDs from 2011 to 2013. While this data still contains radiative transfer effects a comparison with the weekend data (Figure 3.24) further illustrates this change. At the beginning of 2011 the weekday/weekend ratio of NO₂ is around 1.8-2.2, while at the end of 2013 it has decreased to about 1.2-1.6. The reduction of NO₂ in the LA basin thus seems to have predominately occurred during the weekdays. This decrease of around 10±3% per year is similar to that observed by Russel et al. [2010]. However, our weekend change appears to be smaller. One can speculate that cleaner trucks or reduced truck traffic could be responsible for this phenomenon.

The seasonal trend in the HCHO/NO₂ ratio shows clear maxima during summer and minima during the winter, with highest values in August/September. The exact explanation for this seasonal dependence is still under investigation but it is most likely due to changes in VOC emissions and oxidation rates, as indicated by the seasonal dependence of the HCHO DSCD. It should be noted that the DSCD values integrate the trace gases in the vertical, thus eliminating the influence of meteorology, i.e. the seasonal dependence of the boundary layer height. The results seem to indicate that during the summer, the LA atmosphere is more in a NO_x limited regime than during the winter. As during the CalNex case the weekend HCHO/NO₂ ratios are

higher than those for the weekdays. Generally, weekends are in a more NO_x sensitive regime than weekdays. There does not seem to be a statistically significant long-term trend in the HCHO/NO₂ ratios. A comparison of the weekday-weekend HCHO/NO₂ ratio also does not seem to indicate a significant change between 2011 and 2013. It thus appears that the ozone sensitivity regime is not substantially changing, likely due to a decrease in HCHO (or VOCs) accompanying the NO₂ decrease. It would be interesting to further follow the HCHO/NO₂ ratio in Los Angeles to identify how the ozone sensitivity changes in the future.

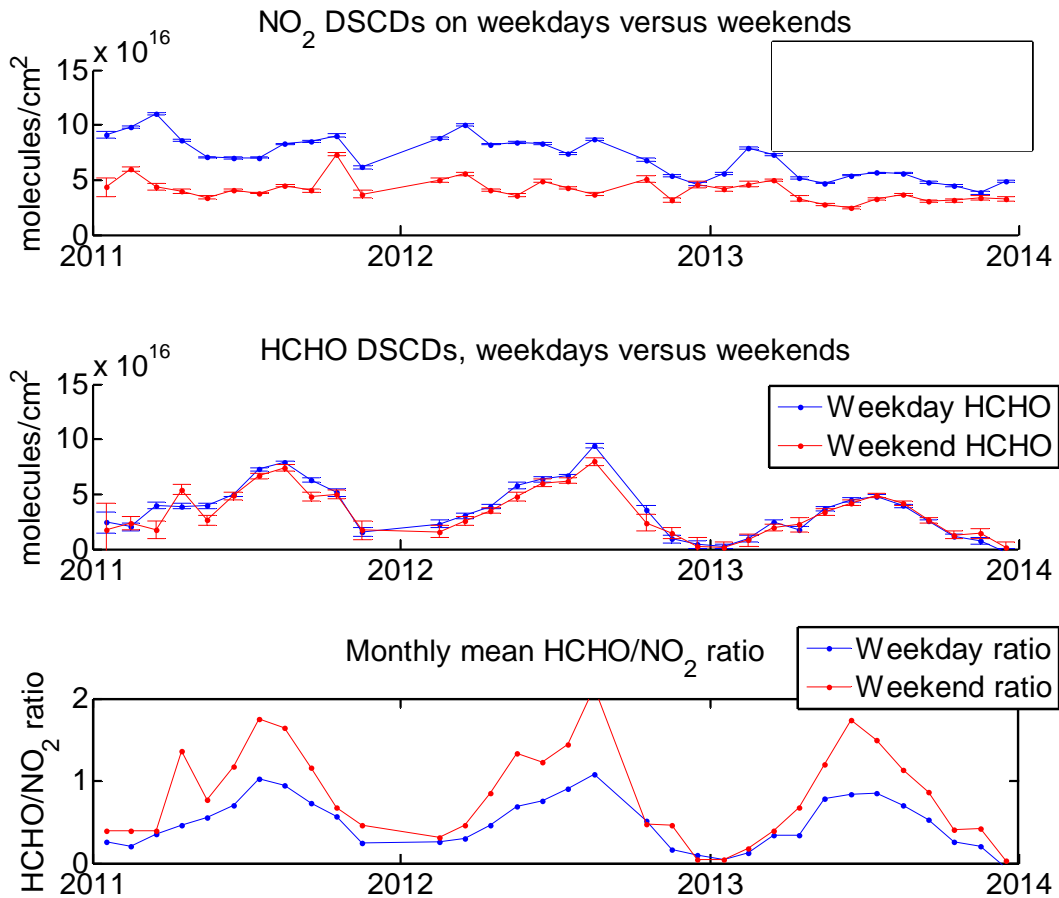


Figure 3.22: Monthly averaged DSCDs of HCHO and NO₂ and HCHO/NO₂ ratio in the Los Angeles Basin observed from Mt. Wilson. A clear seasonal cycle can be observed in the HCHO and HCHO/NO₂ data, with highest ratios in later Summer to early Fall. The weekend effect is most pronounced during the summer periods. Please note that the weekend data is based on fewer data points and thus shows more month to month variability.

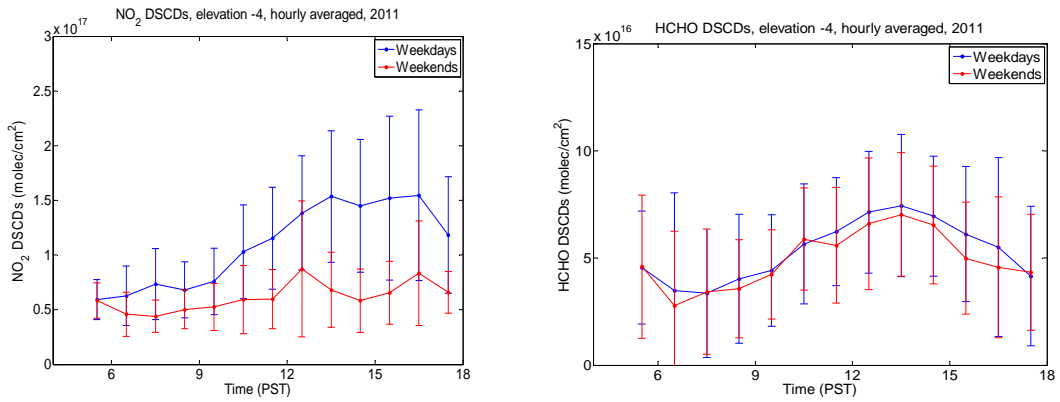


Figure 3.23: Hourly average NO₂ and HCHO DSCDs during 2011. Blue lines show weekday data, red lines show weekend data. Error bars indicate the variation in the observations, including those caused by radiative transfer effects.

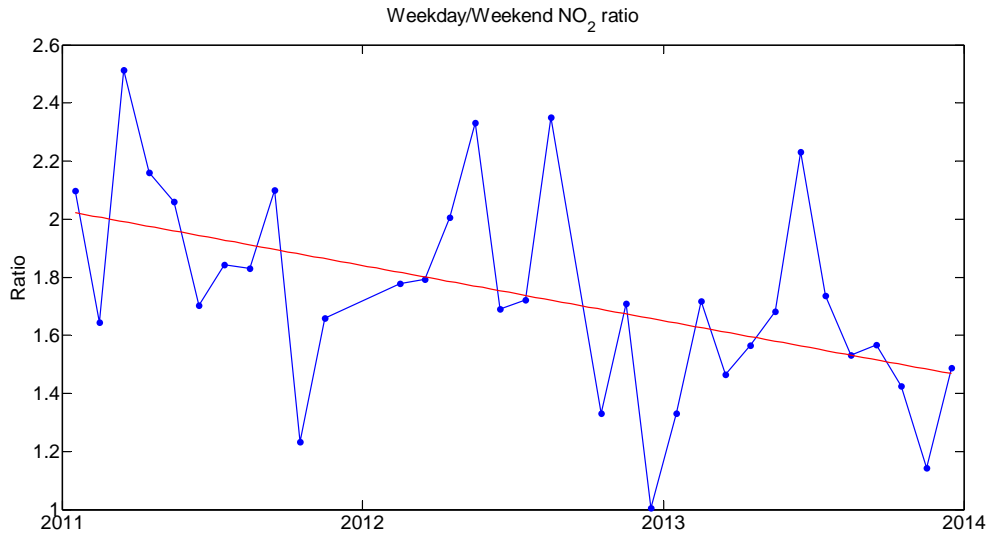


Figure 3.24: Weekday/weekend monthly averaged NO₂ DSCD ratio for the years 2011-2013. The scatter in the data is caused by the higher variability in the weekend data due to fewer data points used in the average. Nevertheless a clear downward trend can be observed.

4. Near-IR Fourier Transfer Measurements of Greenhouse Gases

The Los Angeles basin is a very large anthropogenic source of the important greenhouse gases CO₂ and CH₄, which contribute significantly to regional and global climate change (Hoornweg, 2010). Recent legislation in California, the California Global Warming Solutions Act (AB32), mandated a statewide cap for greenhouse gas emissions in 2020 at levels that prevailed in 1990 (Croes, 2012). Verifying the effectiveness of regional greenhouse gas (GHG) emission control requires high-precision, regional-scale measurement methods combined with models that capture the principal anthropogenic and biogenic sources and sinks. The existing California Air Resources Board (CARB) GHG measurement sites in the Los Angeles area are sparse, with far fewer sites than the CARB air quality network. Instruments in the network sample near the surface, where perturbations from local traffic sources, wind fields and planetary boundary layer (PBL) height changes can induce considerable variability in measured GHG concentrations on short time scales. McKain et al. (2012) used the coupled Weather Research and Forecasting – Stochastic Time-Inverted Lagrangian Transport (WRF–STILT) model to compare the sensitivity of surface and total column measurements of CO₂ to changes in emissions within the Salt Lake City urban dome. Their simulations indicated that column measurements from the ground or space are more sensitive to emissions from the greater urban region than surface point measurements, and less sensitive to variability in PBL height. Thus, column measurements may allow for more precise estimation of anthropogenic emission trends in cities. Kort et al. (2012) analyzed space-based observations of the column-averaged dry-air mole fractions of CO₂ from Greenhouse Gases Observing Satellite (GOSAT) over Los Angeles and Mumbai. Despite the relatively sparse spatial and temporal resolution and coverage provided by GOSAT, the column measurements showed statistically significant gradients between the cities and the surrounding areas which could be used to detect emission changes of a few percent per year over a 5-10 year observation period.

Despite the advantages inherent in the measurement of integrated column abundances, existing satellite and ground-based remote sensing instruments do not provide the temporal and spatial coverage required to quantify megacity GHG emissions. The repeat cycles and swaths of the orbital tracks of space-based instruments in low Earth orbits (e.g. GOSAT currently in orbit, Orbiting Carbon Observatory-2 (OCO-2) to be launched in July, 2014) do not provide daily monitoring of GHG emissions over megacities. There are also very few ground-based remote sensing instruments for column GHG measurements. The Total Carbon Column Observing Network (TCCON) is a collection of ground-based Fourier Transform spectrometers recording direct solar spectra in the near-infrared spectral region to measure the column-averaged volume mixing ratio (VMR) of GHGs. However, most TCCON stations are deployed at rural sites with small spatial gradients in order to provide calibration/validation data for satellite missions. Wunch et al. (2009) estimated the emission rates of GHGs over the LA basin using measurements from a TCCON station that was temporarily located in Pasadena, California. However, since TCCON stations employ direct solar viewing geometry, the spatial coverage of a single spectrometer is quite limited. This highlights the need for an approach that can produce daily GHG column abundance measurements over a wide spatial domain to complement other sensor networks in an urban air-shed.

Here, a novel observing system that addresses the requirements for wide-area monitoring of GHGs to assess the impact of control measures on long-term megacity carbon emissions. The

approach involves the use of a high resolution FTIR spectrometer on a mountaintop looking over the Los Angeles basin to record atmospheric solar absorption spectra from a number of geographically distributed target points. The mountaintop viewing geometry offers two significant advantages relative to direct solar measurements from ground sites in the boundary layer: enhanced sensitivity to composition changes within the boundary layer due to the long low-altitude optical path lengths (tens of km), and the capability to independently measure the composition within the free troposphere to provide background reference information. Apart from differences in viewing angles, the mountaintop vantage point also closely approximates the observations from geostationary orbit by space missions that will be launched later this decade (Key et al. 2012).

This section of the report is organized as follows: Section 4.1 describes the measurement technique. Section 4.2 describes the data processing algorithms, examples of retrievals, and error analysis. Section 4.3 describes the diurnal variations of XGHG. Section 4.4 describes the spatial variations of XCH₄:XCO₂ excess in the Los Angeles basin, and estimations of GHG emission inventory in the Los Angeles basin. Section 4.5 describes the comparisons between the FTS observations and modeling results from the atmospheric 3D model, WRF-VPRM. Section 4.6 outlines directions for future work..

4.1. Measurement Technique

The California Laboratory for Atmospheric Remote Sensing (CLARS) is a NASA/Jet Propulsion Laboratory facility located on the grounds of Mount Wilson Observatory at 1673 meters above sea level. A Fourier Transform Spectrometer was designed and built at Jet Propulsion Laboratory (JPL) for use in the measurements at CLARS. The CLARS-FTS is optimized for reflected sunlight measurements with high spectral resolution in the near-infrared (NIR) region (4,000 – 15,000 cm⁻¹).

Two operating modes are on the CLARS-FTS measurement schedule: Los Angeles Basin Surveys (LABS) and Spectralon® Viewing Observations (SVO). In LABS mode, the pointing system stares at each ground site in the Los Angeles basin and CLARS-FTS records atmospheric absorption spectra over a broad spectral range (4,000 – 8,600 cm⁻¹) using reflected sunlight as the light source. SVO provide the background level of GHG gases. In SVO, CLARS-FTS measures the greenhouse gas concentration above the CLARS site by pointing at a Spectralon® target on the rooftop. Since the CLARS mountaintop site is located above the boundary layer, SVO measurements give the background trace gas abundances in the free troposphere. In the downward viewing geometry used in the CLARS-FTS measurements, the sunlight travels through the boundary layer twice: once on the way to the target and a second time from the target to CLARS. The resulting light path through the boundary layer is typically greater than 20 km which is several times longer than other commonly used viewing geometries, e.g., observing the direct solar beam from the surface, or measurement of surface-reflected sunlight from aircraft and spacecraft.

Daily measurements from CLARS-FTS follow a pre-programmed sequence, in which the CLARS pointing system either directs light reflected from the targets in the Los Angeles basin (LABS mode) or the Spectralon® plate on the rooftop of CLARS site (SVO mode) into the spectrometer. The sequences can be changed to accommodate the needs of special observations. The measurement sequence is repeated ~5-8 times daily. Details of the measurement technique are described in Fu et al. (2014).

4.2. Data Processing and Error Analysis

4.2.1. Interferogram to Spectrum

CLARS-FTS records single-sided interferograms with uniform-time sampling in both the IR and reference channels. The CLARS interferogram processing program (CLARS-IPP) converts interferograms (Level 1a data) into spectra (Level 1b data). The CLARS-IPP algorithm applies the following post-processing steps to each recorded scan: (1) converts time-domain interferogram to path-difference domain interferogram; (2) corrects for solar intensity variations (SIV); (3) corrects phase error, and (4) converts the interferogram into a spectrum using the Fast Fourier Transform (FFT) algorithm (Fu et al., 2014).

A pre-screening step removes individual spectra of low quality, e.g., scenes likely contaminated by clouds. The cloud scene pre-screening of single-scan CLARS-FTS measurement is performed by comparing the intensities of spectral radiances between adjacent scans to identify outliers. Single-scan spectra are then co-added over a period of 3 minutes (12 single-scan spectra), to increase the signal-to-noise ratio (for LABS $\geq 300:1$, for SVO $\geq 450:1$). Depending on the season, the total number of co-added spectra within a single day ranges from 160 to 260 repeating the number of LABS measurement sequences from 5 to 8 times.

4.2.2. Spectrum to Slant Column Densities (SCD) of Trace Gases

To derive slant column abundances of atmospheric trace gases from the measured absorption spectra, we use a modified version of the GFIT program. GFIT is derived from the Occultation Display Spectra (ODS) program (Norton and Rinsland, 1991), which was created for the analysis of Atmospheric Trace Molecule Spectroscopy Mission (ATMOS), and incorporates many improvements. Since the viewing geometry of CLARS-FTS measurements differs from the SVO viewing geometry used by TCCON, several modifications are needed. These modifications were applied to the GFIT February 2013 version. The modified GFIT program consists of a radiative transfer (RT) model coupled to a model of the solar spectrum to calculate the monochromatic spectrum of light that originates from the sun, passes through the atmosphere, and reflects from the Earth's surface.

We retrieve CO₂, CH₄, CO, and O₂ using the spectral bands and the sources of spectroscopic parameters that are listed in Table 4.1, similar to those used by TCCON. The uncertainties of measured XGHG from the errors in spectroscopic parameters and other sources are estimated in section 4.5.2. For O₂, the a priori VMR profile is constant with altitude (a dry-air VMR of 0.2095). For CO₂, CH₄ and CO, the assumed a priori VMR profiles vary seasonally in agreement with model output from Olsen and Randerson (2004). The sensitivity of the column GHG retrievals to different reasonable a priori functions, is expected to be within 1% based on the previous study of Washenfelder et al. (2006).

Nitrous oxide, N₂O, is an important atmospheric greenhouse gas emitted primarily by biological processes involving plants and soils, and by biomass burning. The contribution to the global background from stationary and mobile combustion sources is highly uncertain and has been identified by CARB as a high-priority research area. CLARS-FTS measures N₂O in two spectral windows: 4373-4471 cm⁻¹, and 4418-4442 cm⁻¹. The N₂O retrievals are typically very precise, on the order of 1-2 ppbv. However, as with the other greenhouse gases that are retrieved by the FTS, aerosol scattering introduces a systematic error that increases with distance to the reflection point. Because the N₂O spectral bands lie at significantly longer wavelengths than the

O₂ band which is used to filter out measurements affected by aerosols, it is difficult to discriminate aerosol effects from actual atmospheric N₂O enhancements, which are quite small. For this reason, N₂O is not a standard CLARS-FTS data product at the present time. Research is ongoing to develop an aerosol scattering model which can provide a first-order correction to the N₂O retrievals, and possibly provide a useable N₂O data product in the near future.

Table 4.1: CLARS FTS Measurement Sequence

index	Target Coordinate			Target Name	Measurement
	Latitude (degree)	Longitude (degree)	Altitude (meter)		
0	34.221	-118.057	1673	Spectralon®	SVO ¹
1	34.069	-117.390	340	Fontana	LABS ²
2	34.081	-117.589	325	Rancho Cucamonga	LABS
3	33.951	-117.392	265	Riverside	LABS
4	33.877	-117.416	403	Lake Matt	LABS
5	33.962	-117.573	190	Norco	LABS
6	34.043	-117.725	253	Pomona	LABS
7	34.120	-117.868	217	210 Bend	LABS
8	33.868	-117.601	261	Corona	LABS
0	34.221	-118.057	1673	Spectralon®	SVO
9	33.863	-117.776	97	North OC	LABS
10	34.000	-117.883	151	60 Industry	LABS
11	34.110	-117.969	134	Santa Fe Dam	LABS
12	33.678	-117.864	12	OC Airport	LABS
13	33.800	-117.883	47	Angels Stadium	LABS
0	34.221	-118.057	1673	Spectralon®	SVO
14	33.722	-117.975	12	Huntington Beach	LABS
15	33.910	-118.006	57	La Mirada	LABS
16	34.030	-118.025	77	605 and 60	LABS
17	34.141	-118.042	155	Santa Anita Park	LABS
18	33.821	-118.195	11	Long Beach 405	LABS
19	33.930	-118.158	30	Downey	LABS
20	34.048	-118.116	128	ELA water	LABS
0	34.221	-118.057	1673	Spectralon®	SVO
21	33.810	-118.368	66	Palos Verdes	LABS
22	33.990	-118.400	8	Marina Del Rey	LABS
23	34.054	-118.305	58	Downtown Far	LABS
24	34.102	-118.234	124	Downtown Near	LABS
25	34.093	-118.470	257	Santa Monica	LABS
26	34.154	-118.273	160	Glendale	LABS
27	34.170	-118.165	293	West Pasadena	LABS
28	34.141	-118.353	170	Universal City	LABS

¹Spectralon® Viewing Observations²Los Angeles Basin Surveys

In order to characterize the precision of CLARS-FTS measurements, special observations were conducted which cycled between the Spectralon® target and two nearby reflection points in the LA basin, Santa Anita Park (a horse racing track in the city of Arcadia) and west Pasadena. These targets are labeled #0, #17 and #27, respectively, in Table 4.1 and Figure 4.1). Figure 4.2 shows typical spectral fits of CO₂ bands near 1.6 μm using the CLARS-FTS measurements pointing at Spectralon® (top panels), Santa Anita Park (middle panels) and west Pasadena (bottom panels). The spectral fits were made using two CO₂ bands (blue lines) centered at 6220 cm⁻¹ (noted as MW6220 thereafter) and 6339 cm⁻¹ (noted as MW6339 thereafter) separately. The root mean square (RMS) of the spectral fitting residuals in both CO₂ bands are reasonably close to the expected values since the Chi-squared tests of spectral fitting residuals yielded values generally within 1.3 (Figure 4.3). The RMS of spectral fitting residuals shows a dependency on the spectral SNR (Figure 4.3). Figure 4.4 shows the averaged spectral fitting residuals within MW6220 and MW6339 using the measurements over three targets on January 3rd, 2013. The co-addition of fitting residuals reduces the random spectral noise contribution and preserves the systematic fitting residuals. The systematic fitting residuals were observed in the measurements from all LA basin targets as well as the Spectralon® target. The majority of the “spikes” in the left panels of Figure 4.4 arise from imperfect line parameters of disk integrated solar lines and H₂O lines, although some of the systematic residuals arise from errors in the spectroscopic parameters of CO₂ and neglect of line mixing. In addition, uncertainties in atmospheric temperature, pressure and humidity profiles arising from the limited spatial/temporal resolution of National Center for Environmental Prediction (NCEP) data contribute to systematic residuals, especially for water vapor lines. Overall, the magnitude of the systematic residuals is smaller than 0.5% of the spectral continuum levels with peak values most often appearing at the wavelength of non-target species such as H₂O. The imperfect spectroscopic parameters and line shape function affect the accuracy of retrieved GHG column amounts since they can bias the retrieved GHG column abundances. Most of this bias can be corrected by calibration against secondary measurements. Wunch et al. (2010) discussed a calibration procedure for TCCON measurements, which use the same spectroscopic parameters as the work that reduced the systematic bias for CO₂ from 1.1% to 0.2% and CH₄ from 2.2% to 0.4%.



Figure 4.1: Upper panel: Schematic diagram of spectrometer (altitude of 1.7 km) viewing geometry for Los Angeles Basin Surveys (LABS) and Spectralon® Viewing Observations; lower panel: the target site location of CLARS-FTS observations in a measurement sequence over Los Angeles Basin. Blue balloon indicates CLARS site; Yellow pins showed the target site location. The measurement sequence is being repeated daily for ~5-8 times. The sequences can be changed to accommodate the needs of special observations.

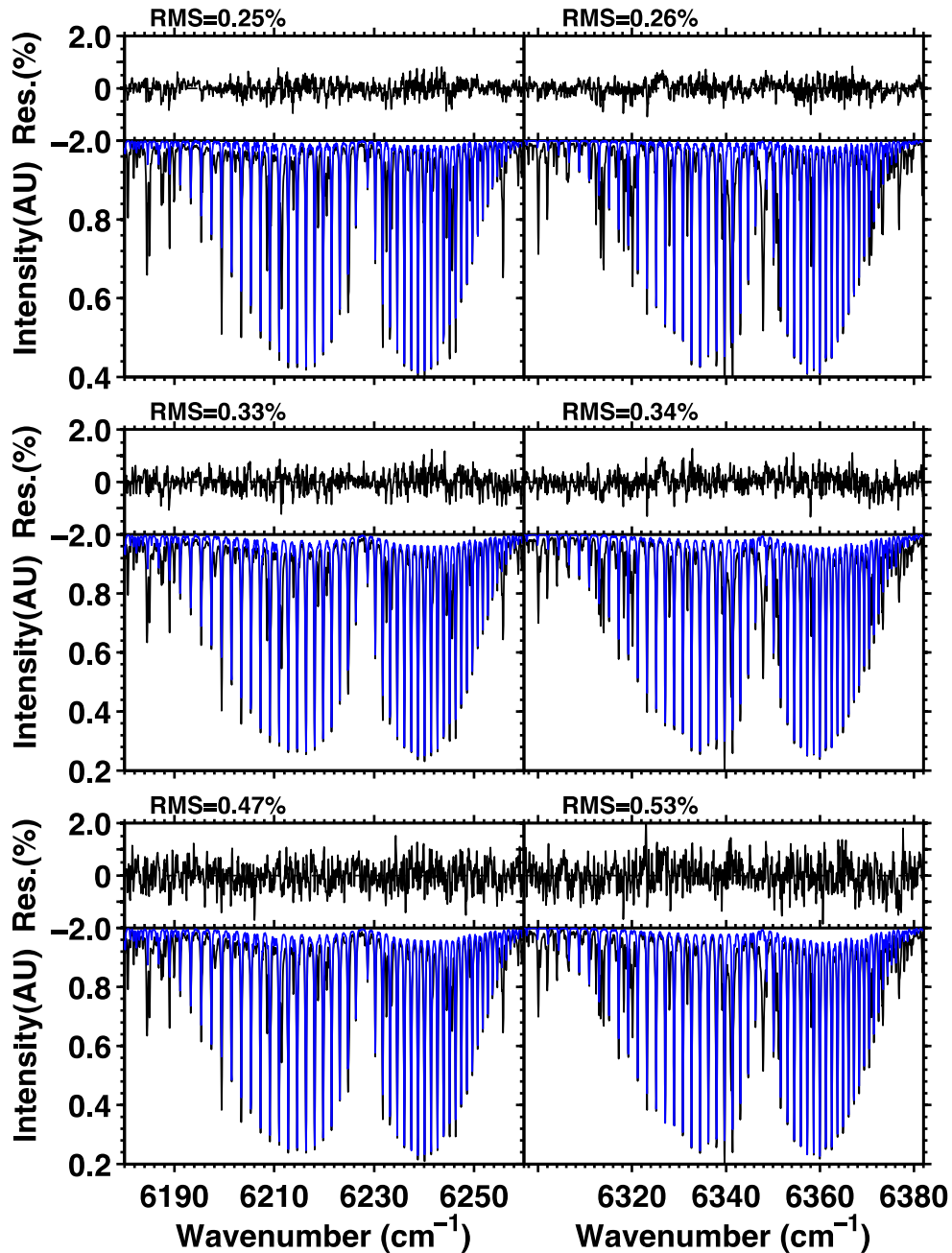


Figure 4.2 Sample spectral fittings of CO₂ bands near 1.6 μm region using the CLARS-FTS measurements in the Spectralon® viewing geometry (top panels); pointing at the Santa Anita Race Track, Arcadia (middle panels); or pointing at the west Pasadena (bottom panels). The measurements were taken on January 3rd, 2013 with a Solar Zenith Angle (SZA) of 58.62° (top panels), 58.39° (middle panels), and 57.89° (bottom panels) respectively. Each spectrum is from 12 co-added scans, which were taken consecutively over 3 minutes. The spectral SNR are 532:1, 417:1, and 227:1 from top to bottom panels, respectively. The measured radiances subtracting the simulated spectra, which included contributions of all trace gases and solar lines, yield the spectral fitting residuals. In all panels, black curves are measured spectra and blue curves are the estimated contribution of CO₂ absorption from the spectral fittings. Contributions of other species in these spectral regions are not shown.

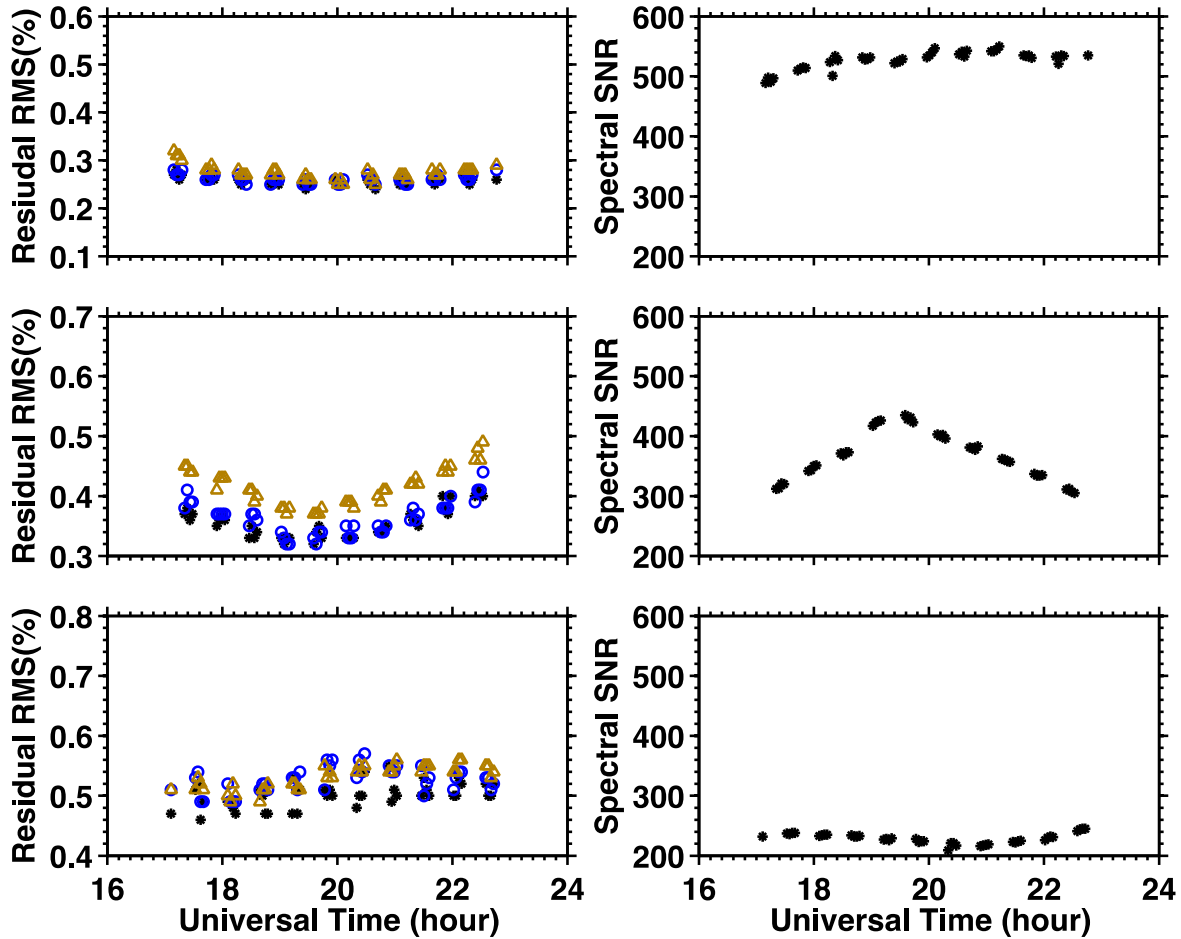


Figure 4.3 Root Mean Square (RMS) of spectral fitting residuals (Left panels) and spectral SNR (Right panels) as a function of time for the measurements of CO₂ and O₂ column densities in Spectralon® viewing geometry (top panels); over the Arcadia Race Track (middle panels); over west Pasadena (bottom panels). Three spectral bands centered at 6220 cm⁻¹ (black stars, noted as MW6220 thereafter), 6339 cm⁻¹ (blue circles, noted as MW6339 thereafter) and 7885 cm⁻¹ (gold triangles, noted as MW7885 thereafter) are presented, respectively. The spectral SNR were nearly identical over the three spectral bands in a measured spectrum, but varies among spectra. The measurements were performed on January 3rd, 2013. The spectral fitting residuals were normalized by the spectral continuum levels prior to the computation of RMS values. The spectral fitting residuals were dominated by the photon shot noise. The Chi-squared tests of spectral fitting residuals yielded values generally within 1.3.

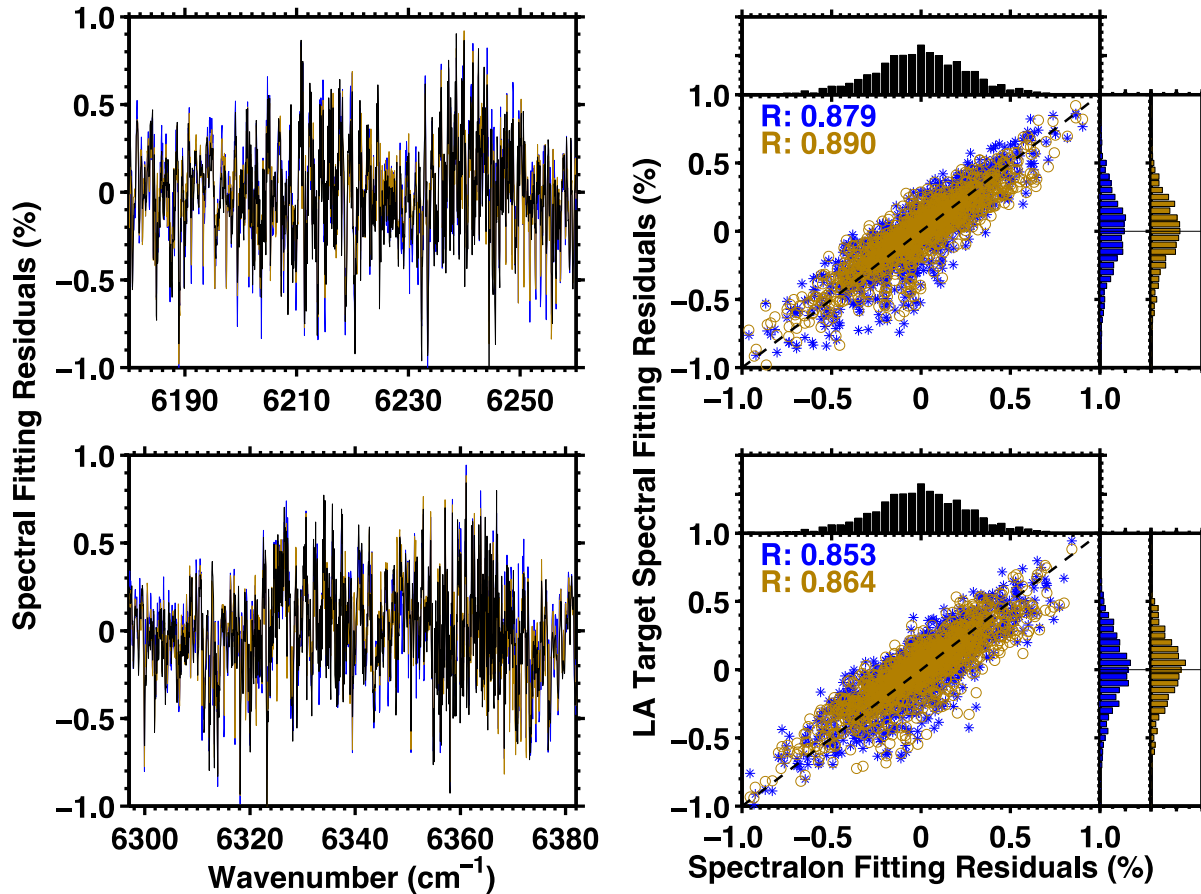


Figure 4.4: The spectral fitting residuals (left panels) and their correlation, Pearson correlation coefficients (R), and histograms (right panels) with MW6220 (top panels) and MW6339 (bottom panels) for CO₂ slant column density measurements. In left panels, black curve is for Spectralon® viewing geometry; blue curve is for west Pasadena; gold curve is for Arcadia Race Track. In right panels, blue stars are the correlation between Spectralon® and west Pasadena; gold circles are the correlation between Spectralon® and Arcadia Race Track; the black dash lines indicate the one to one correlation. The spectral fitting residuals were generated using the co-addition of residuals of 41 spectral fittings of Spectralon® target, 41 spectral fittings of west Pasadena target, and 40 spectral fits of Arcadia Race Track target on January 3rd, 2013. The systematic residuals arise from the imperfect line shape function and spectroscopic parameters in addition to uncertainties of atmospheric pressure and temperature parameters since the magnitude and positions of spiky fitting residuals consistently appear in all three target scenes. However, the magnitude of most of systematic fitting residuals is within 0.5% of spectral continuum levels.

4.2.3. Column Average Volume Mixing Ratio of GHG in Dry Air (XGHG)

XGHG may be calculated from the retrieved GHG column, according to

$$\text{XGHG} = \frac{\text{GHG column}}{\text{dry air total column}} \quad (4.1)$$

where,

$$\text{dry air total column} = \frac{\text{O}_2 \text{ column}}{0.2095} \quad (4.2)$$

Using this expression to compute the column average GHG, VMR will improve the measurement precision of atmospheric GHG concentrations (Washenfelder, 2006; Fu et al., 2008) if systematic errors in the column abundances are common to both the GHG and O₂. These could arise from errors in the spectra, such as instrumental line shape, detector nonlinearity, or from errors in the calculated slant path due to uncertainty in the surface pressure, solar zenith angle (SZA), pointing or aerosol scattering. Errors due to non-ideal ILS are expected to be small because proper FTS alignment was verified by several methods as discussed in section 4.2.4. Detector nonlinearity may be significant when viewing very bright sources such as the Sun; this effect is negligible for reflected sunlight measurements such as those employed by CLARS-FTS. However, errors in the calculated slant path (due to errors in surface pressure, SZA or neglect of aerosol scattering), water vapor (for determination of dry air column mixing ratios), spectral zero level offsets and solar intensity variations due to thin clouds will cause uncertainties in the retrieved column densities of target gases and O₂. Most of these errors are mitigated in the measurement approach and retrieval algorithms. The effect of aerosol scattering on individual retrievals is assessed by comparing the measured O₂ column abundance with the value derived from the surface pressure at the target. Differences exceeding a threshold value trigger the setting of a data quality flag which is used in subsequent data filtering steps. The remaining impacts are estimated in Section 4.2.5.

4.2.4. Sample Retrievals from CLARS-FTS

As an illustration of the data from the CLARS-FTS, sample results from several days of measurements will be shown in this section; more detailed analyses of the data will be presented in subsequent papers. Figure 4.5 shows the XCO₂ and the differences of XCO₂ between MW6220 and MW6339 as a function of time using the CLARS-FTS measurement over three targets on January 3rd, 2013. The difference in XCO₂ between MW6220 and MW6339 using the Spectralon® target (41 measurements) is 0.44 ± 0.53 ppm (1 σ). For the measurements over Santa Anita Park and west Pasadena, the XCO₂ values using MW6220 are also higher than those of MW6339. A difference between the two microwindow retrievals is a consistent feature of the data. CLARS-FTS, which are based on the HITRAN 2008 line list, show improvements in the band-to-band consistency of XCO₂ compared to those which use the HITRAN 2004 line list. These systematic differences of retrieved XCO₂ values between two spectral bands likely arise from systematic errors in spectroscopic parameters between the two bands and the number and intensity of spectral features from interfering species.

As discussed above, SVO measurements are representative of the unpolluted free troposphere while LABS measurements carry the spatial and temporal signatures of boundary layer emissions.

Two spectral regions, which are centered at 5938 cm^{-1} (noted as MW5938 thereafter) and 6076 cm^{-1} (noted as MW6076 thereafter), were utilized in measuring CH_4 column abundances. Figure 4.6 presents sample spectral fits of CH_4 measurements. The overall spectral fitting of CH_4 shows qualities similar to that of CO_2 bands in terms of the RMS of spectral fitting residuals (Figure 4.7) and the magnitude of systematic fitting residuals (Figure 4.8). XCH_4 using the MW6076 is generally higher than that of using MW5938. XCH_4 over Santa Anita Park and west Pasadena show enhanced values compared to the Spectralon® levels (Figure 4.9). Similar enhancements and diurnal variability of XCH_4 were observed on other days.

The observations of XCO utilized the measured spectral region near $2.36\text{ }\mu\text{m}$. The enhancement and stronger diurnal variability of XCO were seen in measurements over both Santa Anita Park and west Pasadena targets, compared to the Spectralon® values (Figure 4.10). Measurement of XCO presents an extra challenge due to the weakness of the CO spectral features, the low solar radiance in this region and the overlap with interfering spectral lines from CH_4 and water vapor. The broad and strong absorption features of interfering species in CO spectral region led to that the spectral fitting residuals for the CO bands are about a factor of two higher than that near $1.6\text{ }\mu\text{m}$. And the weak CO absorption features result in lower sensitivities near surface compared to the measurements of CO_2 , CH_4 , and O_2 . Despite these problems, as shown in Figure 4.10, the XCO measurements provide reliable data for both LA basin targets and Spectralon®.

The sensitivities of CLARS-FTS measurement are characterized by their column averaging kernels. Figure 4.11 shows the column averaging kernels for CO_2 , CH_4 , CO, and O_2 for the Spectralon® (top panels) and Santa Anita Park (bottom panels) targets.

4.2.5. Measurement Uncertainty of XGHG

The uncertainties in retrieved values of column-averaged VMR for both LA basin and Spectralon® measurements contain random and systematic components. The random component determines the measurement precision for XGHG retrievals. The systematic component controls the overall measurement accuracy.

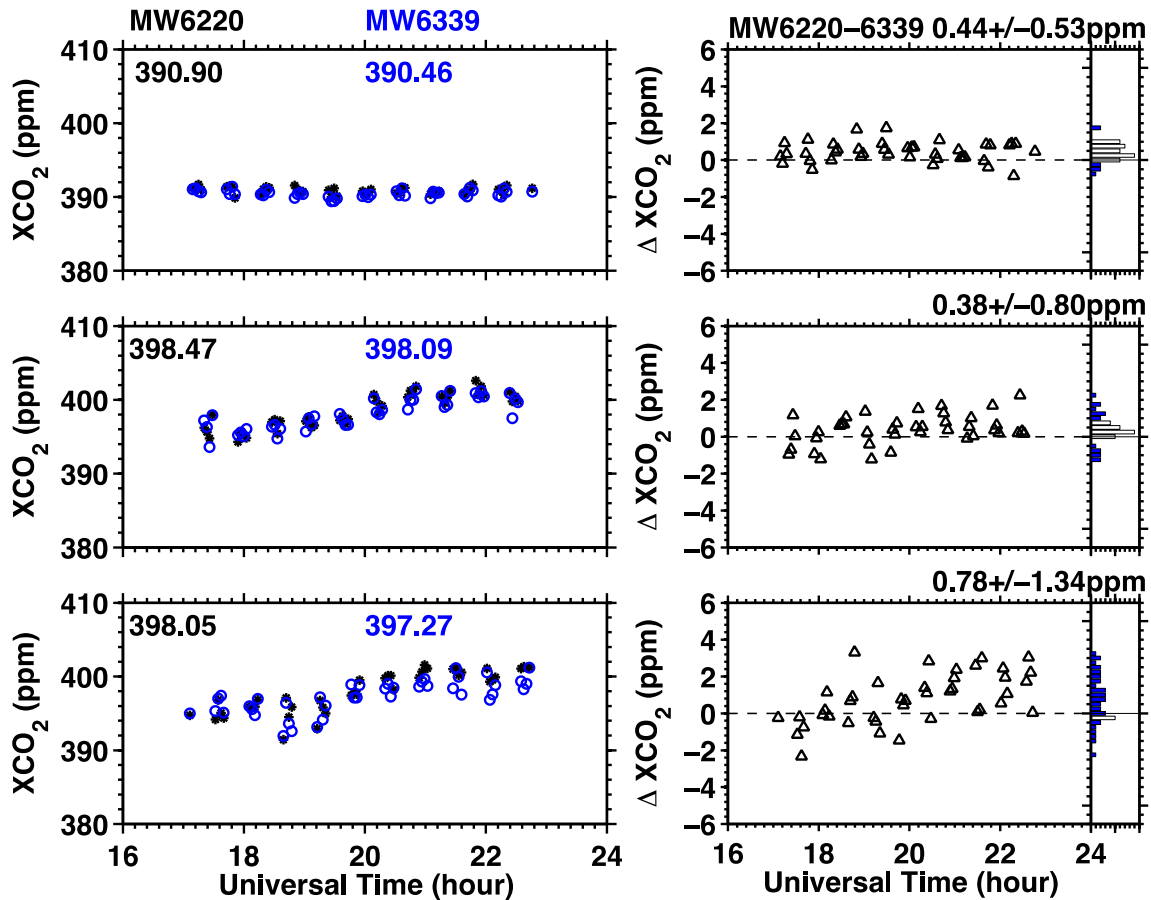


Figure 4.5: XCO₂ (in parts per million (ppm)) measured by CLARS-FTS with MW6220 (black dots) and MW6339 (blue circles) on January 3rd, 2013 (left panels) and differences of retrieved XCO₂ between the two spectral regions and the histograms (right panels) in the Spectralon® viewing geometry (top panels), towards the Arcadia Race Track (middle panels); and towards west Pasadena (bottom panels). Black stars in left panels: XCO₂ obtained using the spectral region of MW6220. Compared to the background levels of XCO₂ (top panels), XCO₂ over Arcadia Race Track (middle panels) and west Pasadena (bottom panels) show higher values (mean ART-SV: 7.60 ppm; mean WP-SV: 6.98 ppm) and present stronger diurnal cycles than those measurements over CLARS site. The XCO₂ values retrieved from MW6220 are higher than those of MW6339. The mean differences between MW6220 and MW6339 are 0.44 ppm, 0.38 ppm, 0.78 ppm for DSV, ART and WP respectively. It was also appeared in the spectral analyses of the TCCON measurements (~0.15 ppm). Both CLARS-FTS and TCCON results, which are using HITRAN 2008 line list, show improvements on the band-to-band consistency of XCO₂, compared to those of using HITRAN 2004 line list such as Figure 6 of Washenfelder et al. (2006) with the XCO₂ using MW6220 about 0.9 ppm higher than that of MW6339. These systematic differences of retrieved XCO₂ values between two spectral bands likely arise from the discrepancies of spectroscopic parameters between two spectral bands and the amount/intensity of spectral features of interfering species.

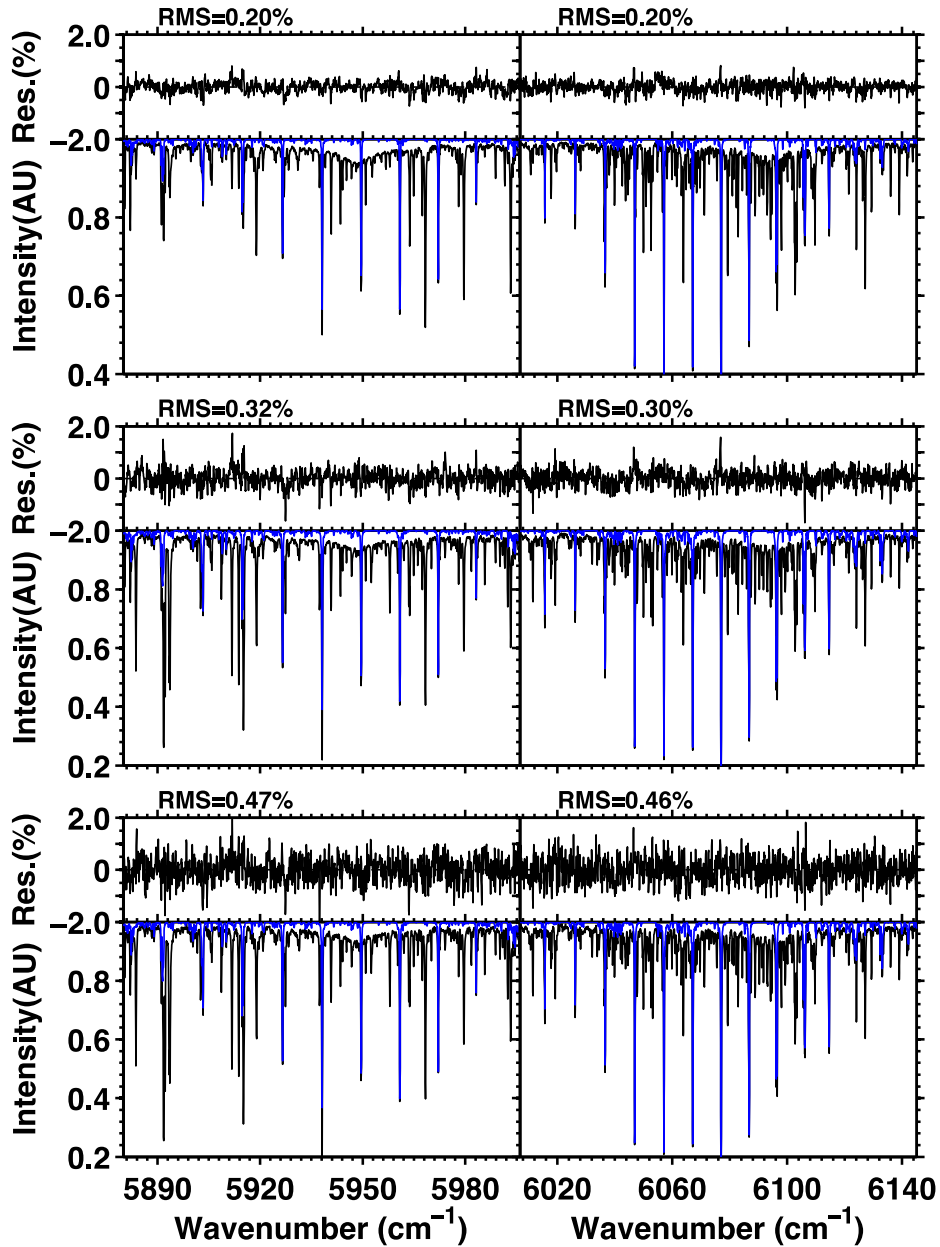


Figure 4.6: Sample spectral fittings of CH_4 bands, which are centered at 5938 cm^{-1} (noted as MW5938 thereafter) and 6076 cm^{-1} (noted as MW6076 thereafter) using the CLARS-FTS measurements in the Spectralon® viewing geometry (Top panels); pointing at the Santa Anita Race Track, Arcadia (middle panels); or pointing at the west Pasadena (Bottom panels). The measurements were taken on January 3rd, 2013 with a Solar Zenith Angle (SZA) of 58.62° (top panels), 58.39° (middle panels), and 57.89° (bottom panels) respectively. Each spectrum is from 12 co-added scans, which were taken consecutively over 3 minutes. The spectral SNR are 532:1, 417:1, and 227:1 from top to bottom panels, respectively. The measured radiances subtracting the simulated spectra, which included contributions of all trace gases and solar lines, yield the spectral fitting residuals. In all panels, black curves are measured spectra and blue curves are the estimated contribution of CH_4 absorption from the spectral fittings. Contributions of other species in these spectral regions are not shown.

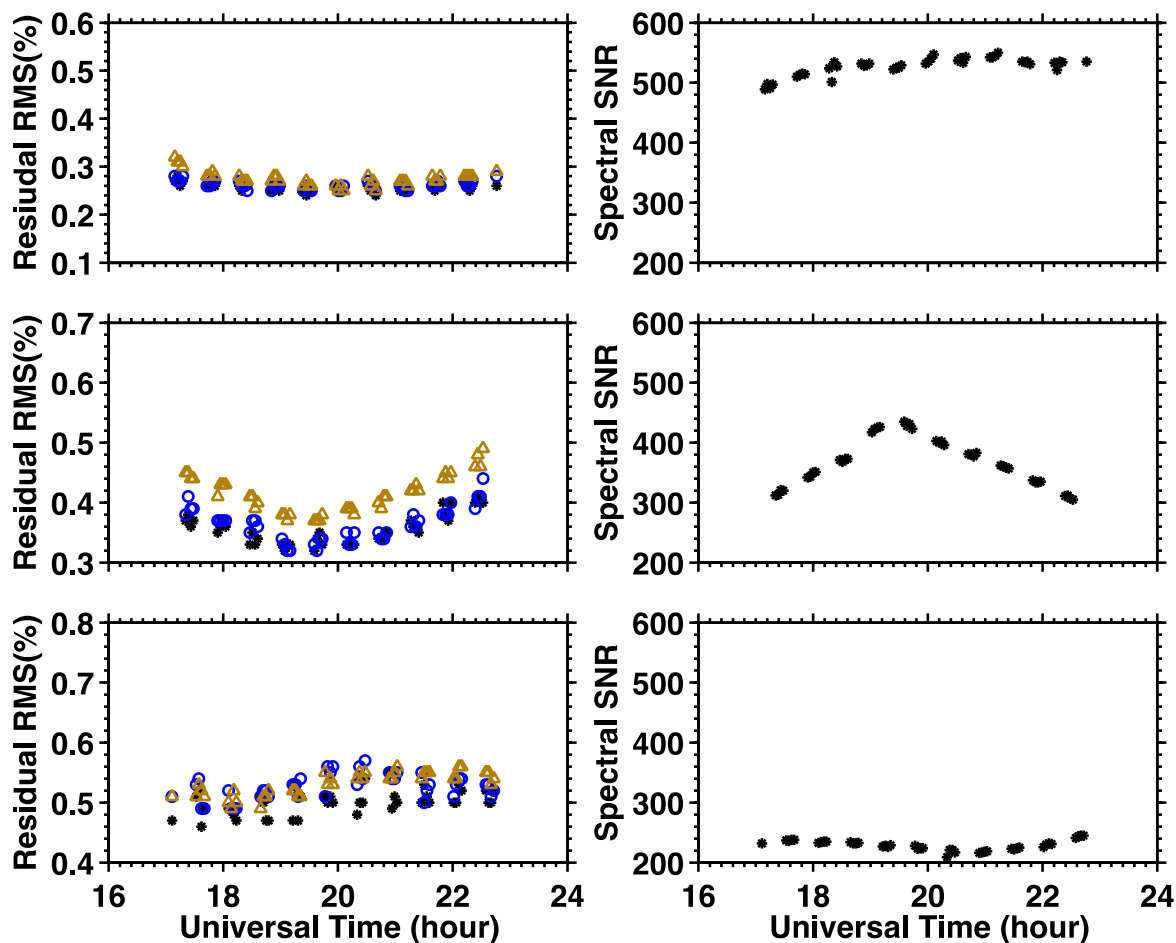


Figure 4.7: Root Mean Square (RMS) of spectral fitting residuals (left panels) and spectral SNR (right panels) as a function of time for the measurements of CH₄ and O₂ column densities in Spectralon® viewing geometry (top panels); over the Arcadia Race Track (middle panels); over west Pasadena (bottom panels). Three spectral bands centered at 5938 cm⁻¹ (black stars, noted as MW5938 thereafter), 6076 cm⁻¹ (blue circles, noted as MW6076 thereafter) and 7885 cm⁻¹ (gold triangles, noted as MW7885 thereafter) are presented, respectively. The spectral SNR were nearly identical over the three spectral bands in a measured spectrum, but varies among spectra. The measurements were performed on January 3rd, 2013. The spectral fitting residuals were normalized by the spectral continuum levels prior to the computation of RMS values. The spectral fitting residuals were dominated by the photon shot noise. The Chi-squared tests of spectral fitting residuals yielded values generally within 1.3.

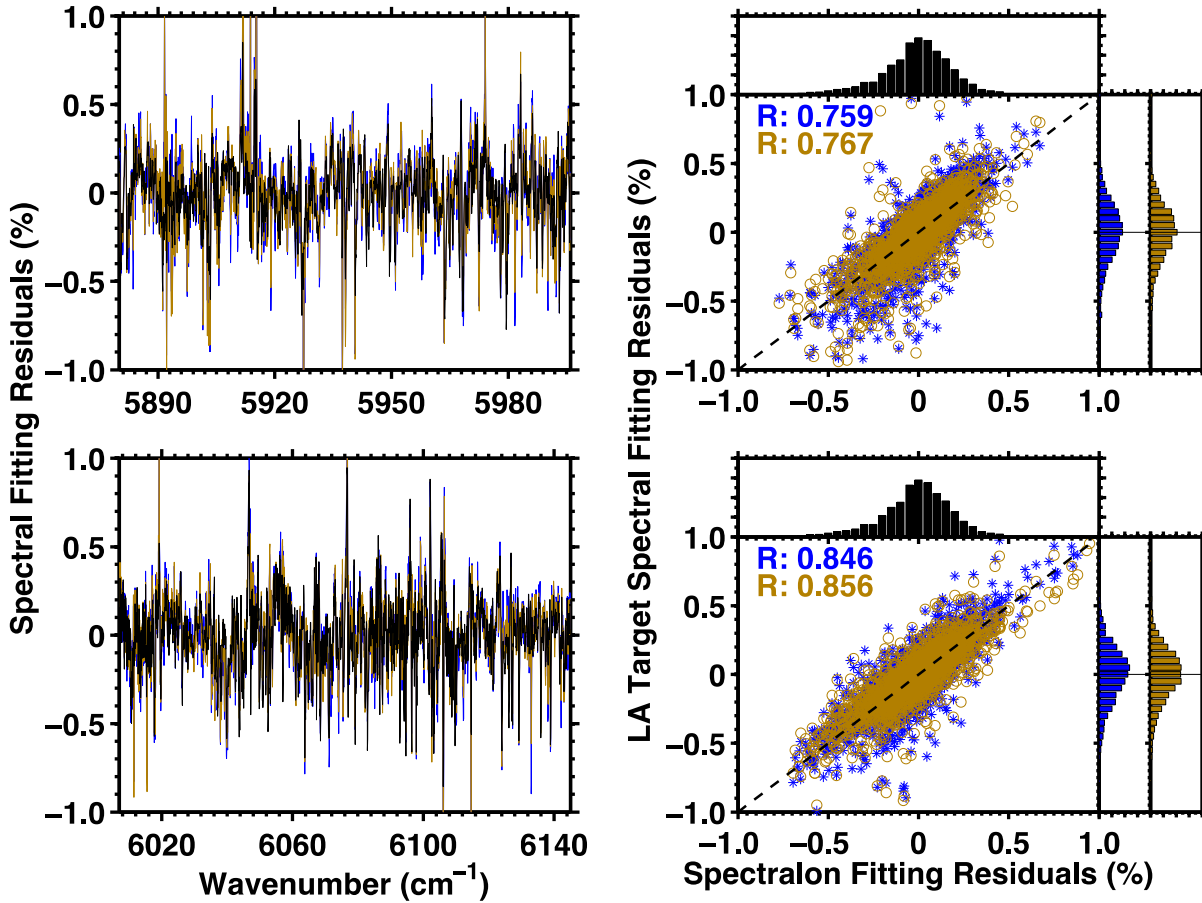


Figure 4.8: The spectral fitting residuals (left panels) and their correlation, Pearson correlation coefficients (R), and histograms (Right panels) with MW5938 (Top panels) and MW6076 (bottom panels) for CH₄ slant column density measurements. In left panels, black curve is for Spectralon® viewing geometry; blue curve is for west Pasadena; gold curve is for Arcadia Race Track. In right panels, blue stars are the correlation between Spectralon® and west Pasadena; gold circles are the correlation between Spectralon® and Arcadia Race Track; the black dash lines indicate the one to one correlation. The spectral fitting residuals were generated using the co-addition of residuals of 41 spectral fittings of Spectralon® target, 41 spectral fittings of west Pasadena target, and 40 spectral fits of Arcadia Race Track target on January 3rd, 2013. The systematic residuals arise from the imperfect line shape function and spectroscopic parameters in addition to uncertainties in atmospheric pressure and temperature parameters since the magnitude and positions of spiky fitting residuals consistently appear in all three target scenes. However, the magnitude of most of systematic fitting residuals is within 0.5% of spectral continuum levels.

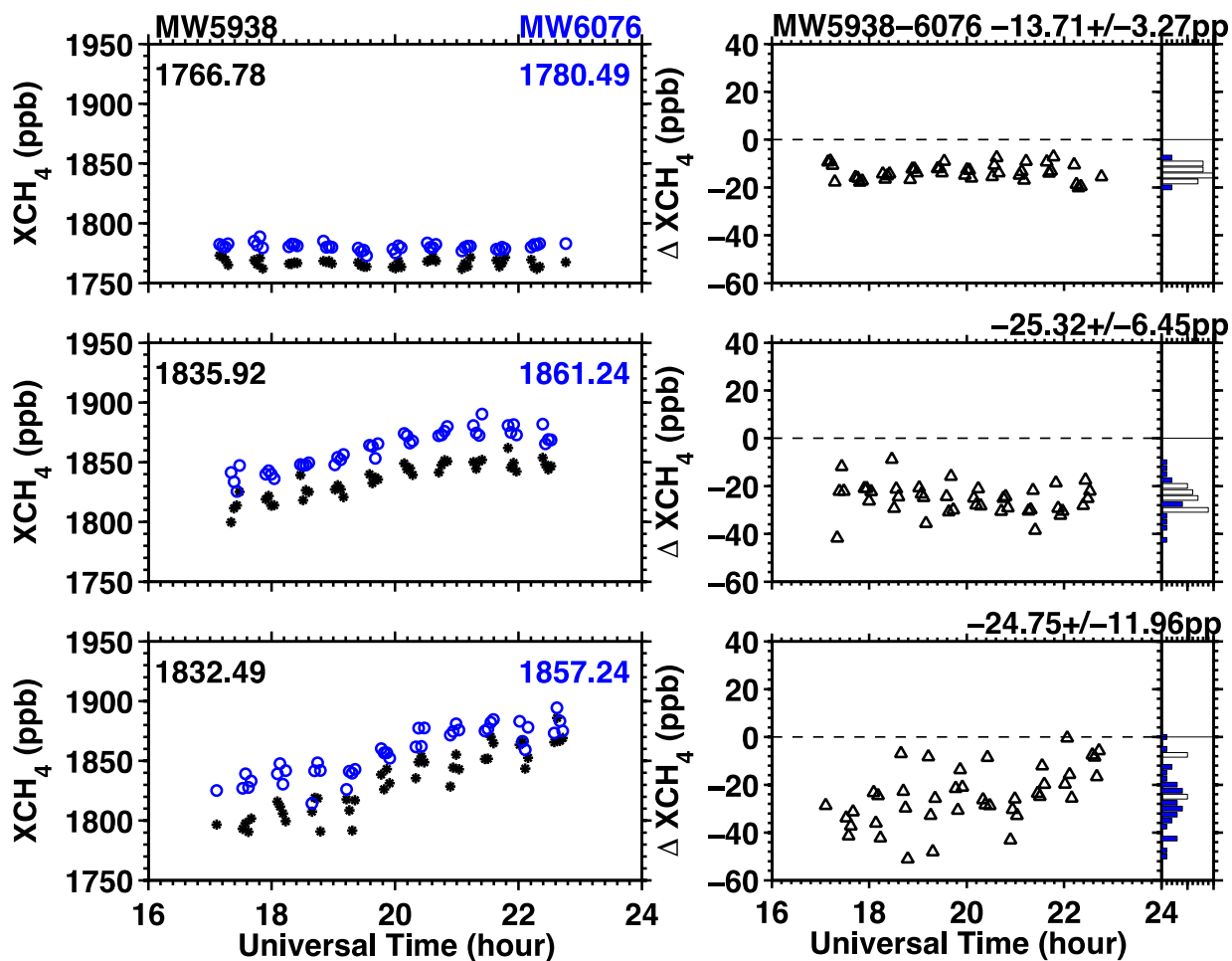


Figure 4.9: XCH₄ (in parts per billion (ppb)) measured by CLARS-FTS with MW5938 (black dots) and MW6076 (blue circles) on January 3rd, 2013 (left panels) and differences of retrieved XCH₄ between the two spectral regions and the histograms (right panels) in the Spectralon® viewing geometry (top panels), towards the Arcadia Race Track (middle panels); and towards west Pasadena (bottom panels). Black stars in left panels: XCH₄ obtained using the spectral region of MW5938. Compared to the background levels of XCH₄ (top panels), XCH₄ over Arcadia Race Track (middle panels) and west Pasadena (bottom panels) show higher values (mean ART-SV: 74.95 ppb; mean WP-SV: 71.23 ppb) and present stronger diurnal cycles than those measurements over CLARS site. The XCH₄ values retrieved from MW6076 are higher than those of MW5938. The mean differences between MW6076 and MW5938 are 13.71 ppb, 25.32 ppb, and 24.75 ppb for SV, ART and WP respectively. These systematic differences of retrieved XCH₄ values between two spectral bands likely arise from the discrepancies of spectroscopic parameters between two spectral bands and the amount/intensity of spectral features of interfering species.

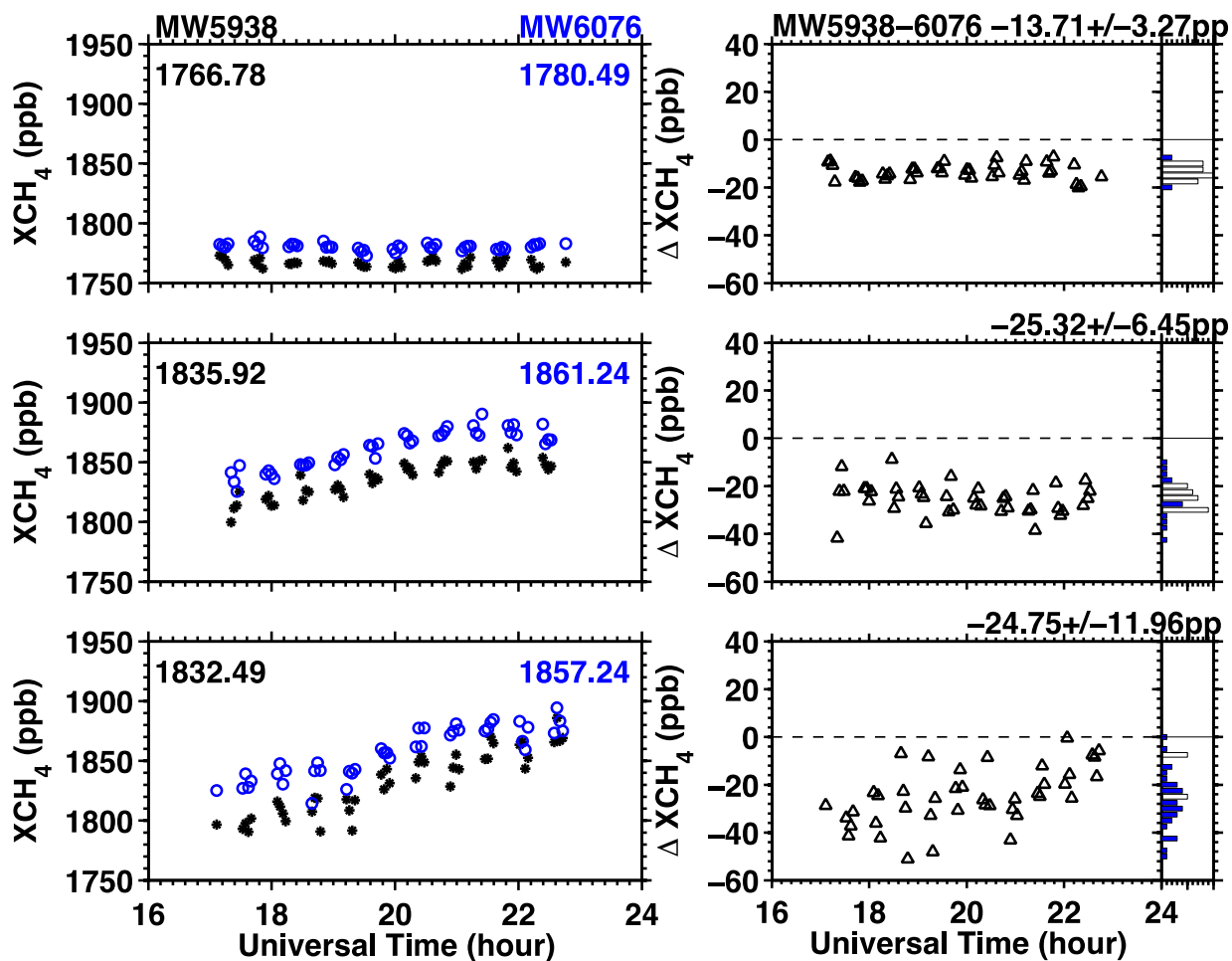


Figure 4.10: XCH₄ (in parts per billion (ppb)) measured by CLARS-FTS with MW5938 (black dots) and MW6076 (blue circles) on January 3rd, 2013 (left panels) and differences of retrieved XCH₄ between the two spectral regions and the histograms (right panels) in the Spectralon® viewing geometry (top panels), towards the Arcadia Race Track (middle panels); and towards west Pasadena (bottom panels). Black stars in left panels: XCH₄ obtained using the spectral region of MW5938. Compared to the background levels of XCH₄ (top panels), XCH₄ over Arcadia Race Track (middle panels) and west Pasadena (bottom panels) show higher values (mean ART-SV: 74.95 ppb; mean WP-SV: 71.23 ppb) and present stronger diurnal cycles than those measurements over CLARS site. The XCH₄ values retrieved from MW6076 are higher than those of MW5938. The mean differences between MW6076 and MW5938 are 13.71 ppb, 25.32 ppb, and 24.75 ppb for SV, ART and WP respectively. These systematic differences of retrieved XCH₄ values between two spectral bands likely arise from the discrepancies of spectroscopic parameters between two spectral bands and the amount/intensity of spectral features of interfering species.

4.2.6. Estimation of XGHG Measurement Precision

The uncertainties returned by GFIT assume a Gaussian distribution of residuals from the spectral fits. In reality, this is usually not the case due to systematic artifacts (e.g., errors/omissions in the spectroscopic data base, the modeling of the instrument response, and uncertainty in the pointing accuracy resulting in errors in the computed optical path). These can dominate the spectral fitting residuals produced by GFIT. Since these artifacts are generally the same from spectrum to spectrum, an uncertainty calculated from the RMS spectral fit generally underestimates the true precision. Hence, we utilize the differences of XGHG between two spectral regions to estimate the precisions of CLARS-FTS measurements. These differences include a systematic bias coming from variations in the spectral signatures of interfering species, and the inconsistencies between spectroscopic parameters within these spectral regions. The remaining variation (1- σ standard deviation of the mean differences) is given by the expression,

$$\sigma_{\Delta\text{XGHG}} = \sqrt{err_{\text{MW1}}^2 + err_{\text{MW2}}^2 + 2err_{\text{MW1}}err_{\text{MW2}}} \quad (4.3)$$

where, $\sigma_{\Delta\text{XGHG}}$ is 1 σ standard deviation of the mean differences using two spectral regions, err_{MW1} and err_{MW2} are the measurement uncertainties/precisions of two spectral regions. The spectral noise and the number of spectral points are the dominant factors of measurement precisions. These two factors are nearly identical between MW1 and MW2 since their small separations ($\sim 5 - 100 \text{ cm}^{-1}$) on the measured spectra and their nearly identical widths of spectral fitting windows (Table 4.2). The spectral noises are random, i.e., no correlation on the spectral noise between two adjacent spectral bands. Hence, the cross term in the right hand side of Equation 4.3 vanishes and Equation 4.3 can be written as

$$err_{\text{MW1}} = err_{\text{MW2}} = \sigma_{\Delta\text{XGHG}} / \sqrt{2} \quad (4.4)$$

Table 4.3 lists the estimated measurement precisions of XCO₂, XCH₄, and XCO over CLARS site, Santa Anita Park and west Pasadena targets by applying Equation 4.4 to the XGHG differences using two adjacent spectral regions. The measurements of Spectralon® targets on January 3rd, 2013 show higher precision (XCO₂: 0.09%; XCH₄: 0.13%; XCO: 2.00%) than the measurements over Santa Anita Park (XCO₂: 0.14%; XCH₄: 0.25%; XCO: 4.01%) and west Pasadena targets (XCO₂: 0.24%; XCH₄: 0.46%; XCO: 8.01%). The measurement precision on January 18th, 2013 shows characteristics similar to those on January 3rd, 2013. The low precision of XCO arises from the decreased spectral SNR in the spectral regions used in the measurements of CO slant column densities. The measurement precision shows target site dependence due to the differences of spectral SNR over three target sites. Overall, the high precision of CLARS-FTS measurements is sufficient to capture the diurnal variations of XCO₂, XCH₄ and XCO and the differences among different targets over LA basin.

Table 4.2: Spectral range, species that have spectral signatures within the spectral range, and sources of spectroscopic parameters used in spectral fittings.

Spectral Range cm ⁻¹	(source of spectroscopic line parameters*) Gases to Fit	Auxiliary Parameters to fit
6180.0 – 6260.0	(1)CO ₂ , (2)H ₂ O, (2)HDO, (3,4)CH ₄	cl ^a ct ^b fs ^c
6297.0 – 6382.0	(1)CO ₂ , (2)H ₂ O, (2)HDO	cl ct fs
4810.0 – 4890.0	(1)CO ₂ , (5)N ₂ O, (2)H ₂ O, (2)HDO, (6)CH ₄ , (7)CO	cl ct fs
5880.0 – 5996.0	(3,4)CH ₄ , (1)CO ₂ , (2)H ₂ O, (2)HDO	DLPBF ^d
6007.0 – 6145.0	(3,4)CH ₄ , (1)CO ₂ , (2)H ₂ O, (2)HDO	DLPBF
4208.7 – 4257.3	(7)CO, (6)CH ₄ , (2)H ₂ O, (2)HDO	cl ct fs
4262.0 – 4318.8	(7)CO, (6)CH ₄ , (2)H ₂ O, (2)HDO	DLPBF
7765.0 – 8005.0	(8)O ₂ , (9)OO ₂ , (2)H ₂ O	cl ct fs

^a continuum level

^b continuum tilt

^c frequency shift

^d fitting the continuum level using Discrete Legendre Polynomial Basis Functions (DLPBF)

* All of the spectroscopic parameters are available in HITRAN 2008 compilation prepared by Rothman et al. (2009).

(1) Toth et al. (2008)

(2) Toth (2005) with the addition (in 2005-7) of hundreds of weak H₂O lines that are visible in humid, high-airmass TCCON spectra. Jenouvrier et al. (2007) subsequently identified many of these weak lines.

(3) GFIT (February 2013 version) includes the weak CH₄ lines extending from 6180 to 6220 cm⁻¹ which were provided by Dr. Linda Brown

(4) Frankenberg et al. (2008)

(5) Toth (1999, 2000)

(6) Brown et al. (2003)

(7) Brault et al. (2003)

(8) Line list created by Andrew Orr-Ewing using the PGOPHER code, based on lab measurements of Newman et al. (1999). The widths were subsequently modified to be 1.5% larger than those in Yang et al. (2005) in order to minimize the airmass dependence of retrieved O₂ column density, as described by Washenfelder et al. (2006). O₂ quadrupoles lines are from Gordon et al. (2010).

(9) The collision induced absorption (CIA) is represented by a pseudo-linelist based on fits to lab spectra described by Smith and Newnham (2000). The CIA is not used in the determination of the O₂ column. It is fitted only to minimize its impact on the discrete O₂ lines.

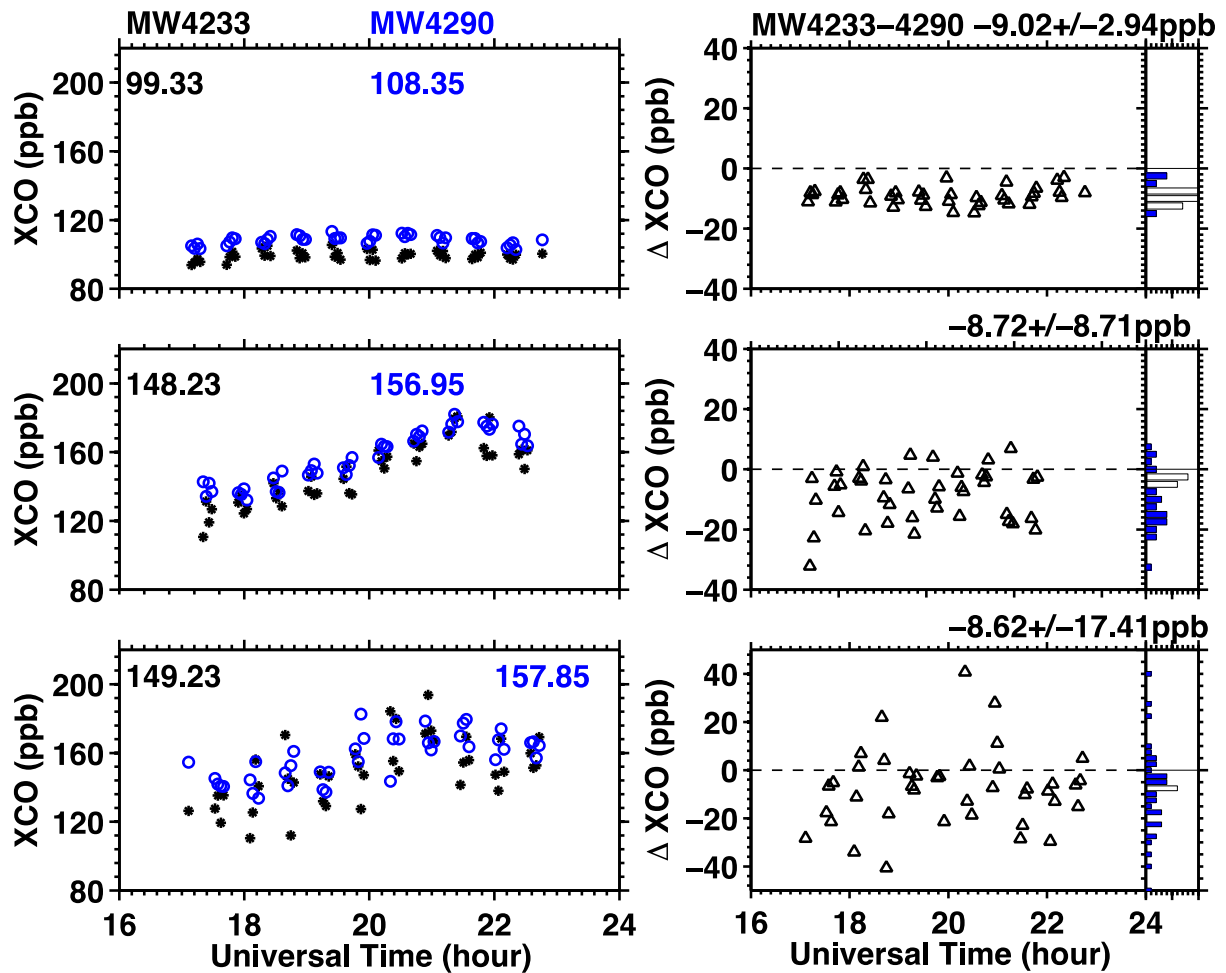


Figure 4.11: XCO (in parts per billion (ppb)) measured by CLARS-FTS with MW4233 (black dots) and MW4290 (blue circles) on January 3rd, 2013 (left panels) and differences of retrieved XCO between the two spectral regions and the histograms (right panels) in the Spectralon® viewing geometry (top panels), towards the Arcadia Race Track (middle panels); and towards west Pasadena (bottom panels). Compared to the background levels of XCO (top panels), XCO over Arcadia Race Track (middle panels) and west Pasadena (bottom panels) show higher values (mean ART-DSV: 48.75 ppb; mean WP-DSV: 49.70 ppb) and present stronger diurnal cycles than those measurements over CLARS site. The XCO values retrieved from MW4290 are higher than those of MW4233. The mean differences between MW4290 and MW4233 are 9.02 ppb, 8.72 ppb, 8.62 ppb for DSV, ART and WP respectively. These systematic differences of retrieved XCO values between two spectral bands are likely arisen from the discrepancies of spectroscopic parameters between two spectral bands and the amount/intensity of spectral features of interfering species.

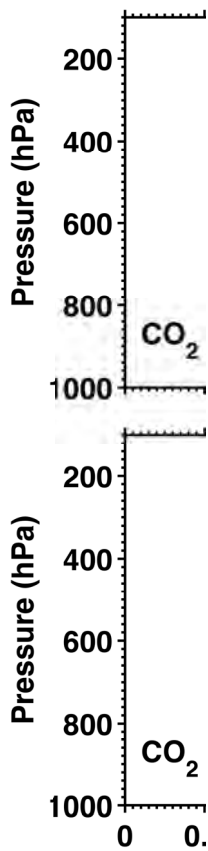


Figure 4.12: Column averaging kernels of GHG measurements using CLARS-FTS with a Maximum Optical Path Difference (MOPD) of 5 cm. Top panels: for the measurements over CLARS site in the Spectralon® viewing geometry; bottom panels: for the measurements targeting the land surface of Arcadia race track (34.141°N, 118.042°W, 155 meters above sea level, 9.3 kilometers slant distance to CLARS site), Arcadia, California. .

Table 4.3: Estimated Measurement Precisions¹

	January 3 rd , 2012			January 18 th , 2012		
XCO ₂	0.37, 0.57, 0.95 ppm ²	0.09, 0.14, 0.24% ³		0.31, 0.66, 0.76 ppm ²	0.08, 0.17, 0.19% ³	
XCH ₄	2.31, 4.56, 8.46 ppb	0.13, 0.25, 0.46%		2.77, 4.90, 9.11 ppb	0.15, 0.26, 0.49%	
XCO	2.08, 6.16, 12.31 ppb	2.00, 4.01, 8.01%		1.85, 5.51, 10.65 ppb	1.88, 4.19, 8.06%	

¹ The method of measurement precision estimation is introduced in Section 4.5.1

² Data in this column are the estimated measurement precisions of XGHG over Spectralon®, Santa Anita Park and west Pasadena targets respectively. Unit is in parts of million (ppm) for XCO₂ and in parts of billion (ppb) for XCH₄ and XCO.

³ Data in this column are the percentage measurement precisions, which were estimated with respect to the mean XGHG over Spectralon®, Santa Anita Park and west Pasadena targets respectively.

4.2.7. Estimation of XGHG Measurement Accuracy

Systematic error sources include the uncertainties in spectroscopic line parameters, light path calculation uncertainties, and errors in the ILS, which affects the accuracy of CLARS-FTS measurements. Table 4.4 lists the estimated measurement accuracy. The uncertainties of measured XCO₂, XCH₄ and XCO arise from spectroscopic parameters, which are expected to be similar to those from previous studies (Washenfelder et al., 2006; Wunch et al., 2010, 2011). Regular HCl cell and infrared laser measurements are carried out to assess the alignment stability and performance of the FTS. The uncertainties in the light path computation arise from residual pointing errors and from the neglect of aerosol scattering in the radiative transfer calculations. As discussed previously, aerosol interference is reduced by using the simultaneously measured O₂ slant column density, which is proportional to the optical path length, to compute XGHG.

Table 4.4: Estimated Measurement Accuracy¹

Error Sources	XCO ₂	XCH ₄	XCO
Spectroscopic Line Parameters, Pressure, Temperature Profiles ²	~ 1.1%	~ 4.0%	~ 2.0 %
Light path calculation ³	< 1.0%	< 1.0%	< 1.0 %
Instrument line shape ⁴	< 1.0%	< 1.0%	< 1.0%
Uncertainty Priori to Calibration	< 3.1 %	< 6.0 %	< 4.0 %

¹ The uncertainty was estimated prior to the CLARS-FTS calibration/validation activity. The discussion of measurement accuracy estimation is introduced in Section 4.5.2.

² Estimation were made based on the uncertainty of TCCON measurements prior to applying calibration factors [Wunch et al., 2010; 2011].

³ Refer to the measured XGHG uncertainty arise from the remaining impacts of aerosol that were not removed by the approach of computing XGHG in section 4.3.

⁴ Refer to the differences between measured and theoretical line shape functions in section 2.2.4

4.3. Diurnal Variations of XGHG

Figure 4.12 shows the diurnal variations of XCO₂, XCH₄ and XCO for the SVO measurements, and the Los Angeles basin, West Pasadena and Santa Anita measurements from around 8:30 to 16:30 local time on seven continuous days during the period of May 5 to May 11, 2012. From May 5 to May 9, the FTS was operated in the target mode, taking alternate measurements among West Pasadena, Santa Anita and SVO. On May 10 and 11, standard measurement cycle was performed.

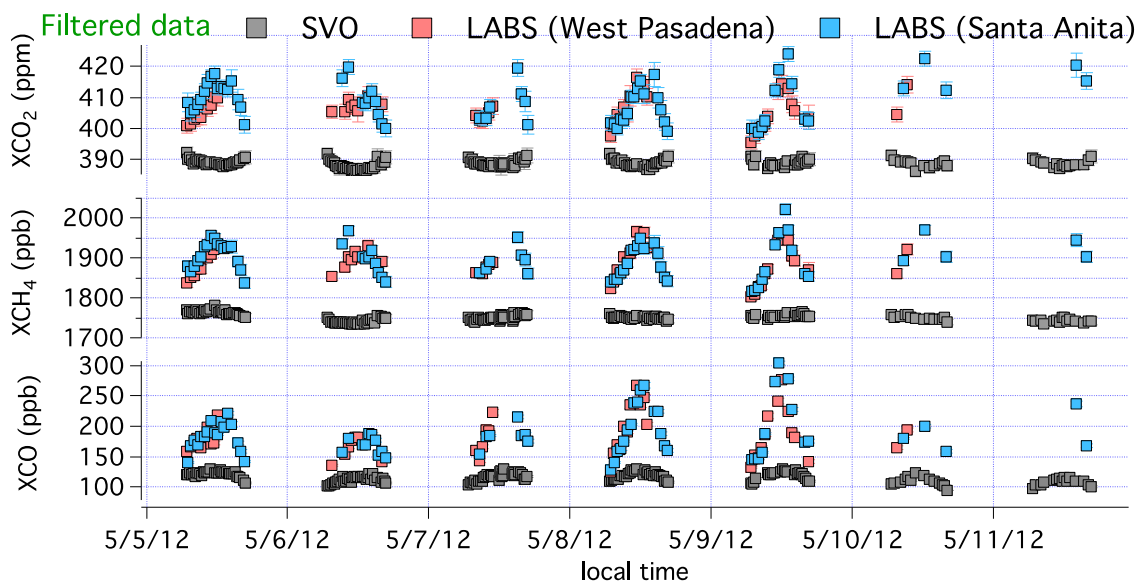


Figure 4.13: Diurnal variations of SVO (grey) and LABS, west Pasadena (red) and Santa Anita Park (blue), XCO_2 , XCH_4 and XCO from around 8:30 to 16:30 on seven consecutive days in May 2012. Error bars represent the RMS of the retrieval spectral fitting residual. Bad data points, such as data taken in the cloudy morning of May 11, were removed from the filtered data set. From May 5-9, the FTS was operated in the target mode, taking alternate measurements among SVO, west Pasadena and Santa Anita Park. On May 10-11, standard measurement cycle was performed, resulting in fewer measurements from each target.

The SVO showed constant path-averaged mixing ratios of about 390 ppm XCO_2 , 1700 ppb XCH_4 and 100 ppb XCO during this period. The constant diurnal pattern was observed because the FTS is located mostly above the planetary boundary layer, where sources are located, and therefore the SVO measurements do not capture variations of atmospheric CO_2 , CH_4 and CO mixing ratio due to emissions in the Los Angeles basin.

On the other hand, the West Pasadena and Santa Anita reflection points observed strong diurnal signals in XCO_2 , XCH_4 and XCO with typically minimum in the early morning at around 405-410 ppm for XCO_2 , 1800-1900 ppb for XCH_4 and 100-150 ppb for XCO and a maximum at noon or in the early afternoon. Emissions of CO_2 , CH_4 and CO in the megacity resulted in daily variations of 10-30 ppm XCO_2 , 100-200 ppb XCH_4 and 100-200 ppb XCO during this period. Since the West Pasadena and the Santa Anita measurement paths span over 9 km and 11 km slant distances in the Los Angeles basin, they are able to pick up emission signatures. Despite the different measurement paths of the West Pasadena and the Santa Anita reflection points, the two showed consistency in XCO_2 , XCH_4 and XCO in general. The buildup of XCO_2 , XCH_4 and XCO in the morning and the falloff in the afternoon are due to a combination of accumulation of emissions and dilution/advection processes in basin. Similar diurnal patterns of XCO_2 , XCH_4 and XCO (that is, peak at noon or early afternoon) have been observed in Pasadena by TCCON (Wunch et al., 2009). However, the column enhancements observed by TCCON are typically

less than 2-3 ppm in XCO₂ and 20-40 ppb in XCH₄, due to the different measurement geometry from the CLARS-FTS.

4.4. Top-down Estimates of CH₄ Emissions

4.4.1. CH₄:CO₂ Ratio Originating From Los Angeles

Several studies have reported strong correlations between CH₄ and CO₂ measured in the PBL in source regions (Peischl et al., 2013; Wennberg et al., 2012; Wunch et al., 2009; S. Newman, personal communication, 2014). Slopes of CH₄:CO₂ correlation plots have been identified with local emission ratios for the two gases. Since the uncertainty in CH₄ emissions is considerably larger than that in CO₂ emissions, we may use the correlation slope to reduce the CH₄ emission uncertainties. Based on two years of data acquired between September 1, 2011 and October 30, 2013, we estimated the CH₄:CO₂ ratio originating from the megacity (Wong et al., 2014). The SVO observations were used as the background reference. The Los Angeles basin XCO₂ and XCH₄ excess mixing ratios above background were calculated by subtracting for SVO observations from the basin observations (Equation 4.5). These excess mixing ratios were related to emissions in the megacity.

$$XGHG_{\text{excess}} = XGHG_{\text{LABS}} - XGHG_{\text{SOV}} \quad (4.5)$$

Slopes of correlation between XCH₄ and XCO₂ excess were 7.3±0.1 ppb CH₄/ppm CO₂ for West Pasadena and 6.1±0.1 ppb CH₄/ppm CO₂ for Santa Anita during this period (Figure 4.13). The tight correlations imply that there is not substantial difference in the emission ratio of the two GHGs during the measurement period from 2011 to 2013. XCH_{4(XS)} and XCO_{2(XS)} should be poorly correlated with each other if their emission ratio varies largely over time, assuming the correlation is mainly driven by emissions.

Figure 4.14 maps the observed correlation slopes and their uncertainties for all the 28 basin reflection points across the Los Angeles basin using natural neighbor interpolation. Spatial variations of the correlation slope were observed among the 28 reflection points in the Los Angeles basin, varying from 5.4 to 7.3 ppb CH₄/ppm CO₂, with an average of 6.4±0.5 ppb CH₄/ppm CO₂ among all the reflection points. Spatial gradients among reflection points became weaker as distance from Mount Wilson increased. Stronger spatial gradients were observed among the closer reflection points in the basin, that is, west Pasadena, Santa Anita Park and East Los Angeles, while weaker spatial gradients were observed among the more distant reflection points, such as Long Beach, Marina Del Rey and North Orange County. Measurements were averaged over a much longer slant path for the more distant reflection points, compared to the nearby reflection points, making the measurements for the more distant reflection points less sensitive to local/point sources. Bootstrap analysis (Efron and Tibshirani, 1993) was performed to make sure that the spatial variations of the correlation slopes were not a result of sampling bias among the 28 reflection points. The uncertainties in the correlation slopes became larger with increasing distance from Mount Wilson due to the decreased data quality, as the measurement path in the Los Angeles megacity became longer. (More data were filtered out for targets further from the instrument, mostly because of aerosol loading.)

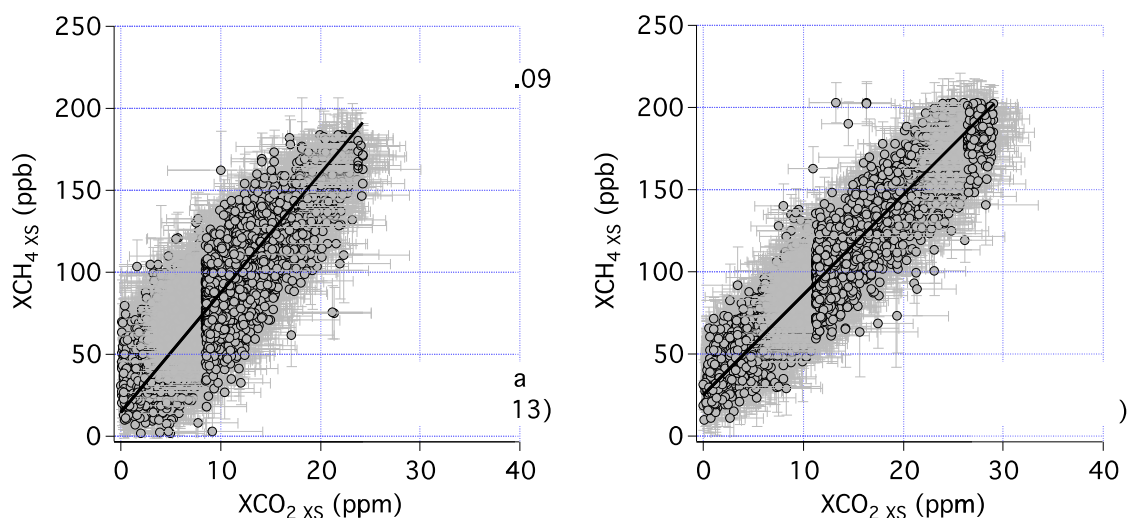


Figure 4.14: Correlations between XCH₄ excess (ppb) and XCO₂ excess (ppm) for West Pasadena (left) and Santa Anita Park (right) between the period of September 1, 2011 and October 30, 2013.

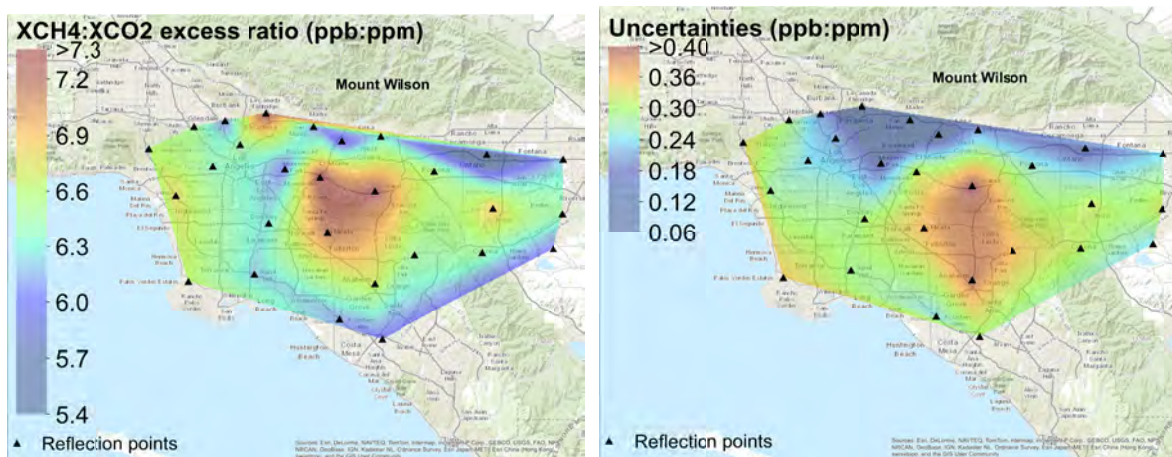


Figure 4.15: Left: Map of correlation slopes of XCH₄ excess to XCO₂ excess (ppb/ppm) in the Los Angeles basin calculated using CLARS-FTS measurement between the period of September 1, 2011 and October 30, 2013. Right: one standard deviation of the correlation slopes.

4.4.2. Implication for bottom-up CH₄ emission inventory

The CARB reported an annual statewide CO₂ emission of 387 Tg CO₂/year for 2011 (http://www.arb.ca.gov/app/ghg/2000_2011/ghg_sector.php). Assuming the CO₂ emissions are spatially distributed by population in the state, we apportioned the statewide emissions by population in the Los Angeles basin, which is 43%, to estimate the bottom-up emission for the Los Angeles basin (<http://www.census.gov/>). The bottom-up CO₂ emission for the Los Angeles basin was 167 Tg CO₂/year in 2011. For the bottom-up CH₄ emission in the Los Angeles basin,

we used the same method as in Wunch et al. 2009 and Peischl et al. 2013. That is, subtracting agriculture and forestry sector from the total statewide emission, then apportioned by population. This gave a bottom-up CH₄ emission of 0.278 Tg CH₄/year in the Los Angeles basin in 2011. Using the bottom-up emission inventory of CO₂ for the Los Angeles basin and the CH₄:CO₂ ratio observed by the CLARS-FTS, we derived the CH₄ emission using Equation 4.6, where $E_{CH_4}|_{top-down}$ is the top-down CH₄ emission inferred by the CLARS-FTS observations, $E_{CO_2}|_{bottom-up}$ is the bottom-up CO₂ emission, $\frac{X_{CH_4}}{X_{CO_2}}|_{slope}$ is the XCH₄:XCO₂ excess ratio observed by the FTS and $\frac{MW_{CO_2}}{MW_{CH_4}}$ is the ratio of molecular weight of CO₂ and CH₄. The derived CH₄ emission inventory was 0.382 Tg CH₄/ year in the Los Angeles basin. The derived CH₄ emission was 37% larger than the bottom-up emission inventory in 2011.

$$E_{CH_4}|_{top-down} = E_{CO_2}|_{bottom-up} \times \frac{X_{CH_4}}{X_{CO_2}}|_{slope} \times \frac{MW_{CO_2}}{MW_{CH_4}} \quad (4.6)$$

Because of the spatial variations of CH₄:CO₂ ratio in the Los Angeles basin, the derived CH₄ emission could vary significantly. For instance, if we were to evaluate the bottom-up CH₄ emission inventory by our observations in West Pasadena only, the derived CH₄ emission inventory for the Los Angeles basin would be overestimated by 21%, since the West Pasadena target observed a CH₄:CO₂ slope that is 21% larger than the average slope of the 28 reflection points.

4.4.3. Seasonal Variability

Seasonal spatial patterns of the XCH₄:XCO₂ excess ratio were observed in the Los Angeles basin with elevated CH₄:CO₂ ratio in the eastern side of the basin in summer (JJA) and fall (SON) seasons (Figure 4.15). These patterns were a result from variations in both CO₂ and CH₄ emissions and meteorological patterns in the Los Angeles basin. Cloudy conditions in spring (MAM) season limited data quality for more distant measurements. Using the seasonal variability of the basin average CH₄:CO₂ ratio, we derived the seasonal CH₄ emission in the basin ($E_{CH_4}|_{monthly, top-down}$), from the seasonal XCH₄:XCO₂ excess ratio observed by the FTS

($\frac{X_{CH_4}}{X_{CO_2}}|_{monthly, CLARS-FTS}$), the annual CARB bottom-up CO₂ emission ($E_{CO_2}|_{annual, bottom-up}$), the seasonal variability of CO₂ emission provided by the Vulcan emission database ($f_{CO_2}|_{monthly, Vulcan}$) and the

ratio of the molecular weights of the two greenhouse gases ($\frac{MW_{CH_4}}{MW_{CO_2}}$) as shown in equation 4.7.

The annual CARB bottom-up CO₂ emission for the Los Angeles basin was estimated by scaling the California statewide emission by population. The monthly XCH₄:XCO₂ excess ratios were the slope of correlations between XCH₄ and XCO₂ excess ratios observed for the Los Angeles basin.

$$E_{CH_4}|_{monthly, top-down} = E_{CO_2}|_{annual, bottom-up} \times f_{CO_2}|_{monthly, Vulcan} \times \frac{X_{CH_4}}{X_{CO_2}}|_{monthly, CLARS-FTS} \times \frac{MW_{CH_4}}{MW_{CO_2}} \quad (4.7)$$

As shown in Figure 4.16, the derived monthly CH₄ emission in the basin varied from 27 to 35 Gg CH₄/month, with larger values in wintertime in general. The spatial CH₄:CO₂ ratio maps

combined with an atmospheric transport model will allow the inversion of maps of CO₂ and CH₄ fluxes in the basin in the future.



Figure 4.16: Seasonal maps of correlation slopes of XCH₄ excess to XCO₂ excess (ppb/ppm) in the Los Angeles basin calculated using CLARS-FTS measurement between the period of September 1, 2011 and October 30, 2013.

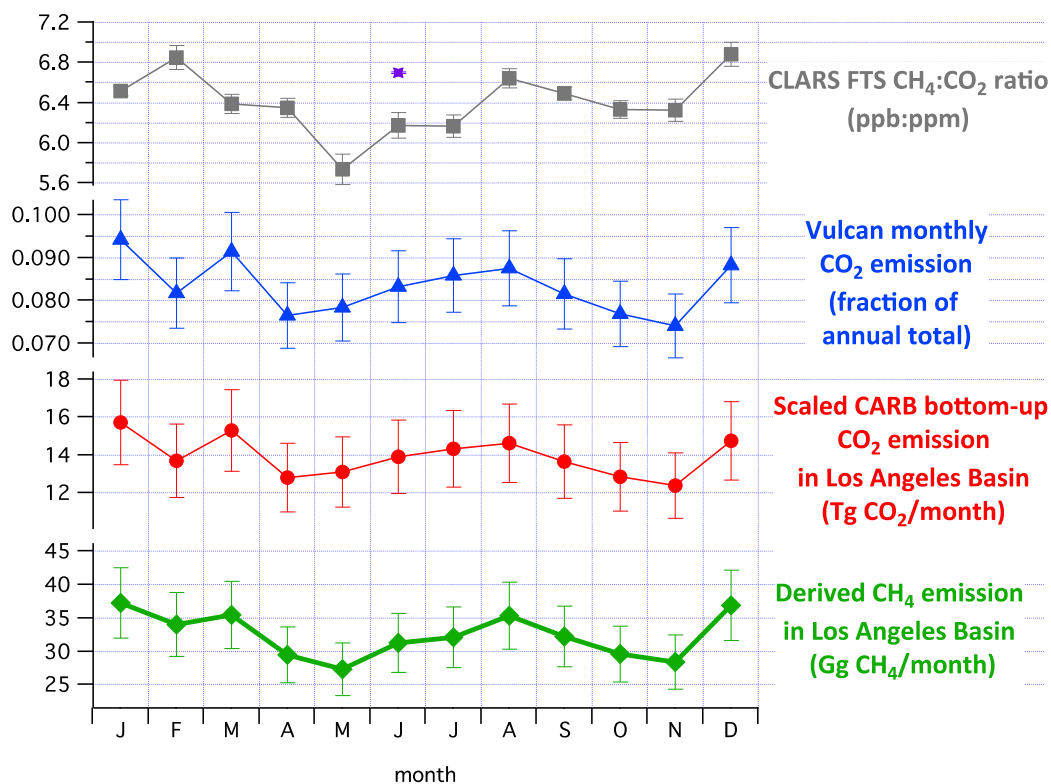


Figure 4.17: Monthly variations of Los Angeles basin averaged $XCH_4:XCO_2$ excess ratio (grey), Vulcan CO_2 emission (blue), scaled CARB bottom-up CO_2 emission (red) and derived CH_4 emission (green) in the Los Angeles basin. Purple dot indicates the $CH_4:CO_2$ ratio observed by aircraft during CalNex 2010 (Peischl et al., 2013).

4.5. Top-down Estimates of CO_2 Emissions

To derive CO_2 emissions in the basin, CO, which is co-emitted with CO_2 , was used as the tracer. CO is a criteria air pollutant regulated by the Environmental Protection Agency (EPA). As a result, CO emissions are believed to be better quantified than those of CO_2 .

4.5.1. CO: CO_2 ratio in the basin

Similar correlation analyses were performed between XCO excess and XCO_2 excess. Following Wunch et al. (2009), an averaging kernel correlation was applied to our ratio due to the different wavebands where the two gases were retrieved. Using data acquired between September 2011 and October 2014, we interpolated the correlation slopes of XCO excess and XCO_2 excess in the Los Angeles basin. Significant spatial variability in XCO excess to XCO_2 excess ratio, ranging from 3-7 ppb XCO/ ppm XCO_2 , was observed across the basin in this time period (Figure 4.18). In general, ratios were larger in the western Los Angeles basin than in the eastern basin. Figure 4.19 shows the seasonal pattern observed during the same period. Larger values of the XCO to XCO_2 excess ratio were recorded in summer than winter. Because CO and CO_2 are co-emitted, the spatial and temporal pattern of the ratio is an indication of combustion efficiency combined with transport processes. Future studies using an atmospheric transport

model are essential to disentangle the spatio-temporal pattern of emissions and atmospheric transport.

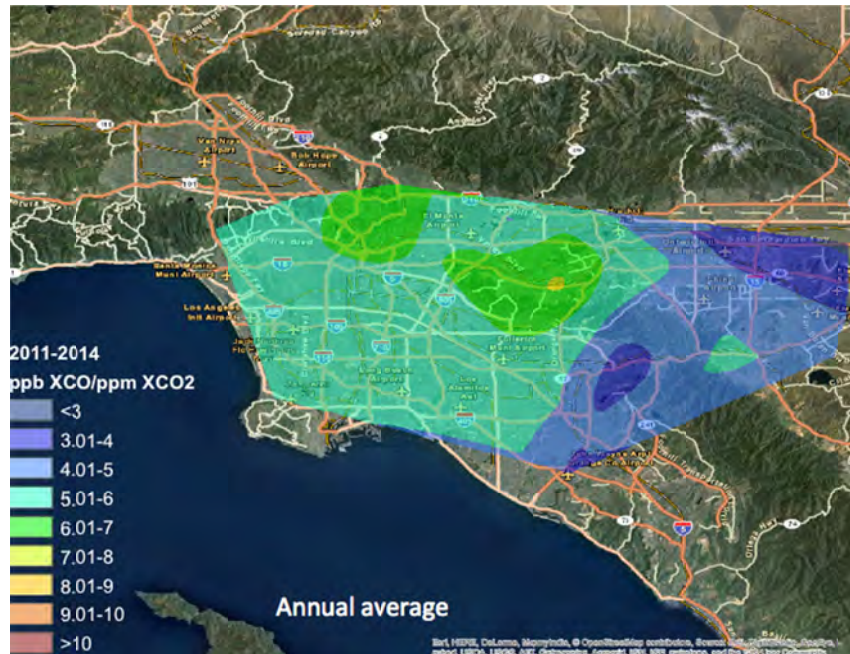


Figure 4.18: Map of correlation slopes of XCO excess to XCO₂ excess (ppb/ppm) in the Los Angeles basin calculated using CLARS-FTS measurement between the period of September 1, 2011 and October 30, 2014.

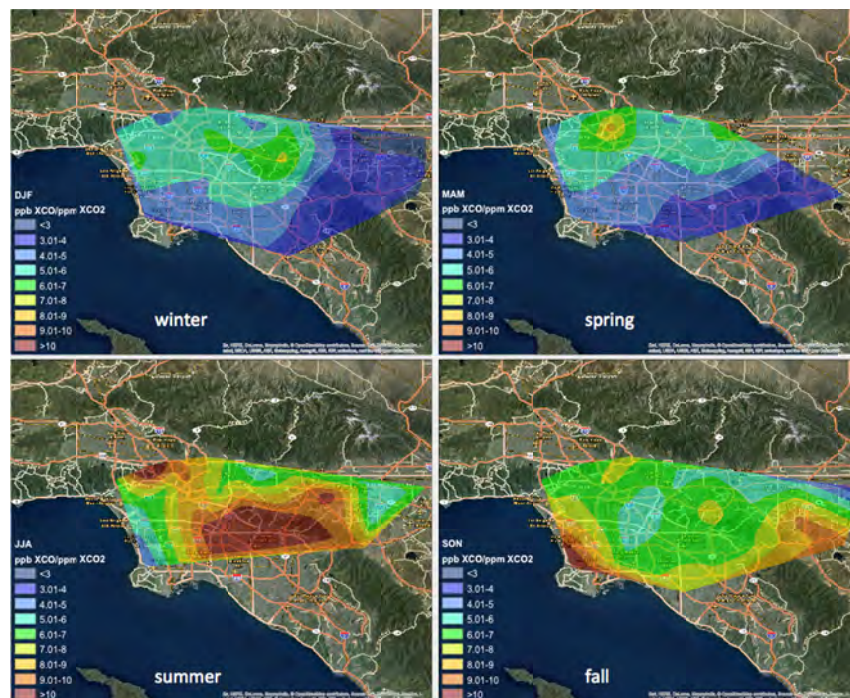


Figure 4.19: Seasonal-spatial variability in XCO excess to XCO₂ excess (ppb/ppm) ratio in the Los Angeles basin calculated using CLARS-FTS measurement between the period of September 1, 2011 and October 30, 2014.

4.5.2. Top-down CO₂ emission estimates from 2011 to 2014

Figure 4.20 (left panel) shows the annual trend of CO:CO₂ ratio observed by the FTS between the period of 2011 and 2014. The ratio had a slight decrease from around 6.5 ppb CO/ ppm CO₂ in 2011 to 5.8 ppb CO/ ppm CO₂ in 2012. It was slightly lower but consistent with the trend reported by the California Air Resources Board in 2011 and 2012. The observed CO:CO₂ ratio was relatively constant since 2012. We estimated the top-down CO₂ emissions using equation 4.8.

$$E_{CO_2|top-down} = E_{CO|bottom-up} \times \frac{X_{CO_2}}{X_{CO}}|_{slope} \times \frac{MW_{CO}}{MW_{CO_2}} \quad (4.8)$$

Annual CO emissions in the South Coast Air Basin were reported by the California Air Resources Board in 2010 and 2012 (<http://www.arb.ca.gov/app/emsmv/2013/emssumcat.php>). We extrapolated the CO emissions in 2011 based on emissions reported in 2010 and 2012 (Figure 4.20 middle panel). CO emissions in 2013 and 2014 were extrapolated based on the reported emissions in 2012 and forecasted emissions in 2015 provided by the California Air Resources Board. Using equation 4.8, we derived the annual top-down CO₂ emissions of 211±12 Tg CO₂/ year in 2011, 230±12 Tg CO₂/ year in 2012, 212±11 Tg CO₂/ year in 2013, and 204±10 Tg CO₂/ year in 2014 (Figure 4.20, right panel). The uncertainties of the derived emissions were calculated assuming a 5% uncertainty in the CARB CO emissions. The top-down CO₂ emissions had a slightly increasing trend from 2011 to 2012 and were about 10-15% greater than the CARB bottom-up CO₂ emissions.

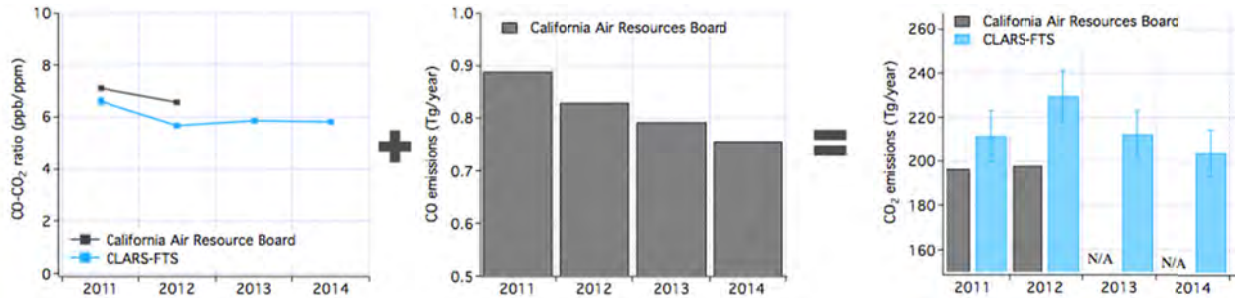


Figure 4.20: Yearly trend of observed Los Angeles basin average CO to CO₂ ratio (left), CARB CO emissions for the South Coast Air Basin (middle) and CO₂ emissions for the basin (right). CO emissions for 2013 and 2014 were extrapolated.

4.6. Comparison between CLARS Observations and WRF-VPRM Model

To further understand the FTS measurement and investigate greenhouse gas emissions in the Los Angeles basin, the CO₂ slant column densities (SCD) measured by CLARS have been compared to that of WRF-VPRM (Weather Research and Forecasting model coupled to Vegetation Photosynthesis and Respiration Model). Note: this analysis was complementary to the CARB-supported effort but not formally part of the scope of work.

The structure of the WRF-VPRM is shown in Figure 4.17(Park et al., 2011). The WRF model is initialized by the Carbon Tracker data. The WRF Preprocessing System (WPS) feeds in

terrestrial data and gridded data and prepares the domain for the WRF model. The WRF model generates meteorological data, such as the shortwave radiation and surface temperature, which are used to calculate the CO₂ biosphere fluxes based on the land surface water (LSWI) and enhanced vegetation index (EVI) measured by the Moderate-resolution Imaging Spectroradiometer (MODIS) (<http://modis.gsfc.nasa.gov/>), and model constraints such as Photosynthetically Active Radiation (PAR). The WRF Chemistry Tracer Transport Model calculates the CO₂ tracer transport based on the CO₂ biosphere fluxes and fossil fuel emission data and outputs the total CO₂ concentrations due to biogenic, anthropogenic and oceanic sources. Details of the WRF-VPRM model are described in Ahmadov et al. (2007) and reference therein. Model simulations of CO₂ concentrations in the Los Angeles basin during CalNex 2010 were performed by Qinbin Li's group at UCLA. Input data included the NCEP North American Regional NCEP North American Regional *Reanalysis (NARR) data at 30 km by 30 km resolution* (<http://nomads.ncdc.noaa.gov/>), *IC/BC from total CO₂ from GEOS-CHEM 2 by 2.5 degree resolution and Vulcan fossil fuel CO₂ emission data, which are fine resolution hourly emission data with less than 10 km, for 2002* (www.purdue.edu/eas/carbon/vulcan).

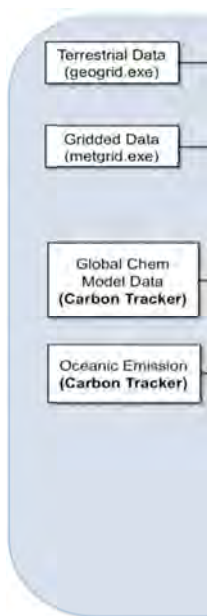


Figure 4.21: Structure of the coupled WRF-VPRM model.

3-D distributions of CO₂ volume mixing ratio (VMR) over Los Angeles basin with a 4-km resolution were simulated. The model domain covers the altitude range from surface to 16.5 km above sea level. Therefore, we developed algorithms to integrate the simulated CO₂ SCD along the solar light path ($CO_{2_SCD_WRF_VPRM}$) for the comparisons between the FTS measurements and model simulations. The integration is achieved by using Equation 4.9: first term represents the partial CO₂ SCD from the location of sun light entering the top boundary of the model domain to the location of CLARS site, and the second term uses the partial CO₂ SCD measured by CLARS FTS to fill in the altitude range where no model simulation is available.

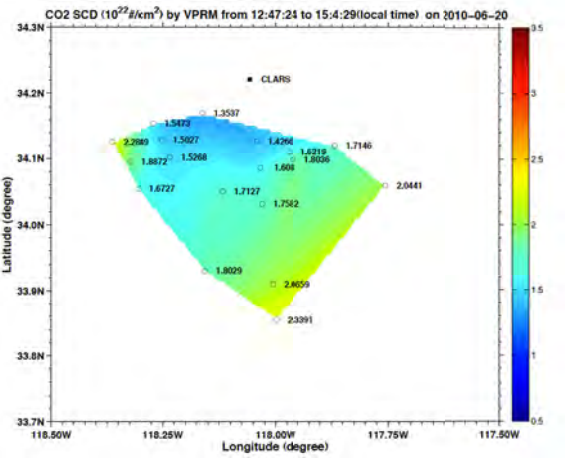
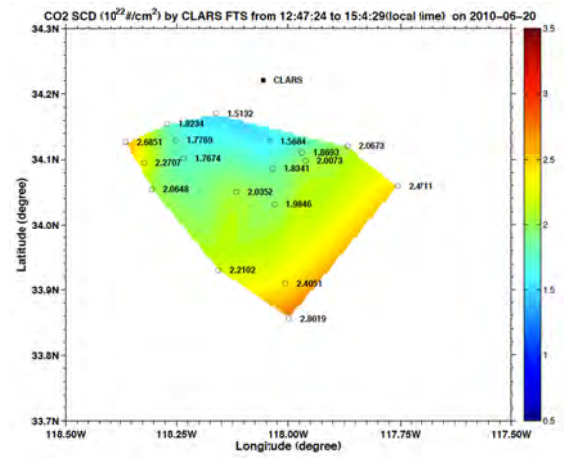
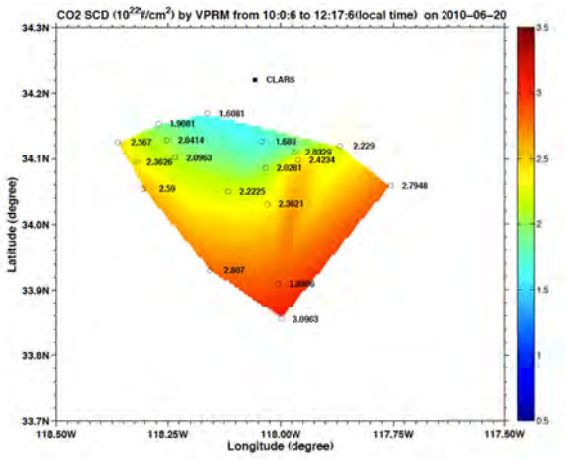
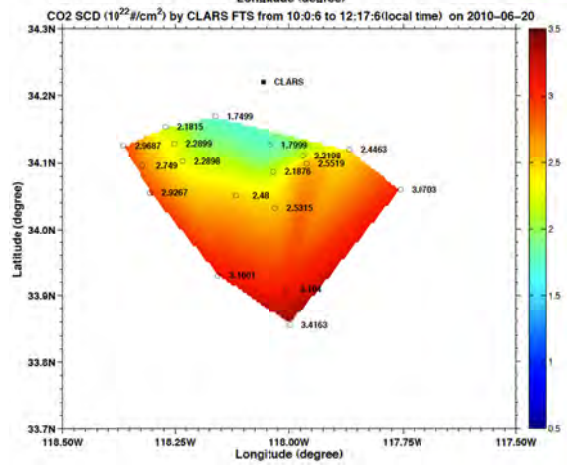
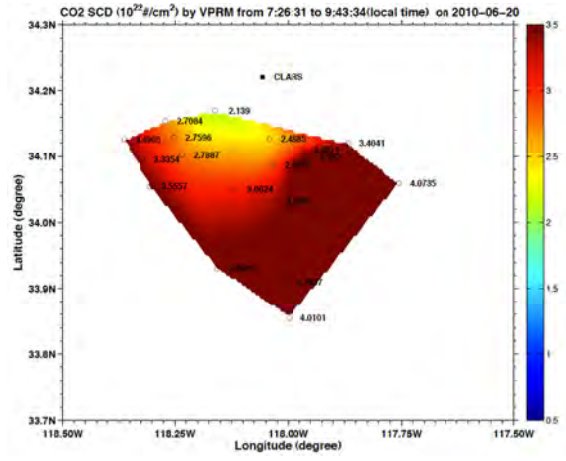
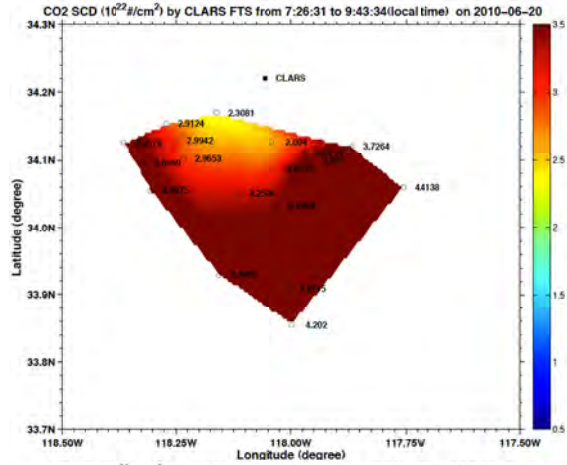
$$CO2_{SCD_WRF_VPRM} = \left(\sum_{i=1}^n (l_i \times VMR_{CO_2}(i) \times N_{air}(i)) \right) \times LPSF + CO2_{PSCD_CLARSFTS} \quad (4.9)$$

where, l_i is the geometric solar light path within the model layer i ; $VMR_{CO_2}(i)$ is CO_2 volume mixing ratio in the model layer i ; $N_{air}(i)$ is the air number density in the model layer i ; $LPSF$ is the light path scaling factor to account for the uncertainty of geometric light path (e.g., uncertainty arisen from the scattering events); $CO2_{PSCD_CLARSFTS}$ is the CO_2 partial SCD along the light path from 16.5 km to the top of atmosphere. Knowing the viewing geometry of each measurement, we applied Smit's algorithm (Smith B. 1998) to perform Ray-tracing calculations, which locate the model grid boxes that are in the light path of the FTS measurement by providing the index of model grid box (i) and slant distance (l_i). WRF-VRPM provides $VMR_{CO_2}(i)$ and $N_{air}(i)$. The $LPSF$ is determined using the following expression.

$$LPSF = \frac{O2_{CLARSFTS_SCD}}{O2_{Geometric_SCD}} \quad (4.10)$$

where, $O2_{CLARSFTS_SCD}$ is oxygen gas SCD measured by CLARS FTS, $O2_{Geometric_SCD}$ is the oxygen gas SCD along geometric light path.

Figure 4.21 shows the spatial-temporal distributions of the CLARS FTS observed and the WRF-VPRM simulated CO_2 SCD in the Los Angeles basin at 8:30 am, 11:00 am, 2:30 pm, and 4:30 pm respectively on June 20, 2010. Both measured and simulated CO_2 SCDs were interpolated onto a regular grid by using ordinary point kriging algorithm. *The time series of the observed and the modeled CO_2 SCD for all the target points in the Los Angeles basin on this day are shown in Figure 4.22.* The model simulations have good agreement with the FTS observations. The CO_2 SCD values of five measurements and simulation pairs are significant lower than the other pairs since they are the CO_2 SCDs of the SVO viewing. In general, the WRF-VPRM simulations have a low bias of 10% compared to that of CLARS FTS observation. In addition to the observations and simulations on June 20th, 2010, the spatial-temporal distribution of CO_2 SCD on multiple days during CalNex 2010 campaign show agreement between observations and simulations similar to that present in Figure 4.22. Meteorological parameters were reproduced reasonably well in the model. One possible reason of the underpredicted CO_2 in the model is the old CO_2 emission data from 2002 that is used in the model. In Los Angeles, where anthropogenic CO_2 emission dominates the total CO_2 emission, the actual anthropogenic emission of CO_2 in 2010 was likely to be larger than 2002, due to increase in fuel consumption and industrial activities. Model inversion will be performed in the future to estimate the CO_2 emissions in the Los Angeles basin.



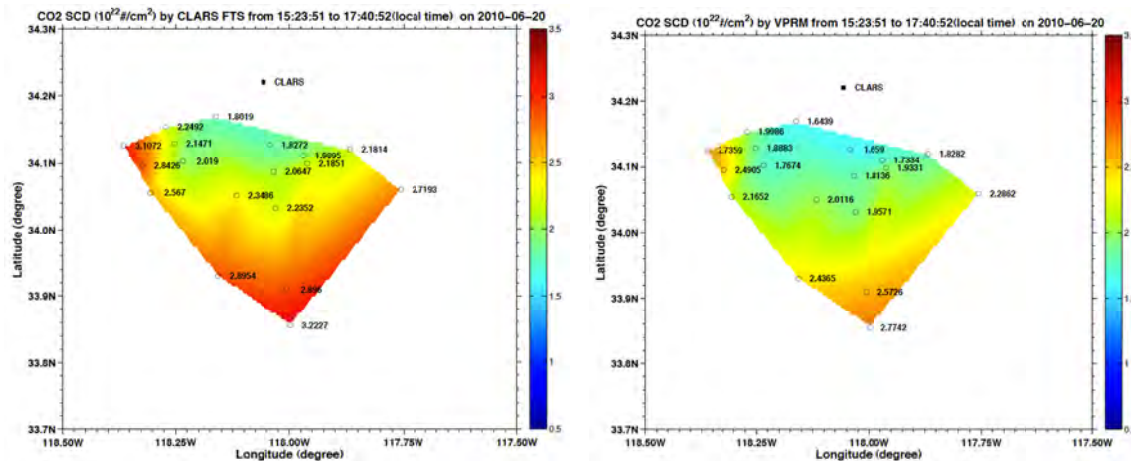


Figure 4.22: CO₂ SCD measured by CLARS FTS over LA basin (left column) and WRF-VPRM simulations (right column). The plots from top to bottom are representing the results during the time periods at 8:30 am, 11:00 am, 2:30 pm, and 4:30 pm on June 20th, 2010 respectively.

4.7. Future developments

Several improvements will be incorporated into future versions of the CLARS-FTS retrieval algorithm. These improvements include: (1) incorporation of a more advanced radiative transfer model which accounts explicitly for aerosol scattering to retrieve aerosol properties and for more robust data filtering. Absolute radiometric calibration of the FTS is being implemented to make use of this approach. (2) fine adjustment of target coordinates and the pointing system model to improve geolocation; (3) incorporation of line mixing and improved spectral line parameters to reduce systematic errors in the fitting residuals; (4) calibration of XCO₂, XCH₄, and XCO retrievals using aircraft and balloon in-situ profiles traceable to WMO standards; (5) further analysis of CH₄:CO₂ and CO:CO₂ ratio in Los Angeles such as seasonal and/or annual trends; and (6) assimilation of CLARS-FTS GHG observations using WRF model and model inversion to derive GHG emissions in the Los Angeles basin.

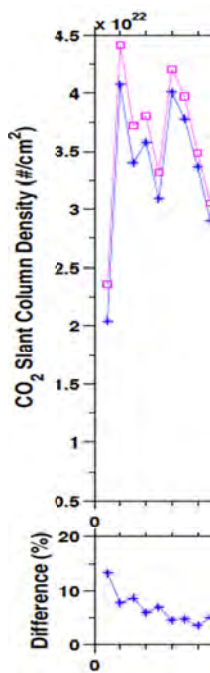


Figure 4.23: (Upper plot) CO₂ slant column densities over Los Angeles basin on June 20th, 2010; (Lower plot) the percentage differences between CLARS FTS measurements and WRF-VPRM simulations. The pair indexes indicate the time sequence (starts from #1 7:26 am, ends at #79 5:40 pm). The CO₂ SCD of 5 measurement and simulation pairs show significant lower values than other pairs since they are resampling the CO₂ SCDs above CLARS site (using measurements in the SVO viewing geometry).

5. Modeling

As part of this project we developed a version of WRF-Chem for the Los Angeles Basin. The model was run to simulate the CalNex period, and its results were compared to observations to gain information on the emission inventories of CO and NO_x. The inversion of the model based on observations to determine the correction of the inventories was not possible as the WRF-Chem adjoint did not become available in time for our project. We therefore pursued the alternate plan outlined in our proposal and performed the inversion directly to derive vertical aerosol extinction and NO₂ profiles as described above. We hope to pursue our original idea once a WRF-Chem adjoint becomes available. The following sections briefly describe the model setup, model results, and comparison of the model output to the observations. The conclusions for the emission inventories in the LA basin derived from the comparison will be discussed.

5.1. Model Setup

The Weather Research and Forecasting (WRF) model coupled with online chemistry (WRF-Chem) community model version 3.1.1 (<http://www.wrf-model.org/index.php> and <http://ruc.noaa.gov/wrf/WG11/>) was used with three nested domains with horizontal resolutions of 36, 12, and 4 km, respectively, with the finest resolution covering Southern California. 30 vertical layers extended from the surface to 100 hPa. Boundary conditions for meteorological variables were obtained from the North American Regional Reanalysis (NARR) 32 km 3-hourly data while default boundary conditions were used for trace gases in the outmost domain. A summary of physical parameterization options is shown in Table 5.1.

The simulation period is from May-June, 2010, coinciding with the CalNex observational period. The meteorological parameters were originally re-initialized at 00:00 UTC every three days to mitigate the problems of systematic error growth in long integrations (Lo *et al.*, 2008). However, we found that a more frequent re-initialization of 24h improved the performance of the meteorological model on certain days.

Table 5.1: *WRF-Chem model configurations.*

Aerosol scheme	MOSAIC (4 bins) (Zaveri <i>et al.</i> , 2008)
Photolysis scheme	Fast-J (Wild <i>et al.</i> , 2000)
Gas phase chemistry	CBM-Z (Zavner <i>et al.</i> , 1999)
Cumulus parameterization	Grell 3D ensemble scheme (Grell and Devenyi, 2002)
Short-wave radiation	Dudhia scheme (Dudhia, 1989)
Long-wave radiation	RRTM (Mlawer <i>et al.</i> , 1997)
Microphysics	WSM 3-class simple ice scheme (Hong <i>et al.</i> , 2004)
Advection scheme	Runge-Kutta 3 rd order (Wicker and Skamarock, 2002; Skamarock, 2006)
Land-surface model	NOAH LSM (Chen and Dudhia, 2001)
Boundary layer scheme	YSU (Hong <i>et al.</i> , 2006)
Meteorology initial and boundary conditions	NARR (32-km) initialized every 2 days, nudging for the outmost domain (Mesinger <i>et al.</i> , 2006)
Initial condition for chemical	5-day spin-up

species	
Boundary conditions for chemical species	averages of mid-latitude aircraft profiles (McKeen <i>et al.</i> , 2002)
Vertical layers	30
Biogenic Emission	Guenther <i>et al</i> (1993, 1994)

5.2. Emission Inventories

The anthropogenic emissions used in the model were based on the U.S. EPA 2005 National Emission Inventory-NEI'05 (U.S. EPA, 2010). Emissions of CO and NO_x were adapted to reflect the changes from 2005 to 2010 as will be discussed in the following.

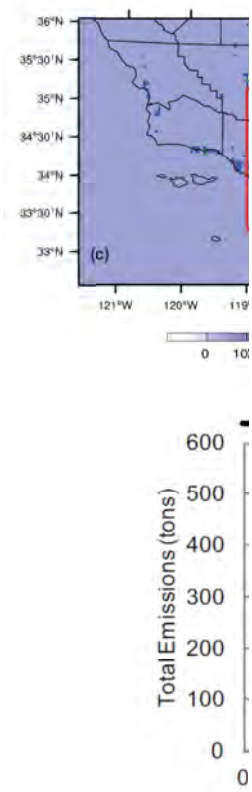


Figure 5.1: Anthropogenic CO emissions in the two inner domains and hourly variations in the innermost domain. The thick black rectangle in the upper right graph is the source region used in comparisons with NOAA WP-3D aircraft data

5.2.1. Carbon Monoxide

Anthropogenic CO emission in the inventory for the L.A. basin is ~4100 tons/day, with weekend/weekday ratios of 0.90 and 0.86 for Saturday and Sunday, respectively (Chinkin *et al.*, 2003; Sullivan *et al.*, 2004; Pollack *et al.*, 2012; Bahreini *et al.*, 2012). The spatial emissions

(Figure 5.1) reflect freeways and population centers in L.A. and Orange counties. The transportation sector contributes 90.5% of the total CO emissions (California Air Resource Board, 2012; data available at <http://www.arb.ca.gov/app/emsinv/emssumcat.php>). The diurnal variations in emissions (Figure 4.2) show a 10% CO emission reduction on the weekend.

To account for significantly reductions in CO and other pollutant emissions in California from 2005 to 2010, a scaling factor of 28% for CO was applied during weekdays and weekend (California Air Resource Board, 2012; data available at <http://www.arb.ca.gov/app/emsinv/emssumcat.php>).

5.2.2. Nitrogen Oxides

The diurnal and spatial variations of NO_x emission are similar to those of CO (Figure 5.2). In urban centers such as Long Beach (118.2°W, 33.8°N), Los Angeles (118.4°W, 33.9°N), and Irvine (117.8°W, 33.7°N) the transportation sector contributes 70-85% to the total NO_x emissions while in less densely populated cities a larger variety of sources, can be found in Kim *et al.* (2011).

Weekend-to-Weekday (WE-to-WD) emission changes are 22% and 26% on Saturday and Sunday, respectively, due to reduced weekend diesel truck traffic (Figure 5.2).

To consider the emission changes from 2005 to 2010, two emission scenarios were generated based on NEI'05_REF. In the baseline case (BASE_NO_x), emissions were reduced by 24% on weekends and weekdays (CARB emission projection, 2012; data available at <http://www.arb.ca.gov/app/emsinv/emssumcat.php>) In the low NO_x case (LOW_NO_x) NO_x emission were decrease by 45% on all days of the week relative to NEI'05_REF as suggested by Russell *et al.* (2010).

5.2.3. Hydrocarbons

Unlike NO_x emissions, which are dominated by on-road vehicles, VOC emissions also had significant contributions from area sources (solvent, paint and other residential sources) in the basin (CARB, 2012; data available at <http://www.arb.ca.gov/app/emsinv/emssumcat.php>), as well as biogenic sources. The biogenic emissions were calculated from the Guenther online scheme in the model (Guenther *et al.*, 1993 and 1994). In the model, VOC species are lumped into several functional groups based on structure and reactivity. Weekend emission changes of VOC vary by groups, with the ratios ranging from 0.89 to 1.14. The reactivity of the VOC groups is calculated based on the reactivity scales of the main compounds (Carter, 2013; data available at <http://www.engr.ucr.edu/~carter/SAPRC/>). The estimated total VOC reactivity R during the weekends is close to that on weekdays with a 1.02-1.04 weekend/weekday ratio. Overall, the inventories indicate that the NO_x/R ratio decreases on weekends in the basin.

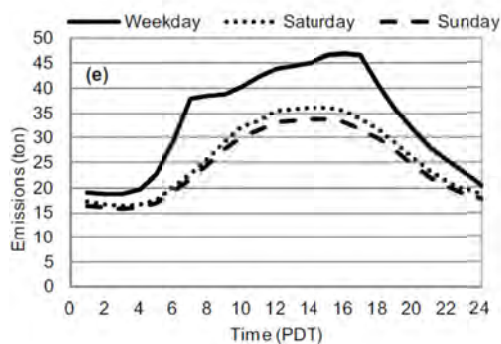


Figure 5.2: Daily averaged anthropogenic NO_x emissions in the two innermost domains and hourly variations in the innermost 4-km domain.

5.3. Comparison with observations

5.3.1. Meteorology

The model successfully capture day-to-day variations and the diurnal cycles of the various meteorological parameters (Table 5.2) Boundary layer heights (PBLH) at the Caltech site for May 27-June 15 are in good agreement with the observations during day and night, except during daytime on May 29-30 during the nights of June 1, 2, 6 and 9 (Figure 5.3). The aggregated statistics of a comparison of the model against aircraft data from five daytime flights (May 4, 14, 16, 19 and June 20) and two night-time flights (June 2 and 3) is included in Table 5.2. Generally daytime conditions are better represented in the model with higher correlations of temperature ($r^2 = 0.84$) and smaller RMSE of wind direction (Table 5.2).

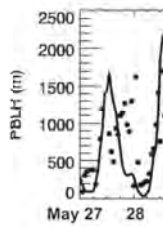


Figure 5.3: Simulated (solid lines) and observed (black dots) hourly averages planetary boundary layer height (PBLH) at the CalNex Caltech supersite (see Fig. 2b) for May 27-June 15, 2010.

Table 5.2: WRF-Chem simulated (MOD) and observed (OBS) temperature, wind speed, PBLH and water vapor at surface sites and across basin, bias (MOD-OBS), root mean square error (RMSE), standard deviations (S.D.) and correlations (r^2) between model results and observations.

	Temperature (K degree)							Wind Speed (m/s)						
	OBS	MOD	S.D.		Bias	RMSE	r^2	Mean		S.D.		Bias	RMSE	r^2
			OBS	MOD				OBS	MOD					
Caltech	292.6	293.5	4.6	5.1	0.9	2.0	0.85	1.0	2.5	0.7	1.3	1.5	1.2	0.19
Downtown L.A. Mean	293.6	293.4	2.6	3.6	-0.2	1.7	0.81	1.84	3.43	0.43	0.96	1.59	0.99	0.02
Fullerton	292.8	292.9	2.9	3.9	0.1	1.7	0.81	2.66	2.74	0.95	1.15	0.07	0.74	0.59
L.A. airport	290.8	290.8	1.4	2.3	0.0	1.6	0.53	3.35	2.61	1.35	1.35	-0.74	0.91	0.59
Ontario	294.9	295.9	5.3	5.7	1.0	1.8	0.90	3.31	3.79	1.59	2.18	0.48	1.12	0.76
Riverside	295.6	297.7	6.3	6.1	2.1	1.6	0.94	3.37	3.17	1.53	1.72	-0.21	0.92	0.71
Van Nuys	294.2	296.3	4.7	4.6	2.1	1.6	0.88	2.94	2.97	1.14	0.94	0.03	1.04	0.26
Across basin ^b														
Night time	287.6	289.0	2.4	2.6	1.5	1.8	0.55	4.4	4.8	2.5	3.0	0.3	2.4	0.39
Day time	289.8	290.4	3.9	4.8	0.6	2.0	0.84	4.6	4.1	2.2	1.6	-0.4	1.9	0.31

^aThe periods are May 27-June 15, 2010 for Caltech (*Pairs of data n>400*), and June 4-8, 2010 for other surface sites (*Pairs of data n > 100*).

^bThe results across basin were below 3 km; five daytime flights were on May 4, 14, 16 and 19, and June 20 (*Pairs of data n > 1000*).; two nighttime flights were on June 2 and 3 (*Pairs of data n > 600*).

The PBLH discrepancies on May 29-30 are associated with a positive bias of ~6 K in temperature and a positive bias of ~4-5 m/s in wind speed (not shown), which may be the cause of the erroneous PBLH simulation. Model re-initialization every 24h instead of every 72h significantly improves the meteorological simulations on May 30th. However the anomalous meteorology on May 29th, and especially the presence of a stratosphere intrusion (Langford et al. 2012) was not improved, showing the limits of the regional model. As simulations on other days did not change for the 24h re-initialization scheme we used the 72-hour re-initialization scheme for all days except for May 29-30.

5.3.2. CO

Surface CO from the Caltech site was compared to the model output for May 29-June 15 (Figure 5.5). The model overestimated CO mixing ratios by ~42%, excluding May 29-30. The observed daily maximum at 10:00-14:00 PDT is due to the transport of morning emissions near downtown L.A. (Veres et al., 2011), which is well captured by the model. The secondary CO peak at 7:00 am, which is likely due to local rush-hour traffic, is not well captured by the model. This may indicate that the 4-km horizontal resolution is too coarse to accurately consider local emissions in Pasadena.

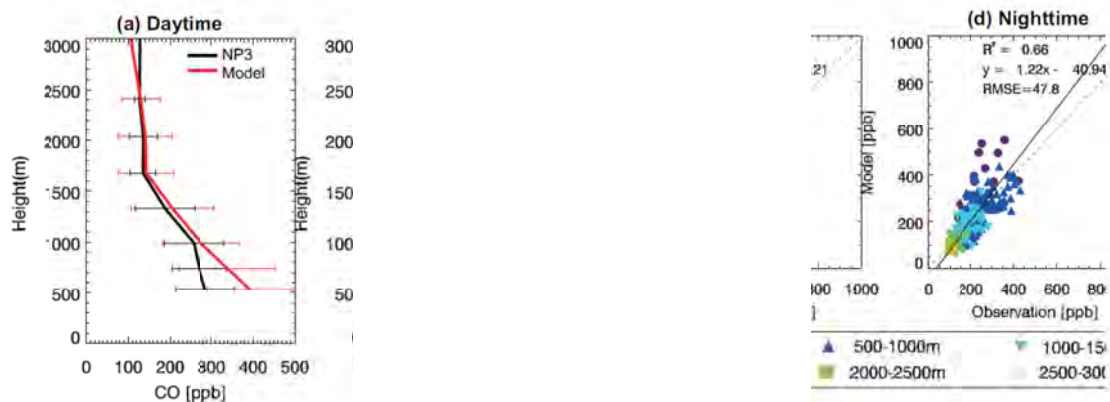


Figure 5.4: Simulated and observed concentrations of CO vertical profiles for the ensemble of CalNex flights during a) daytimes and b) nighttimes. The horizontal bars indicate the standard deviations. Also shown are the scatter plots (c-d), with values at different altitudes color-coded.

We also compared observations of CO below 3 km from the NOAA WP-3D to the model output (Figure 5.4) for an ensemble of flights. The modeled CO between 1-3 km shows good agreement with the observation. Only in the boundary layer (< 1 km during the day, < 400 m during nighttime) does the model overestimate CO. For example between 0.6-1 km, the model overestimates CO by ~60 ppb which is consistent with surface CO overestimation at 29 ARB sites (not shown). CO is overestimated by ~60-90 ppb in nocturnal boundary layer (NBL) below 500 m in the model.

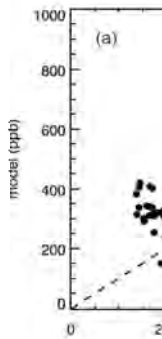


Figure 5.5: Simulated and observed surface concentrations of CO at the CalNex Caltech supersite for May 15-June 14, 2010: a) scatter plot, b) diurnal cycle. Values are hourly averages (unit: ppbv). The vertical bars are standard deviations.

Table 5.3: CO concentrations at surface sites and across the basin, Values at ARB sites are in steps of 100 ppbv. Units:ppbv.

		Mean		Median		S.D.		Bias	RMSE	r^2
		OBS	MOD	OBS	MOD	OBS	MOD			
At Surface sites ^a										
	Caltech	303	429	292	428	83	133	126	117	0.24
	North Long Beach			300	272					
	North Main Street			500	685					
	Azusa			400	499					
	Riverside			200	496					
	San Bernardino			300	511					
	Goleta			200	195					
	29 ARB sites daytime average			300	292					
	29 ARB sites nighttime average			300	396					
Across basin ^b										
< 3 km	Daytime	197	210	168	160	81	130	13	92	0.51
	Nighttime	177	175	161	156	67	81	-2	47	0.66
< 1.5 km	Daytime	223	249	216	246	81	134	26	102	0.41
	Nighttime	214	219	204	203	67	83	4	59	0.51

^a The periods are May 27-June 15, 2010 for all surface sites.

^b Five daytime flights were on May 4, 14, 16 and 19, and June 20; two nighttime flights were on June 2 and 3.

The aggregate statistics of all data points below 3 km and 1.5 km (Table 5.3) shows that the model overestimates daytime CO by 12-18% in the boundary layer. Due to the limited number of data points in the NBL, the model overestimations of nighttime near surface CO are not reflected in the statistics; however this can be seen in the comparisons with ARB sites (Table 5.3). The slopes of linear fit between modeled and observed CO during daytime and nighttime are 1.60 and 1.22 respectively.

Brioude et al. (2012) found that CO emissions were lower by $43\pm 6\%$ in L.A. County relative to NEI'05. While we used a 28% reduction from NEI'05 in our model study, the overestimation of modeled CO, both at the surface and across the basin, indicate that the CO emissions used in our model for the L.A. basin are still too high.

5.3.3. NO_x

O_3 , NO_x ($=\text{NO} + \text{NO}_2$), NO, NO_2 , O_x , HCHO and HNO_3 measured at the Caltech super site for May 27-June 15, 2010 (Figure 5.6) and CARB sites were compared to simulations with the baseline emission scenario (BASE_ NO_x). The CARB observations were also compared the LOW_ NO_x case simulations (Table 4.4 and Table 4.5). After excluding May 29-30, the day-to-day variation and diurnal cycle of O_3 was well simulated (*for May 27- June 15, correlations $r^2 = 0.63$, pairs of data $n > 470$, confidence value $p < 0.01$*) and afternoon O_3 was underestimated by 9.3 ppb (16%). Nocturnal O_3 was too low by 11.7 ppb (54%) in the model, most likely due to an inaccurate description of the $\text{NO} + \text{O}_3 \rightarrow \text{NO}_2 + \text{O}_2$ chemistry which is influenced by vertical mixing and surface NO emissions. Nocturnal $\text{O}_x = \text{O}_3 + \text{NO}_2$ mixing ratios, which are conserved in the $\text{O}_3 + \text{NO}$ reaction, were well simulated at Caltech (Table 4.4) confirming this hypothesis.

Day-to-day variations of NO, NO_2 and NO_x were captured well in the model with the exception of May 29-June 2. Modeled NO_2 and NO_x mixing ratios are 45% and 30% higher in the afternoon and 91% and 68% higher at night compared to the observations. HNO_3 mixing ratios were underestimated in the mode by 5% ($r^2 = 0.63$, $n > 400$), predominately during the night. A possible explanation is an incorrect description of N_2O_5 chemistry the model. The diurnal variation of HCHO is generally well modeled ($r^2 = 0.57$, $n > 470$) but shows an average bias of 0.65 ppb (30%) during afternoon peak hours and 1.06 ppb (110%) at night.

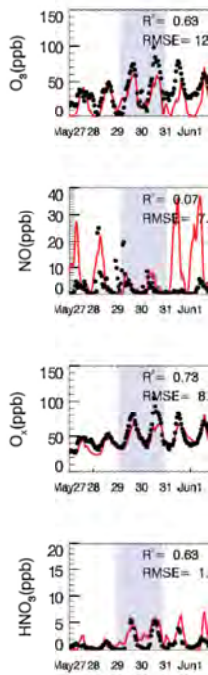


Figure 5.6: Simulated (solid red line) and observed (black dot) hourly averages of O₃, NO_y, NO, NO₂, O_x, HCHO and HNO₃ concentrations at the CalNex Caltech supersite (see Fig. 1b) for May 27-Jun 15, 2010. Model results are from the simulation with the BASE_NO_x emission scenarios (see text for details). The three weekends are color-coded.

Table 5.4: WRF-Chem simulated (BASE) and observed (OBS) surface chemical species concentrations (O₃, NO_y, NO, NO₂, HCHO, HNO₃) at the Caltech super site for May 27-June 15, 2010. Also listed are model biases, standard deviations (S.D.), root mean square error (RMSE) and correlations (r^2) between model results and observations. Model results are simulated by using emission scenario BASE_NO_x. Units:ppb (*pairs of data n > 400*).

	Mean		S.D		Bias BASE-OBS	RMSE	r^2	Daytime mean ^a		Nighttime Mean ^b	
	OBS	BASE	OBS	BASE				OBS	BASE	OBS	BASE
O ₃	36.2	25.6	19.5	18.3	-10.6	12.2	0.63	56.8	47.4	21.6	9.9
NO _x	21.8	27.7	10.0	13.0	6.1	15.6	0.01	21.6	20.8	19.9	30.8
NO	2.4	5.9	4.5	7.3	3.6	7.5	0.07	2.2	5.5	0.8	2.1
NO ₂	13.0	22.3	7.0	10.0	9.3	10.7	0.06	10.6	15.4	15.1	28.9
O _x	49.4	47.7	16.8	13.8	-1.7	8.8	0.73	67.5	62.4	36.9	38.6
HCHO	1.5	2.4	0.8	0.9	0.9	0.6	0.57	2.1	2.8	1.0	2.0
HNO ₃	3.1	3.0	3.1	2.8	-0.2	1.9	0.63	4.6	5.6	1.8	1.3

^a Daytime: 12:00-18:00 PDT

^b Nighttime: 22:00-3:00 PDT

Table 5.5: Same as Table 4.4, but for surface O₃, NO_x=NO+NO₂ at ARB sites for May 15- June 8, 2010. Model results are from two simulations with 45% (M1) and 24% (M2) NO_x emission reductions respectively. Units:ppbv (*pairs of data n > 500*).

	Mean			Bias		RMSE		<i>r</i> ²		
	OBS	M1	M2	M1 - OBS	M2 - OBS	M1	M2	M1	M2	
O ₃	At single site									
	North Long Beach	31.9	20.3	17.3	-11.6	-14.6	12.2	12.2	0.12	0.12
	North Main Street	28.9	22.5	17.1	-6.4	-11.8	11.6	11.0	0.57	0.56
	Reseda	41.0	34.4	31.7	-6.7	-9.3	11.4	12.0	0.61	0.57
	Riverside	43.8	38.2	32.8	-5.7	-11.1	12.5	12.0	0.70	0.71
	San Bernadino	36.4	36.8	29.7	0.4	-6.7	13.3	12.6	0.71	0.74
	El Cajon	33.7	34.4	32.6	0.7	-1.1	10.9	10.5	0.42	0.46
	20 sites Average									
	Nighttime	23.8	13.9	9.4	-9.9	-14.3	16.3	18.7	0.10	0.13
	Weekday daytime	48.7	49.8	43.0	1.1	-5.7	12.4	11.9	0.48	0.51
Weekend daytime	62.7	54.5	51.6	-8.1	-11.1	13.2	15.4	0.70	0.64	
NO _x	At single site									
	North Long Beach	18.9	25.9	37.2	7.0	18.3	21.8	30.2	0.10	0.10
	North Main Street	30.9	30.1	45.2	-0.7	14.4	17.6	21.9	0.20	0.19
	20 sites average									
	Nighttime	14.0	20.3	29.9	6.3	13.7	13.7	20.5	0.14	0.16
	Weekday daytime	14.1	12.5	15.5	-1.5	1.5	9.0	9.6	0.22	0.29
Weekend daytime	9.1	9.0	11.3	-0.1	2.1	7.3	9.8	0.35	0.38	

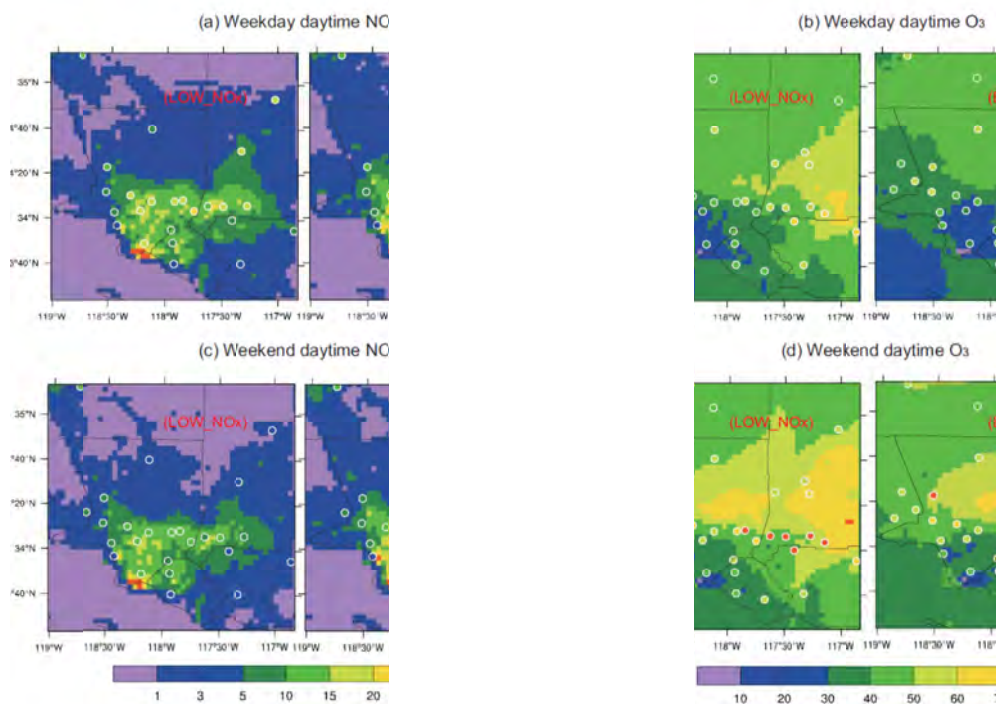


Figure 5.7: WRF-Chem simulated (color contour) surface NO_x and O_3 concentrations in the SCAB area averaged for May 15-June 6, 2010: (a-b) weekday daytime 12:00-18:00 PDT; (c-d) weekend daytime. Model results from two simulations are shown: LOW_ NO_x and BASE_ NO_x . CARB observations are overlaid as circled dots in same color scale. The units are ppb. O_3 data on May 29-30 (weekends) were excluded due to the already discussed problems with PBLH

The model performance in the entire inner model domain was tested by modeled NO_x and O_3 mixing ratios with observations from 20 CARB sites for both NO_x emissions cases (Figure 5.7 and Table 5.5). The increase of modeled daytime O_3 with decreasing NO_x emission indicates that the SCAB is NO_x -saturated (e.g. Qin *et al.*, 2004). On the other hand, weekend O_3 was less sensitive to NO_x emissions than weekday O_3 (6.8 ppb increase). It can thus be concluded that O_3 production is less NO_x -saturated on weekends than on weekdays.

A similar comparison was made using five NOAA-WP3 flights (Figure 5.8). NO_y is used as a better measure of NO_x emissions. NO_y , HNO_3 and PAN model output successfully captured afternoon plumes from Long Beach and Los Angeles. NO_y was overestimated in Long Beach, likely due to NO_x emissions being too high at the Long Beach. Correlations of O_3 , NO_y , HNO_3 and PAN from aircraft observations in the boundary layer (< 1.5 km) and the model are shown in Figure 5.9 and the resulting performance statistics are listed in Table 5.6. Weekday O_3 and NO_y on weekdays (Figure 5.8 a, c) was modeled well, with a negative bias of 2.3 ppb (4%) and 3.4 ppb (24%), respectively (Table 5.6). Weekends results showed larger discrepancies, with negative bias of O_3 (16.7 ppb, 23%), and a positive bias of NO_y (2.7 ppb, 40%) and HNO_3 (0.64 ppb, 27%).

Table 5.6: WRF-Chem simulated (LOW) and WP-3D observed (OBS) daytime O₃, NO_y, HNO₃ and PAN in boundary layer (<1.5 km) across basin (black rectangles in Fig. 1b and 1d) on weekdays (May 4, 14 and 19) and weekends (May 16 and June 20). Model results are with the LOW_NO_x emission scenario (see text for detail). Also listed are bias, root mean square error (RMSE), standard deviations (S.D) and correlations (r^2). Units: ppb. (*pairs of data n > 600*).

Species	Mean		Median		Bias LOW-OBS	RMSE	S.D.		r^2
	OBS	LOW	OBS	LOW			OBS	LOW	
Weekday									
O ₃	55.5	53.2	55.7	51.0	-2.3	12.4	12.5	12.0	0.24
NO _y	14.5	11.0	11.5	11.0	-3.4	9.4	11.5	8.0	0.34
HNO ₃	2.84	3.47	2.50	3.39	0.62	2.01	1.65	1.91	0.14
PAN	0.63	0.82	0.62	0.72	0.19	0.48	0.29	0.55	0.24
Weekend									
O ₃	72.8	56.1	73.2	53.5	-16.7	9.6	11.6	11.7	0.44
NO _y	6.6	9.3	5.8	9.0	2.7	4.7	4.8	6.7	0.51
HNO ₃	2.33	2.97	2.08	2.82	0.64	1.41	1.18	1.66	0.30
PAN	1.02	0.99	0.94	0.94	-0.03	0.44	0.60	0.69	0.60

Observed and modeled surface NO_x concentration showed a clear weekend effect with reductions from weekdays to weekends of 36% and 28%, respectively. This is reflected in the observations, which show a 14.0 ppb surface O₃ increase from weekdays to weekends. The model, however, showed only a 4.7-8.6 ppb increase in ozone, underestimating weekend O₃ by 11-17%. Boundary layer airborne observations also showed significant weekend-to-weekday differences with an average 17.2 ppb O₃ increase and 7.9 ppb (54%) NO_y decreases on weekends (Table 5.6). The model was not able to reproduce these observations, showing only a 2.9 ppb O₃ increase and 16% NO_y reduction (Table 5.5). The smaller NO_y reduction in the model is also reflected by a positive bias in weekend NO_y and HNO₃ of 40% and 27%, respectively. The most likely explanations for these results is that weekend NO_x emissions (22-26% reduction from weekday) are still too high in the model.

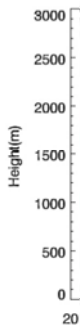


Figure .
ensemb
and Jun
examin
emissio

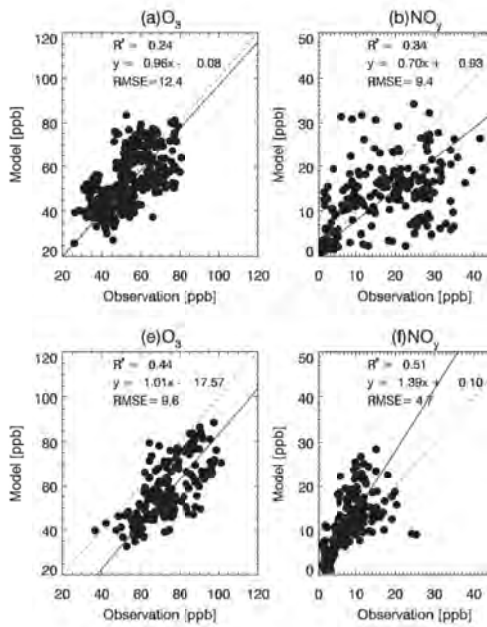


Figure 5.9: Simulated (Y-axis) and observed (X-axis) concentrations of O_3 , NO_y , HNO_3 and PAN for the ensemble of CalNex flights during weekdays (top) and weekends (bottom). Only data in the boundary layer (<1.5 km) and in the source region (black rectangle in Fig. 1d) are shown. Data over ocean is excluded. Model results are from the LOW_ NO_x emission scenario.

6. Conclusions

Two spectroscopic remote sensing instruments have been successfully deployed at the California Laboratory for Remote Sensing on Mt. Wilson, overlooking the LA Basin. Both systems have operated since 2010 and yielded a large amount of data on pollutants and greenhouse gases.

The multi-axis Differential Optical Absorption Spectroscopy instrument measured reflected and scattered sunlight in various viewing angles. In this report, we have primarily focused on the vertical dimension of those observations. We have developed the spectroscopic retrieval tools to derive path-averaged trace gas concentrations of NO₂, HCHO, and O₄ (a proxy for aerosol extinction). A cloud sorting algorithm was also developed and applied to exclude observations influenced by the presence of clouds. Most of our effort went into the development of the numerical tools to retrieve vertical aerosol extinction and trace gas concentration profiles from the observations. A combination of a fast radiative transfer model (VLIDORT) with an optimal estimation based inversion algorithm was found to give the best results for these retrievals. The retrievals are performed in a two-step process in which the aerosol extinction profile is retrieved first using a non-linear optimization approach, followed by a second linear step to derive the NO₂ concentration profiles. A theoretical information content analysis using this tools confirmed that the retrievals can derive 3-4 pieces of information on aerosol extinction and approximately 5 pieces of information on NO₂. Our approach is thus able to retrieve vertical profiles with a height resolution of ~400m. Example retrievals of actual observations showed that our actual retrievals are somewhat lower with an average of 3-4 degrees of freedom for NO₂. The lower value is likely due non-ideal conditions that can occur in the atmosphere, such as horizontal inhomogeneities in the aerosol and NO₂ distribution. We thus applied our approach to the 2011-2013 observational dataset. Comparison with selected data shows a good agreement of the vertically integrated aerosol extinction values with total optical density from an AERONET station located on the Caltech campus. The comparison also identified issues for some retrievals, which could again be caused by non-ideal conditions in the atmosphere. Work is ongoing to better understand which conditions lead to these problems. Comparison with surface NO₂ measurements revealed a good agreement with our retrievals, considering the differences in observation strategy, i.e. the MAX-DOAS integrates in the horizontal and has a limited vertical resolution while the in-situ data could be impacted by local emissions. The full data-set of aerosol extinction and NO₂ profiles will be made available to the ARB at the end of the project.

As the quality of our instrument allowed the successful retrieval of HCHO and NO₂ in a wavelength range that is typically not used for NO₂ retrievals, we also applied a method to monitor ozone formation sensitivity. The HCHO/NO₂ ratio was used as a proxy of ozone sensitivity after relating it to the more commonly used marker Ln/Q (Kleinman et al., 1997). The cross-over point between cross-over point between the VOC and NO_x sensitive regimes for the HCHO/NO₂ ratio was determined in collaboration with P. Stevens at the University of Indiana using his observations of OH, HO₂, and other trace gases during the CalNex Los Angeles field study in 2011. A HCHO/NO₂ ratio of 0.55 was identified as the cross-over point for the CalNex period. The daily averaged HCHO/NO₂ ratios from Mt. Wilson show a clear pattern with higher ratios, indicative of decreased VOC sensitivity, during the weekends, and lower ratios during the weekdays. The monthly averaged NO₂ and HCHO DSCDs from Mt. Wilson from 2011-2013 show that this weekend effect is caused by lower NO₂ levels on the weekends. The data also shows a decrease in monthly averaged NO₂ slant column densities during weekdays, while

weekend NO_2 does not seem to decrease as much. This trend, however, is not reflected in the long-term trend of HCHO/NO_2 ratios.

We have developed an automated atmospheric observatory to measure the GHG emissions over the Los Angeles basin. Near-infrared solar absorption spectra have been acquired continuously since May 2010. The slant column densities of GHG and O_2 , which were obtained from spectral fits, were utilized to compute the column-average GHG VMR (XCO_2 , XCH_4 , and XCO). The quality of spectral fits and the measurement precisions are estimated using the measurements on January 3rd and 18th, 2013 under clear sky conditions. The spectral fitting residuals of individual spectral segments were dominated by the random noise with RMS of fitting residuals being better than 0.3% and 0.5% for the measurements above the CLARS site and LA basin targets. The systematic fitting residuals are less than 0.5%. They are attributed to known uncertainty in the GHG spectroscopic line strengths and air-broadened width parameters and the uncertainty in the disk integrated solar spectra. Compared to the background levels, XCO_2 over Santa Anita Park and west Pasadena show higher values (6.26 ppm and 6.11 ppm) and present stronger diurnal cycles than those measurements over the CLARS site. The precisions of retrieved XCO_2 , XCH_4 , and XCO over CLARS are 0.09%, 0.14% and 1.94%. For the measurements over LA basin targets (Santa Anita Park and west Pasadena), the precisions of retrieved XCO_2 , XCH_4 , and XCO are 0.16% and 0.22%, 0.26% and 0.48%, 4.10% and 8.04%. The high measurement precisions of CLARS-FTS provide the capabilities of capturing the diurnal variations of XCO_2 , XCH_4 , and XCO over LA basin targets and the differences among the LA basin targets. The calibration of XCO_2 , XCH_4 , and XCO retrievals using aircraft in-situ profiles will be accomplished in the near future. Using ratio analysis, the CLARS-FTS observations suggested that the CH_4 emission inventory of the Los Angeles in 2011-2013 to be 0.382 Tg CH_4 / year, which was 37% above the bottom-up CH_4 emission inventory. Seasonal variability in the derived CH_4 emissions ranged from 27 to 35 Gg CH_4 /month, with larger values in wintertime in general. CLARS-FTS observations implied that the CO_2 emissions to be 211 Tg CO_2 / year in 2011, 230 Tg CO_2 / year in 2012, 212 Tg CO_2 / year in 2013, and 204 Tg CO_2 / year in 2014. Derived CO_2 emissions were 10-15% larger than the bottom-up CO_2 emissions in 2012. Spatial and temporal patterns of XCO_2 in the Los Angeles basin observed by the CLARS-FTS are simulated by WRF-VPRM model. The model results have a low bias of 10% compared to that of CLARS FTS observations. Model inversion will be performed to derive GHG emissions in the Los Angeles basin.

We successfully implemented the regional air quality model WRF-Chem for the LA Basin. Meteorological conditions, CO and NO_x were validated using the CalNex campaign (May-June 2010). The model meteorology performed well, except during two days with unusual meteorological conditions, such as a stratospheric intrusion event. CO concentrations at the Caltech and the inland source region during the day and night were overestimated by 42%, ~20% and 30-50%, respectively. The high bias in CO in the basin suggests that the CO emissions (28% reduction from NEI'05) were still too high. A 45% reduced NO_x emissions rate relative to NEI'05 improved model performance relative to a 24% NEI reduction case for daytime NO_x and O_3 in the source region. The lower NO_x emissions increased O_3 by 6.8 ppb and 2.9 ppb on weekdays and weekends respectively in the model, indicating that O_3 formation in the basin is NO_x -saturated. The relatively smaller O_3 increase on weekends may indicate that modeled weekend O_3 production is shifted to be less NO_x -saturated compared to weekdays. The modeled weekend-to-weekday difference was much smaller than the observations with a small 2.9 ppb O_3 increase and a 16% NO_x reduction. Together with overestimated NO_y on weekends and

underestimated NO_y on weekdays in the basin we conclude that a 22-26% weekend-to-weekday difference in NO_x emissions in the model is not large enough and weekend NO_x emissions were still overestimated in the model. The results reported here have been published in Atmospheric Environment in 2013 (Chen et al., 2013).

7. References

- Ahmadov, R., Gerbig, C., Kretschmer, R., Koerner, S., Neininger, B., Dolman, A. J., and Sarrat, C.: Mesoscale covariance of transport and CO₂ fluxes: Evidence from observations and simulations using the WRF-VPRM coupled atmosphere-biosphere model, *J. Geophys. Res.*, 112, D22107, doi:10.1029/2007JD008552, 2007.
- Aliwell, S. R., Van Roozendaal, M., Johnston, P., Richter, A., Wagner, T., Arlander, D., et al., Analysis for BrO in zenith-sky spectra: An intercomparison exercise for analysis improvement. *J. Geophys Res*, 107(D14), 1–20. doi:10.1029/2001JD000329, 2002.
- Bahreini, R., Middlebrook, A.M., de Gouw, J.A., Warneke, C., Trainer, M., Brock, C.A., Stark, H., et al., Gasoline emissions dominate over diesel in formation of secondary organic aerosol mass, *Geophys. Res. Lett.*, 39. doi: 10.1029/2011gl050718, 2012.
- Bekker, D. L., Blavier, J. -F. L., Toon, G. C., and Servais C.: An FPGA-based Data Acquisition and Processing System for the MATMOS FTIR Instrument, *Aerospace Conference Proceedings, 2009 IEEE*, vol. 1, pp. 1-11, doi:10.1109/AERO.2009.4839459, Big Sky, Montana, March 7th to 14th, 2009.
- Bekker, D. L., Blavier, J. L., Fu, D., Key, R. W., Manatt, K. S., McKinney, C., Rider, D. M., Sander, S. P., Werne, T. A., Wu, A. C., Wu, Y. H.: Command and data handling system for the panchromatic Fourier transform spectrometer, *Aerospace Conference Proceedings, 2012 IEEE*, vol. 1, pp. 1-10, doi:10.1109/AERO.2012.6187224, Big Sky, Montana, March 3rd to 10th, 2012.
- Bekker, D. L., Lukowiak, M., Shaaban, M., Blavier, J. -F. L., and Pingree, P. J.: A Hybrid-FPGA System for On-Board Data Processing Targeting the MATMOS FTIR Instrument, *Aerospace Conference Proceedings, 2008 IEEE*, vol. 1, pp. 1-15, doi:10.1109/AERO.2008.4526400, Big Sky, Montana, March 1st to 8th, 2008.
- Bergland, G.: A radix-eight fast Fourier transform subroutine for real-valued series, *IEEE Transactions on Audio and Electroacoustics*, 17(2), 138-144, 1969.
- Brasunas, J. C. and Cushman, G. M.: Uniform Time sampling Fourier Transform Spectroscopy, *Appl. Opt.*, 36(10), doi: 10.1364/AO.36.002206, 2206-2210, 1997.
- Brault, J.W., Brown, L.R., Chackerian, C., Freedman, R., Predoi-Cross, A., Pine, A.S., Self-broadened ¹²C¹⁶O line shapes in the $\nu = 2 \leftarrow 0$ band. *J. Mol. Spectrosc*, 222, 220–39, 2003.
- Brault, J.W.: New approach to high-precision Fourier transform spectrometer design, *Appl. Opt.* 35(16), doi:10.1364/AO.35.002891, 2891-2896, 1996.
- Brioude, J., Kim, S.W., Angevine, W.M., Frost, G.J., Lee, S.H., McKeen, S.A., Trainer, M., Fehsenfeld, F.C., Holloway, J.S., Ryerson, T.B., Williams, E.J., Petron, G., and Fast, J.D., Top-down estimate of anthropogenic emission inventories and their interannual variability

- in Houston using a mesoscale inverse modeling technique, *J. Geophys. Res.*, 116. doi: 10.1029/2011jd016215, 2011..
- Brown, L. R., Benner, D. C., Champion, J. P., Devi, V. M., Fejard, L., Gamache, R. R., Gabard, T., Hilico, J. C., Lavorel, B., Loete, M., Mellau, G. C., Nikitin, A., Pine, A. S., Predoi-Cross, A., Rinsland, C. P., Robert, O., Sams, R. L., Smith, M. A. H., Tashkun, S. A., Tyuterev, V. G.: Methane line parameters in HITRAN, *J. Quant. Spect. Rad. Trans.*, 82, 219–38, 2003.
- California Air Resource Board, 2009 almanac emission projection data. data available at <http://www.arb.ca.gov/app/emsinv/emssumcat.php> (accessed Nov 2011), 2012.
- California Air Resource Board, Air quality data query tool. data available at <http://www.arb.ca.gov/aqmis2/aqdselect.php> (accessed Nov 2011), 2012.
- California Air Resource Board, Air quality data statistics. data available at <http://www.arb.ca.gov/adam/index.html> (accessed Nov 2011), 2012.
- Campbell J., Synthetic quadrature phase detector/demodulator for Fourier transform spectrometers, *Appl. Opt.*, 47(36), 6889-6894, 2008.
- Cantrell, C. A., Davidson, J. A., McDaniel, A. H., Shetter, R. E., and Calvert, J. G.. Temperature-dependent formaldehyde cross sections in the near-ultraviolet spectral region. *J. Phys. Chem.*, 94(10), 3902–3908, 1990.
- Chen F., and Dudhia J., Coupling an advanced land-surface (hydrology model with the Penn State (NCAR MM5 modeling system. Part I: Model description and implementation, *Monthly Weather Review*, 129, 569-585, 2001.
- Chen, D., Q. Li, J. Stutz, Y. Mao, L. Zhang, O. Pikelnaya, J.Y. Tsai, C. Haman, B. Lefer, B. Rappenglück, S.L. Alvarez, J. A. Neuman, J. Flynn, J. M. Roberts, J. B. Nowak, J. de Gouw, J. Holloway, N.L. Wagner, P. Veres, S.S. Brown, T.B. Ryerson, C. Warneke, I.B. Pollack, WRF-Chem simulation of NO_x and O₃ in the L.A. basin during CalNex-2010, *Atmos. Environ.*, 81, 421-432, <http://dx.doi.org/10.1016/j.atmosenv.2013.08.064>, 2013
- Chinkin L. R., Coe D. L., Funk T. H., Main H. H., Roberts P. T., Ryan P. A., and Lawson D. R., Weekday versus weekend emissions activity patterns in California’s South Coast Air Basin. *J. Air Waste Man. Assoc.*, 53, 829-843, 2003.
- Connes, J.: Recherches sur la spectroscopie par transformation de Fourier, *Revue d’Optique*, 40, 45–79, 116–140, 171–190, 231–265, 1961, translated into *English by Flanagan, C. A., Spectroscopic Studies Using Fourier Transform, vol. 3157, U.S. Naval Ordnance Test Station Technical Publication, Inoyokern, California, 1963.*
- Croes, B. E.: New Directions: California’s programs for improving air quality and minimizing greenhouse gas emissions, *Atmos. Environ.*, 47, 562–563, doi:10.1016/j.atmosenv.2010.05.041, 2012.
- Davis, S. P., Abrams, M. C., and Brault, J. W.: *Fourier Transform Spectrometry, 2nd edn.*, Academic Press, San Diego, California, 2001.
- Deutschmann, T., Beirle, S., Frieß, U., Grzegorski, M., Kern, C., Kritten, L., Platt, U., Prados-Roman, C., Pukite, J., Wagner, T., Werner, B., and Pfeilsticker, K.. The Monte Carlo

- Atmospheric Radiative Transfer model McArtim: Introduction and validation of Jacobians and 3D features. *J. Quant. Spectrosc. Radiat. Transfer.* 112, 1119-1137, 2011
- Dudhia J., Numerical study of convection observed during the winter monsoon experiment using a mesoscale two-dimensional model, *J. Atmos. Sci.*, 46, 3077-3107, 1989.
- Duncan, B., Y. Yoshida, J. R. Olson, S. Sillman, R. V. Martin, L. Lamsal, Y. Hu, K. E. Pickering, C. Retscher, D. J. Allen, J. H. Crawford, Application of OMI observations to a space-based indicator of NO_x and VOC controls on surface ozone formation. *Atmos. Environ.*, 442213-2223, 2010
- Fishman, J., Iraci, L. T., Al-Saadi, J., Chance, K., Chavez, F., Chin, M., Coble, P., Davis, C., DiGiacomo, P.M., Edwards, D., Eldering, A., Goes, J., Herman, J., Hu, C., Jacob, D., Jordan, C., Kawa, S. R., Key, R., Liu, X., Lohrenz, S., Mannino, A., Natraj, V., Neil, D., Neu, J., Newchurch, M., Pickering, K., Salisbury, J., Sosik, H., Subramaniam, A., Tzortziou, M., Wang, J., Wang, M.: The United States' next generation of atmospheric composition and coastal ecosystem measurements: NASA's Geostationary Coastal and Air Pollution Events (GEO-CAPE) mission, *B. Am. Meteorol. Soc.*, 93, 1547–1566, doi:10.1175/BAMS-D-11-00201.1, 2012.
- Forman, M. L., Steel, W. H., and Vanasse, G. A.: Correction of asymmetric interferograms obtained in Fourier spectroscopy, *J. Opt. Soc. Am.*, 56(1), 59–63, doi: 10.1364/JOSA.56.000059, 1966.
- Frankenberg, C., Warneke, T., Butz, A., Aben, I., Hase, F., Spietz, P., and Brown, L. R.: Pressure broadening in the $2\nu_3$ band of methane and its implication on atmospheric retrievals, *Atmos. Chem. Phys.*, 8, 5061-5075, 2008.
- Frieß, U., Monks, P. S., Remedios, J. J., Rozanov, A., Sinreich, R., Wagner, T., and Platt, U., MAX-DOAS O₄ measurements: A new technique to derive information on atmospheric aerosols: 2. Modeling studies. *J. Geophys. Res.*, 111(D14), 1–20. doi:10.1029/2005JD006618, 2006.
- Fu, D., Sung, K., Boone, C. D., Walker, K. A., Bernath, P. F.: Ground-based solar absorption studies for the Carbon Cycle science by Fourier Transform Spectroscopy (CC-FTS) mission, *J. Quant. Spect. Rad. Trans.*, 109, 2219–2243, 2008.
- Fu, D., T.J. Pongetti, J.F.L. Blavier, T.J. Crawford, K.S. Manatt, G.C. Toon, K.W. Wong, and S.P. Sander, Near-infrared remote sensing of Los Angeles trace gas distributions from a mountaintop site, *Atmos. Meas. Tech.*, 7, 713-729, doi:10.5194/amt-7-713-2014, 2014.
- Geller, M.: A high resolution atlas of the infrared spectrum of the Sun and the Earth atmosphere from space, volume III. Key to identification of solar features from 650 to 4,800 cm⁻¹; *NASA Reference Publication 122*; NASA: Washington, DC, USA, 1992.
- Geller, M.: Line identification in ATMOS solar spectra. In Laboratory and Astronomical High Resolution Spectra; Proceedings of ASP Conference No. 81, Brussels, Belgium, 29 August–2 September 1994; *ASP Conference Series*; Sauval, A.J., Blomme, R., Grevesse, N., Eds.; *Astronomical Society of the Pacific: San Francisco, CA, USA*, page 81, 1995.

- Gordon, I. E., Kassi, S., Campargue, A., Toon G. C.: First identification of the $a^1\Delta_g - X^3\Sigma_g^-$ electric quadrupole transitions of oxygen in solar and laboratory spectra, *J. Quant. Spect. Rad. Trans.*, 111, 1174-1183, 2010.
- Greenblatt, G. D., Orlando, J. J., Burkholder, J. B., and Ravishankara, A. R., Absorption Measurements of Oxygen Between 330 and 1140 nm. *J. Geophys. Res.*, 95(D11), 18577–18582. doi:10.1029/JD095iD11p18577, 1990.
- Grell G. A., and Dévényi D., A generalized approach to parameterizing convection combining ensemble and data assimilation techniques, *Geophys. Res. Lett.*, 29, 1693. doi:10.1029/2002GL015311, 2002.
- Griesmann, U., Kling, R., Burnett, J. H., and Bratasz, L.: The NIST FT700 Vacuum Ultraviolet Fourier Transform Spectrometer: applications in ultraviolet spectrometry and radiometry, *Proc. SPIE 3818*, 180–188, 1999.
- Griffiths, P. R., De Haseth, J. A.: *Fourier Transform Infrared Spectrometry*, second edition, Wiley-Interscience, 2007.
- Guenther A. B., Zimmerman P. R., Harley P. C., Monson R. K, and Fall R., Isoprene and monoterpene emission rate variability: Model evaluations and sensitivity analyses. *J. Geophys. Res.*, 98(D7), doi:10.1029/93JD00527, 1993.
- Guenther A. B., Zimmerman P., and Wildermuth M., Natural volatile organic compound emission rate estimates for US woodland landscapes, *Atmos. Environ.*, 28, 1197-1210, 1994.
- Hase, F., Blumenstock, T., and Paton-Walsh, C.: Analysis of instrumental line shape of high-resolution FTIR-spectrometers using gas cell measurements and a new retrieval software, *Appl. Opt.*, 38(15), 3417 – 3422, 1999.
- Hermans, C., Vandaele, A. C., Carleer, M., Fally, S., Colin, R., Jenouvrier, A., and Mérienne, M. F., Absorption cross-sections of atmospheric constituents: NO₂, O₂, and H₂O. *Environ. Sci. & Pollut. Res.*, 6(3), 151. doi:10.1007/BF02987620, 1999
- Hong S. Y., Dudhia J, and Chen S. H., A revised approach to ice microphysical processes for the bulk parameterization of clouds and precipitation, *Monthly Weather Review*, 132: 103-120. doi:10.1175/1520-0493, 2004.
- Hong S. Y., Noh Y., and Dudhia J., A new vertical diffusion package with an explicit treatment of entrainment processes, *Monthly Weather Review*, 134, 2318-2341. doi:10.1175/MWR3199.1, 2006.
- Hönninger, G., von Friedeburg, C., and Platt, U., Multi axis differential optical absorption spectroscopy (MAX-DOAS). *Atmos. Chem. Phys.*, 4(1), 231–254. doi:10.5194/acp-4-231-2004, 2004
- Hoornweg, D., Freire, M., Lee, M. J., Bhada-Tata, P., Yuen, B.: *Cities and Climate Change: An Urgent Agenda*, The World Bank, Washington, D. C., 2010.
- Irion, F.W., Gunson, M.R., Toon, G.C., Chang, A.Y., Eldering, A., Mahieu, E., Manney, G.L., Michelsen, H.A., Moyer, E.J., Newchurch, M.J., Osterman, G.B., Rinsland, C.P., Salawitch, R.J., Sen B., Yung, Y.L., and Zander, R.: Atmospheric Trace Molecule Spectroscopy (ATMOS) Experiment Version 3 data retrievals, *Appl. Opt.*, 41(33), 6968 – 6979, 2002.

- Jenouvrier, A., Daumont, L., Regalia-Jarlot, L., Tyuterev, V. G., Carleer, M., Vandaele, A. C., Mikhailenko, S., Fally, S.: Fourier transform measurements of water vapor line parameters in the 4200-6600 cm^{-1} region, *J. Quant. Spect. Rad. Trans.*, 105(2), 326-355, doi:10.1016/j.jqsrt.2006.11.007, 2007.
- Keppel-Aleks, G., Toon, G. C., Wennberg, P. O., and Deutscher, N. M.: Reducing the impact of source brightness fluctuations on spectra obtained by Fourier-transform spectrometry, *Appl. Opt.*, 46(21), 4774-4779, doi:10.1364/AO.46.004774, 2007.
- Key, R., Sander, S., Eldering, A., Rider, D., Blavier, J.-F., Bekker, D., Wu, Y.-H., Manatt, K.: The Geostationary Fourier Transform Spectrometer, *Aerospace Conference Proceedings, 2012 IEEE*, doi:10.1109/AERO.2012.6187164, Big Sky, Montana, March 3rd to 10th 2012.
- Kim, S.W., McKeen, S.A., Frost, G.J., Lee, S.H., Trainer, M., Richter, A., Angevine, W.M., Atlas, E., et al., Evaluations of NO_x and highly reactive VOC emission inventories in Texas and their implications for ozone plume simulations during the Texas Air Quality Study 2006, *Atmos. Chem. Phys.*, 11, 11361-11386. doi:10.5194/acp-11-11361-2011, 2011.
- Kleinman, L. I., Daum, P. H., Lee, Y. N., Nunnermacker, L. J., Springston, S. R., Weinstein-Lloyd, J., and Rudolph, J., Sensitivity of ozone production rate to ozone precursors. *Geophys. Res Lett.*, 28(15), 2903-2906, 2001.
- Kleinman, L. I., The dependence of tropospheric ozone production rate on ozone precursors. *Atmos. Environ.*, 39(3), 575-586, doi:10.1016/j.atmosenv.2004.08.047, 2005
- Kleinman, L., Daum, P., and Lee, J., Dependence of ozone production on NO and hydrocarbons in the troposphere. *Geophys. Res Lett.*, 24(18), 2299-2302, 1997
- Kort, E.A., Frankenberg, C., Miller, C.E., and Oda, T.: Space-based observations of megacity carbon dioxide, *Geophys. Res. Lett.*, 39, L17806, doi:10.1029/2012GL052738, 2012.
- Langford, A.O., Brioude, J., Cooper, O.R., Senff, C.J., Alvarez, R.J., Hardesty, R.M., Johnson, B.J., and Oltmans, S.J., Stratospheric influence on surface ozone in the Los Angeles area during late spring and early summer of 2010, *J. Geophys. Res.*, 117, D00v06. doi:10.1029/2011jd016766, 2012.
- Levenberg, K., A method for the solution of certain non-linear problems in least squares, *Quart. Appl. Math.*, 2, 164-168, 1944.
- Livingston, W., Wallace, L.: An atlas of the solar spectrum in the infrared from 1,850 to 9,000 cm^{-1} (1.1 to 5.4 μm); *NSO Technical Report; NSO: Tucson, AZ, USA*, 1991.
- Lo J. C.-F., Yang Z.-L., and Pielke R. A., Assessment of three dynamical climate downscaling methods using the Weather Research and Forecasting (WRF) model, *J. Geophys. Res.*, 113: D09112. doi:10.1029/2007JD009216, 2008.
- Manning, C. J. and Combs, R. J.: FT-IR Interferogram sampling validation and correction, *Proc. SPIE, Electro-Optic, Integrated Optic, and Electronic Technologies for Online Chemical Process Monitoring with Advanced Techniques*, 3537, 181-186, 1999.
- Marquardt, D. W., An algorithm for least-squares estimation of nonlinear parameters, *J. Soc. Indust. Appl. Math.*, 11, 431- 441. 1963.

- Marr, L. C., and Harley, R. A., Spectral analysis of weekday – weekend differences in ambient ozone, nitrogen oxide, and non-methane hydrocarbon time series in California. *Atmos. Environ.*, 36, 2327–2335, 2002.
- Martin, R. V., Fiore, A.M., and van Donkelaar, A., Space-based diagnosis of surface ozone sensitivity to anthropogenic emissions. *Geophys. Res. Lett.*, 31(6), 2–5. doi:10.1029/2004GL019416, 2004.
- McKain, K., Wofsy, S. C., Nehr Korn, T., Eluszkiewicz, J., Ehleringer, J. R., and Stephens, B. B.: Assessment of ground-based atmospheric observations for verification of greenhouse gas emissions from an urban region, *PNAS*, doi:10.1073/pnas.1116645109, 2012.
- McKeen S. A., Wotawa G., Parrish D. D., Holloway J. S., Buhr M. P., Hubler G., Fehsenfeld F. C., and Meagher J. F., Ozone production from Canadian wildfires during June and July of 1995, *J. Geophys. Res.*, 107:D14, 4192. doi:10.1029/2001JD000697, 2002.
- Mesinger F., et al., North American Regional Reanalysis, *Bull Am. Met. Soc.*, 87, 343-360, doi: 10.1175/BAMS-87-3-343, 2006.
- Mlawer E. J., Taubman S. J., Brown P. D., Lacono M. J., and Clough S. A., Radiative transfer for inhomogeneous atmosphere: RRTM, a validated correlated-k model for the long-wave, *J. Geophys. Res.*, 102:D14, 16,663-16,682. doi:10.1029/97JD00237, 1997.
- Murphy, J. G., Day, D. A., Cleary, P. A., Wooldridge, P. J., Millet, D. B., Goldstein, A. H., et al., The weekend effect within and downwind of Sacramento - Part 1: Observations of ozone, nitrogen oxides, and VOC reactivity. *Atmos. Chem. and Phys.*, 7(20), 5327–5339, 2007.
- National Research Council, Committee on Earth Science and Applications from Space: A community assessment and strategy for the future: *Earth science and applications from space: national imperatives for the next decade and beyond*, National Academies Press, Washington D.C., 2007.
- Newman, S. M., Lane, I. C., Orr-Ewing, A. J., Newnham, D. A., and Ballard, J.: Integrated absorption intensity and Einstein coefficients for the $O_2 \text{ a}^1\Delta_g - X^3\Sigma_g^-(0,0)$ transition: A comparison of cavity ring down and high resolution Fourier transform spectroscopy with a long-path absorption cell, *J. Chem. Phys.* 110, 10749-10757, doi:10.1063/1.479018, 1999.
- Norton, R. H. and Rinsland, C. P.: ATMOS data processing and science analysis methods, *Applied Optics*, 30(4), 389-400, 1991.
- O'Dell, C. W., Connor, B., Bösch, H., O'Brien, D., Frankenberg, C., Castano, R., Christi, M., Eldering, D., Fisher, B., Gunson, M., McDuffie, J., Miller, C.E., Natraj, V., Oyafuso, F., Polonsky, I., Smyth, M., Taylor, T., Toon, G. C., Wennberg, P. O., and Wunch, D.: The ACOS CO₂ retrieval algorithm – Part 1: Description and validation against synthetic observations, *Atmos. Meas. Tech.*, 5, 99-121, doi:10.5194/amt-5-99-2012, 2012.
- Olsen, S. C., Randerson, J. T.: Differences between surface and column atmospheric CO₂ and implications for carbon cycle research, *J. Geophys. Res.*, 109, D02301, doi:10.1029/2003JD003968, 2004.
- Park, C., Q. Li, D. Chen, D. Fu, S. Sander, A. Jamroensan, G. Carmichael, R. Ahmadov, R. Kretschmer, C. Gerbig, Regional CO₂ Simulation over the L.A. Basin with WRF-VPRM, *CalNex 2010 Data Analysis Workshop Agenda, Sacramento, CA*, 2011.

- Pikelnaya, O., Hurlock, S. C., Trick, S., and Stutz, J. 2007. Intercomparison of multi-axis and long-path differential optical absorption spectroscopy measurements in the marine boundary layer. *J. Geophys. Res.*, 112(D10), 1–13. doi:10.1029/2006JD007727, 2007.
- Pingree, P. J., Blavier, J.-F. L., Toon, G. C., and Bekker, D. L.: An FPGA/SoC approach to on-board data processing enabling new Mars science with smart payloads, *Aerospace Conference Proceedings, 2007 IEEE, vol. 1*, pp. 1-12, doi:10.1109/AERO.2007.353091, Big Sky, Montana, March 3rd to 10th, 2007.
- Platt, U., and Stutz, J., *Differential Optical Absorption Spectroscopy*, Berlin, Heidelberg: Springer Berlin Heidelberg, p. 597, 2008.
- Pollack, I.B., Ryerson, T.B., Trainer, M., Parrish, D.D., Andrews, A.E., Atlas, E.L., Blake, D.R., Brown, S.S., et al., Airborne and ground-based observations of a weekend effect in ozone, precursors, and oxidation products in the California South Coast Air Basin, *J. Geophys. Res.*, 117. doi:10.1029/2011jd016772, 2012.
- Pougatchev, N. S., Campbell, J. F., Regan, C. R., Abrams, M. C., Brault, J. W., Farmer, C. B., and Hinton, D. E.: Advanced technologies high resolution Fourier transform spectrometer for atmospheric studies, *Aerospace Conference Proceedings, 2000 IEEE, vol. 3*, pp. 237–243, doi:10.1109/AERO.2000.879851, Big Sky, Montana, March 18th to 25th, 2000.
- Qin, Y., Tonnesen, G.S., and Wang, Z., Weekend/weekday differences of ozone, NO_x, CO, VOCs, PM₁₀ and the light scatter during ozone season in southern California, *Atmos. Environ.*, 38, 3069-3087. doi:10.1016/j.atmosenv.2004.01.035, 2004.
- Rodgers, C. D., *Inverse Methods for Atmospheric Sounding, Theory and Practice*. World Scientific Publishing, Singapore, 240 pp., 2000.
- Rothman, L.S., Gordon I.E., Barbe, A., Benner, C.D., Bernath, P.F., Birk, M., Boudon, V., Brown, L.R., Campargue, A., Champion, J.-P., Chance, K., Coudert, L.H., Dana, V., Devi, V.M., Fally, S., Flaud, J.-M., Gamache, R.R., Goldman, A., Jacquemart, D., Kleiner, I., Lacome, N., Lafferty, W.J., Mandin, J.-Y., Massie, S.T., Mikhailenko, S.N., Miller, C.E., Moazzen-Ahmadi, N., Naumenko, O.V., Nikitin, A.V., Orphal, J., Perevalov, V.I., Perrin, A., Predoi-Cross, A., Rinsland, C.P., Rotger, M., Iimeková, M., Smith, M.A.H., Sung, K., Tashkun, S.A., Tennyson, J., Toth, R.A., Vandaele, A.C., Vander Auwera, J.: The HITRAN 2008 molecular spectroscopic database, *J. Quant. Spect. Rad. Trans.*, 110, 533–572, 2009.
- Russell, A.R., Valin, L.C., Bucsela, E.J., Wenig, M.O., and Cohen, R.C., Space-based Constraints on Spatial and Temporal Patterns of NO_x Emissions in California, 2005-2008, *Environ. Sci. Technol.*, 44, 3608-3615. doi:10.1021/Es903451j, 2010.
- Sen, B., Osterman, G.B., Salawitch, R.J., Toon, G.C., Margitan, J.J., Blavier, J.-F., Chang, A.Y., May, R.D., Webster, C.R., Stimpfle, R.M., Bonne, G.P., Voss, P.B., Perkins, K.K., Anderson, J.G., Cohen, R.C., Elkins, J.W., Dutton, G.S., Hurst, D.F., Romashkin, P.A., Atlas, E.L., Schauffler, S.M., Loewenstein, M.: The budget and partitioning of stratospheric chlorine during the 1997 Arctic summer, *J. Geophys. Res.*, 104(D21), 26653 – 26665, 1999.
- Skamarock W. C., Positive-definite and monotonic limiters for unrestricted-time-step transport schemes, *Monthly Weather Review*, 134, 2241-2250. doi:10.1175/MWR3170.1, 2006.

- Smith, K. M., Newnham, D. A.: Near-infrared absorption cross sections and integrated absorption intensities of molecular oxygen (O₂, O₂-O₂, and O₂-N₂) *J Geophys. Res.*, 105(D6), 7383-7396, 2000.
- Smits B., "Efficiency Issues for Ray Tracing," *Journal of Graphics Tools*, Vol. 3, No. 2, pp. 1-14, 1998.
- Spurr, R., Kurosu, T., and Chance, K., A linearized discrete ordinate radiative transfer model for atmospheric remote-sensing retrieval. *J. Quant. Spect. Rad. Trans.*, 68(6), 689, 2001.
- Spurr, R., VLIDORT: A linearized pseudo-spherical vector discrete ordinate radiative transfer code for forward model and retrieval studies in multilayer multiple scattering media. *J. Quant. Spect. Rad. Trans.*, 102(2), 316–342, doi:10.1016/j.jqsrt.2006.05.005, 2006.
- Stutz, J., and Platt, U., Numerical analysis and estimation of the statistical error of differential optical absorption spectroscopy measurements with least-squares methods. *Appl. Opt.*, 35(30), 1996.
- Sullivan D. C., Reid S. B., Stiefer P.S., Funk T. H., and Chinkin L. R., On-road mobile source emission inventory development for the central states regional air planning association. *14th International Emission Inventory Conference: "Transforming Emission Inventories - Meeting Future Challenges Today"*, Las Vegas, April. 2005.
- Toth, R. A., Brown, L. R., Miller, C. E., Malathy Devi, V., Benner, D. C.: Spectroscopic database of CO₂ line parameters: 4300-7000 cm⁻¹, *J. Quant. Spect. Rad. Trans.*, 109(6), Spectroscopy and Radiative Transfer in Planetary Atmospheres, 906-921, doi:10.1016/j.jqsrt.2007.12.004, 2008.
- Toth, R.A.: Line positions and strengths of N₂O between 3515 and 7800cm⁻¹, *J. Mol. Spectrosc.*, 197, 158–87, 1999.
- Toth, R.A.: Measurements of positions, strengths and self-broadened widths of H₂O from 2900 to 8000 cm⁻¹: line strength analysis of the 2nd triad bands, *J. Quant. Spect. Rad. Trans.*, 94(1), 51-107, 2005.
- Toth, R.A.: N₂ and air-broadened linewidths and frequency-shifts of N₂O, *J. Quant. Spect. Rad. Trans.*, 66, 285–304, 2000.
- Vandaele, A., Hermans, C., Fally, S., Carleer, M., Colin, R., Merrienne, M.F., Jenouvrier, A., and Coquart B., High-resolution Fourier transform measurement of the NO₂ visible and near-infrared absorption cross sections: temperature and pressure effects. *J. Geophys. Res.*, 107(D18), 4348. doi:10.1029/2001JD000971, 2002.
- Veres, P., Roberts, J.M., Warneke, C., Welsh-Bon, D., Zahniser, M., Herndon, S., Fall, R., and de Gouw, J., Development of negative-ion proton-transfer chemical-ionization mass spectrometry (NI-PT-CIMS) for the measurement of gas-phase organic acids in the atmosphere, *Int. J. Mass. Spectrom.*, 274, 48-55. doi: 10.1016/j.ijms.2008.04.032, 2008.
- Voigt, S., Orphal, J., Bogumil, K., and Burrows, J. P., The temperature dependence (203–293 K) of the absorption cross sections of O₃ in the 230–850 nm region measured by Fourier-transform spectroscopy. *J. Photochem. Photobio. A: Chem.*, 143(1), 1–9. doi:10.1016/S1010-6030(01)00480-4, 2001.

- Vountas, M., Rozanov, V. V., and Burrows, J. P., Ring effect: Impact of rotational Raman scattering on radiative transfer in Earth's atmosphere, *J. Quant. Spectrosc. Radiat. Transfer*, 60, 943–961, 1998.
- Wagner, T., Dix, B., Friedeburg, C., Frieß, U., Sanghavi, S., Sinreich, R., and Platt, U., MAX-DOAS O₄ measurements: A new technique to derive information on atmospheric aerosols—Principles and information content. *J. Geophys. Res.*, 109(D22), D22205. doi:10.1029/2004JD004904, 2004
- Wallace, L., Hinkle, K., Livingston, W.C.: An Atlas of the Photospheric Spectrum from 8,900 to 13,600 cm⁻¹ (7350 to 11230 Å); *NSO Technical Report; NSO: Tucson, AZ, USA*, 1993.
- Washenfelder, R. A., Toon, G. C., Blavier, J. F., Yang, Z., Allen, N. T., Wennberg, P. O., Vay, S. A., Matross, D. M., and Daube, B. C.: Carbon dioxide column abundances at the Wisconsin Tall Tower site, *J. Geophys. Res.*, 111, D22305, doi:10.1029/2006JD007154, 2006.
- Wicker L. J., and Skamarock W. C., Time splitting methods for elastic models using forward time schemes, *Monthly Weather Review*, 130, 2088 -2097. doi:10.1175/1520-0493, 2002.
- Wild O., Zhu X., and Prather M. J., FAST-J: accurate simulation of in- and below-cloud photolysis in tropospheric chemical models, *J. Atmos. Chem.*, 37, 245-282. doi: 10.1023/A:1006415919030, 2000.
- Wong, K.W., D. Fu, T. Pongetti, S. Newman, Y. Hsu, E. Kort, C. Miller, R. Duren, Y.L. Yung, and S. Sander, Mapping CH₄:CO₂ ratio in Los Angeles with CLARS-FTS from Mount Wilson, *Atmos. Chem. Phys. Discuss.*, 14, 17037-17066, doi:10.5194/acpd-14-17037-2014, 2014.
- Wunch, D., Toon, G. C., Blavier, J. -F. L., Washenfelder, R. A., Notholt, J., Connor, B. J., Griffith, D. W. T., Sherlock, V., and Wennberg, P. O.: The total carbon column observing network, *Philosophical Transactions of the Royal Society - Series A: Mathematical, Physical and Engineering Sciences*, 369(1943), 2087-2112, doi:10.1098/rsta.2010.0240, 2011.
- Wunch, D., Toon, G. C., Wennberg, P. O., Wofsy, S. C., Stephens, B., Fisher, M. L., Uchino, O., Abshire, J. B., Bernath, P. F., Biraud, S. C., Blavier, J. -F. L., Boone, C. D., Bowman, K. P., Browell, E. V., Campos, T., Connor, B. J., Daube, B. C., Deutscher, N. M., Diao, M., Elkins, J. W., Gerbig, C., Gottlieb, E., Griffith, D. W. T., Hurst, D. F., Jiménez, R., Keppel-Aleks, G., Kort, E. A., Macatangay, R., Machida, T., Matsueda, H., Moore, F. L., Morino, I., Park, S., Robinson, J., Roehl, C. M., Sawa, Y., Sherlock, V., Sweeney, C., Tanaka, T., and Zondlo, M. A.: Calibration of the Total Carbon Column Observing Network using aircraft profile data, *Atmos. Meas. Techn.*, 3(5), 1351-1362, 2010.
- Wunch, D., Wennberg, P. O., Toon, G. C., Keppel-Aleks, G., and Yavin, Y. G.: Emissions of greenhouse gases from a North American megacity, *Geophys. Res. Lett.*, 36, L15810, doi:10.1029/2009GL039825, 2009.
- Yang, Z., Wennberg, P. O., Cageao, R. P., Pongetti, T. J., Toon, G. C., Sander, S. P.: Ground-based photon path measurements from solar absorption spectra of the O₂ A-band, *J. Quant. Spect. Rad. Trans.*, 90(3-4), 309-321, doi:10.1016/j.jqsrt.2004.03.020, 2005.

Zaveri R. A, and Peters L. K, A new lumped structure photochemical mechanism for large-scale applications, *J. Geophys. Res.*, 104:D23, 30,387-30,415. doi: 10.1029/1999JD900876, 1999.

Zaveri R. A., Easter R. C., Fast J. D., and Peters L. K., Model for Simulating Aerosol Interactions and Chemistry (MOSAIC), *J. Geophys. Res.*, 113:D13, D13204. doi:10.1029/2007JD008782, 2008.

8. Glossary

AB32	Assembly Bill (AB) 32
AERONET	Aerosol Robotic Network
Ak	Averaging Kernel
AOT	Aerosol optical thickness
ARB	Air Resources Board
ART	Arcadia Race Track
ATMOS	Atmospheric Trace Molecule Spectroscopy Mission
BASE_NO _x	Baseline WRF-CHEM model case
BL	Boundary layer
BLH	Boundary Layer Height
CalNex	California Nexus 2010 field experiment
Caltech	California Institute of technology
CARB	California Air Resources Board
CLARS	California Laboratory for Atmospheric Remote Sensing
CLARS-IPP	CLARS interferogram processing program
DOAS	Differential Optical Absorption Spectroscopy
DoF	Degrees of freedom
DSCD	Differential slant column densities
DSV	Direct Spectralon® viewing
EPA	Environmental Protection Agency
EVI	Enhanced vegetation index
FFT	Fast Fourier Transform
FTIR	Fourier Transform infrared
FTS	Fourier Transform Spectrometer
GFIT	FTS retrieval algorithm
GHG	Greenhouse gas
GOSAT	Greenhouse Gases Observing Satellite
HITRAN	High-resolution transmission molecular absorption database
IR	Infrared
JPL	Jet Propulsion Laboratory
LA	Los Angeles

LABS	Los Angeles Basin Surveys
LOW_NO _x	Low NO _x WRF-CHEM model case
LSWI	Land surface water
MAX-DOAS	Multi-axis Differential Optical Absorption Spectroscopy
MOD	Model
MOPD	Maximum Optical Path Difference
<i>NARR</i>	North American Regional Reanalysis
NASA	National Aeronautics and Space Administration
NBL	Nocturnal Boundary layer
NCEP	National Center for Environmental Prediction
NCEP	National Centers for Environmental Prediction
Near-IR	Near-infrared
NEI	National Emission Inventory
NOAA	National Oceanic and Atmospheric Administration
OBS	Observation
OCO-2	Orbiting Carbon Observatory-2
PAR	Photosynthetically active radiation
PBL	Planetary boundary layer
PBLH	Planetary boundary layer height
ppb/ppbv	parts per billion (volume)
ppm/ppmv	parts per million (volume)
RMS	Root mean square
RMSE	Root mean square error
RT	Radiative transfer
RTM	Radiative transfer model
S.D.	Standard deviation
SCAB	South-coast Air Basin
SCD	Slant column densities
SNR	Signal-to-Noise ratio
SV	Spectralon® viewing
SVO	Spectralon® Viewing Observations
SZA	Solar zenith angle

TCCON	Total Carbon Column Observing Network
UCLA	University of California Los Angeles
UTC	Coordinated Universal Time
UV	Ultraviolet
UV-vis	Ultraviolet - visible
VLIDORT	Vector Linearized Discrete Ordinate Radiative Transfer
VMR	Volume mixing ratio
VOC	Volatile organic carbon
WD	Weekday
WE	Weekend
WP	West Pasadena
WPS	WRF Preprocessing System
WRF	Weather Research and Forecasting (model)
WRF-CHEM	Weather Research and Forecasting model coupled with online chemistry
WRF-STILT	Weather Research and Forecasting – Stochastic Time-Inverted Lagrangian Transport (model)
WRF-VPRM	Weather Research and Forecasting model coupled to Vegetation Photosynthesis and Respiration Model.
XCH ₄	Column-averaged dry-air mole fractions of methane
XCO	Column-averaged dry-air mole fractions of carbon monoxide
XCO ₂	Column-averaged dry-air mole fractions of carbon dioxide
XGHG	Column-averaged dry-air mole fractions of greenhouse gases